REPORT DOCUMENTATION PAGE

1

Form Approved OMB NO. 0704-0188

The public reporting burden for this collection of information is estimated to average 1 hour per response, including the time for reviewing instructions, searching existing data sources, gathering and maintaining the data needed, and completing and reviewing the collection of information. Send comments regarding this burden estimate or any other aspect of this collection of information, including suggesstions for reducing this burden, to Washington Headquarters Services, Directorate for Information Operations and Reports, 1215 Jefferson Davis Highway, Suite 1204, Arlington VA, 22202-4302. Respondents should be aware that notwithstanding any other provision of law, no person shall be subject to any oenalty for failing to comply with a collection of information if it does not display a currently valid OMB control number.
PLEASE DO NOT RETURN YOUR FORM TO THE ABOVE ADDRESS.

1. REPORT DATE (DD-MM-YYYY) 31-08-2014	2. REPORT TYPE Ph.D. Dissertation	3. DATES COVERED (From - To) -

4. TITLE AND SUBTITLE
Controlling Atomic, Solid-State and Hybrid Systems for Quantum Information Processing

5a. CONTRACT NUMBER
W911NF-11-1-0400

5b. GRANT NUMBER

5c. PROGRAM ELEMENT NUMBER
611103

6. AUTHORS
Michael Gullans

5d. PROJECT NUMBER

5e. TASK NUMBER

5f. WORK UNIT NUMBER

7. PERFORMING ORGANIZATION NAMES AND ADDRESSES
Massachusetts Institute of Technology (MIT
77 Massachusetts Ave.
NE18-901
Cambridge, MA 02139 -4307

8. PERFORMING ORGANIZATION REPORT NUMBER

9. SPONSORING/MONITORING AGENCY NAME(S) AND ADDRESS (ES)
U.S. Army Research Office
P.O. Box 12211
Research Triangle Park, NC 27709-2211

10. SPONSOR/MONITOR'S ACRONYM(S)
ARO

11. SPONSOR/MONITOR'S REPORT NUMBER(S)
59745-PH-MUR.80

12. DISTRIBUTION AVAILIBILITY STATEMENT
Approved for public release; distribution is unlimited.

13. SUPPLEMENTARY NOTES
The views, opinions and/or findings contained in this report are those of the author(s) and should not contrued as an official Department of the Army position, policy or decision, unless so designated by other documentation.

14. ABSTRACT

Quantum information science involves the use of precise control over quantum systems to explore new technologies. However, as quantum systems are scaled up they require an ever deeper understanding of many-body physics to achieve the required degree of control. Current experiments are entering a regime which requires active control of a mesoscopic number of coupled quantum systems or quantum bits (qubits). This thesis describes several approaches to this goal and shows how mesoscopic quantum systems can be controlled and utilized for quantum information tasks

15. SUBJECT TERMS
QuISM

16. SECURITY CLASSIFICATION OF:			17. LIMITATION OF ABSTRACT	15. NUMBER OF PAGES	19a. NAME OF RESPONSIBLE PERSON Paola Cappellaro
a. REPORT	b. ABSTRACT	c. THIS PAGE			
UU	UU	UU	UU		19b. TELEPHONE NUMBER 617-253-8137

Standard Form 298 (Rev 8/98)
Prescribed by ANSI Std. Z39.18

Report Title

Controlling Atomic, Solid-State and Hybrid Systems for Quantum Information Processing

ABSTRACT

Quantum information science involves the use of precise control over quantum systems to explore new technologies. However, as quantum systems are scaled up they require an ever deeper understanding of many-body physics to achieve the required degree of control. Current experiments are entering a regime which requires active control of a mesoscopic number of coupled quantum systems or quantum bits (qubits). This thesis describes several approaches to this goal and shows how mesoscopic quantum systems can be controlled and utilized for quantum information tasks.

HARVARD UNIVERSITY
Graduate School of Arts and Sciences

DISSERTATION ACCEPTANCE CERTIFICATE

The undersigned, appointed by the

Department of Physics

have examined a dissertation entitled

Controlling Atomic, Solid-State and Hybrid Systems for Quantum Information Processing

presented by Michael John Gullans

candidate for the degree of Doctor of Philosophy and hereby certify that it is worthy of acceptance.

Signature ______________________________

Typed name: Professor Mikhail Lukin, Chair

Signature ______________________________

Typed name: Professor Bertrand Halperin

Signature ______________________________

Typed name: Professor Vladan Vuletić

Date: September 4, 2013

Controlling Atomic, Solid-State and Hybrid Systems for Quantum Information Processing

A dissertation presented
by

Michael John Gullans

to
The Department of Physics
in partial fulfillment of the requirements
for the degree of
Doctor of Philosophy
in the subject of

Physics

Harvard University
Cambridge, Massachusetts
September 2013

©2013 - Michael John Gullans

All rights reserved.

Professor Mikhail D. Lukin **Michael John Gullans**

Controlling Atomic, Solid-State and Hybrid Systems for Quantum Information Processing

Abstract

Quantum information science involves the use of precise control over quantum systems to explore new technologies. However, as quantum systems are scaled up they require an ever deeper understanding of many-body physics to achieve the required degree of control. Current experiments are entering a regime which requires active control of a mesoscopic number of coupled quantum systems or quantum bits (qubits). This thesis describes several approaches to this goal and shows how mesoscopic quantum systems can be controlled and utilized for quantum information tasks.

The first system we consider is the nuclear spin environment of GaAs double quantum dots containing two electrons. We show that the through appropriate control of dynamic nuclear polarization one can prepare the nuclear spin environment in three distinct collective quantum states which are useful for quantum information processing with electron spin qubits. We then investigate a hybrid system in which an optical lattice is formed in the near field scattering off an array of metallic nanoparticles by utilizing the plasmonic resonance of the nanoparticles. We show that such a system would realize new regimes of dense, ultra-cold quantum matter and can be used to create a quantum network of atoms and plasmons. Finally we investigate quantum nonlinear optical systems. We show that the intrinsic nonlinearity for plasmons in graphene can be large enough to make a quantum gate for single photons. We also consider two nonlinear optical systems based on ultracold gases of atoms. In one case, we theoretically analyze an all-optical single photon switch using cavity quantum electrodynamics (QED) and slow light. In the second case, we study few photon physics in strongly interacting Rydberg polariton systems, where we demonstrate the existence of two and three photon bound states and study their properties.

Contents

Title Page i
Abstract iii
Table of Contents v
List of Figures viii
List of Tables x
Citations to Previously Published Work xi
Acknowledgments xii
Dedication xiv

1 Introduction **1**
1.1 Motivation 1
1.2 Mesoscopic Quantum Systems 2
1.2.1 Electron and Nuclear Spins in Solids 2
1.2.2 Optical Lattices for Ultracold Atoms 5
1.2.3 Quantum Nonlinear Optical Systems 6
1.3 Structure of Thesis 7

2 Dynamic Nuclear Polarization in Double Quantum Dots **9**
2.1 Introduction 9
2.2 Setup 14
2.3 Model 16
2.4 Results 23
2.4.1 Noise Free Nuclear Spins 27
Polarization Saturation 29
Growth of Difference Fields 30
Zero States 31
Crossover 31
Stability of Zero States 33
2.4.2 Effect of Nuclear Spin Noise 34
Unequal Dots 34
Identical Dots 39

2.5 Relevance to Other Central Spin Systems 42
2.6 Conclusions 43

3 Nanoplasmonic Lattices for Ultracold Atoms 45
3.1 Introduction 45
3.2 Atom Trapping Above a Single Metallic Nanoparticle 48
3.3 Atom Trapping Above a Lattice of Nanoparticles 50
3.4 Hubbard Models in Nanoscale Lattices 51
3.5 Plasmon Mediated Interactions and Entanglement in the Nanolattice 53
3.6 Conclusions 58

4 Single Photon Nonlinear Optics with Graphene Plasmons 59
4.1 Introduction 59
4.2 Graphene Plasmonics 61
4.3 Nonlinear Plasmonics in Graphene 63
4.4 Graphene Macro-Atom 64
4.5 Efficient Coupling and a Single-photon Switch 67
4.6 Conclusions 72

5 All-Optical Switch and Transistor Gated by One Photon 73
5.1 Introduction 73
5.2 Theoretical Model 78
5.3 Experimental Results 83
5.4 Conclusions 85

6 Few Body Physics in Strongly Interacting Rydberg-Polariton Gases 87
6.1 Introduction 87
6.2 Numerical Approach for Atom-Photon Interactions 90
6.3 Results 91
  6.3.1 Two Photon Solitons 93
  6.3.2 Three Photon Solitons 94
6.4 Conclusions 95

A Appendices to Chapter 2 96
A.1 Parameters Used in Simulations 96
A.2 Φ Variables 96
A.3 Multiple Nuclear Species 104

B Appendics to Chapter 3 108
B.1 Van der Waals Interaction with the Nanosphere 108
B.2 Heating Rate from Inelastic Light Scattering 111
B.3 Tuning the Lattice Potential 112
B.4 Effective Scattering Length in Tight Traps 113

B.5 Two Atom Entanglement on the Lattice 115

C Appendices to Chapter 4 **118**

C.1 Nonlinear Conductivity 118

C.2 Quantizing the Plasmon Mode 120

C.3 Coupling between Nanoribbon and Cavity 120

D Appendices to Chapter 6 **122**

D.1 Numerical Code for Two-Photon Time Dependent Dynamics 122

D.2 Numerical Code for Three-Photon Steady State Solution 124

Bibliography **133**

List of Figures

1.1 Electrically gated quantum dots. 4

2.1 Schematic of dynamic nuclear polarization in double quantum dots. . 14
2.2 Schematic of our numerical approximation and simulation parameters. 22
2.3 Phase diagram for identical dots in simplified model. 25
2.4 Phase diagram for identical dots without noise using experimental parameters. 26
2.5 Examples of trajectories for the different regions of the phase diagram. 28
2.6 Example trajectories where the zero state is achieved and destabilized by noise. 32
2.7 Asymptotic values of $|D_z/S_z|$ for asymmetric dots. 35
2.8 Phase diagram for identical dots with noise using experimental parameters. 42

3.1 Schematic of physics in nanoplasmonic lattice and trapping potentials. 47
3.2 Hubbard parameters in nanoscale lattice. 53
3.3 Long range entanglement of atoms mediated by plasmons. 54

4.1 Schematic of graphene macro-atom and scaling of nonlinearity. 65
4.2 $g^2(t)$ in emission for the graphene macro-atom. 67
4.3 Performance of the graphene based single photon switch. 68

5.1 All-optical switch and transistor. 77
5.2 Theoretical curve showing the two-photon cross-correlation function of the gate and signal field. 82
5.3 Measured cross correlation function compared to theory 84

6.1 Schematic of Rydberg-polariton system. 89
6.2 Two-photon soliton dynamics. 94
6.3 Three photon solutions in steady state. 95

A.1 Results for the different size and identical dots when multiple species are included. 105

B.1 Demonstration of the tuning of the tunneling in the nanoscale Hubbard model. 113
B.2 Diagram used to calculate the effective scattering length for different trap frequencies. 115
B.3 Preparation procedure for long-range, ground state, two-atom entanglement in nanoplasmonic lattice. 116

List of Tables

A.1 Parameters used in simulations of DNP in double quantum dots. . . . 97
A.2 Parameters for different nuclear species in GaAs. 104

Citations to Previously Published Work

Most of the chapters of this thesis have appeared in print elsewhere. By chapter number, they are

- Chapter 2: *Dynamic Nuclear Polarization in Double Quantum Dots*, M. Gullans, J. J. Krich, J. M. Taylor, H. Bluhm, B. I. Halperin, C. M. Marcus, M. Stopa, A. Yacoby, and M. D. Lukin, Phys. Rev. Lett. 104, 226807 (2010) and *Preparation of Non-Equilibrium Nuclear Spin States in Double Quantum Dots*, M. Gullans, J. J. Krich, J. M. Taylor, B. I. Halperin, and M. D. Lukin, Phys. Rev. B 88, 035309 (2013).

- Chapter 3: *Nanoplasmonic Lattices for Ultracold Atoms*, M. Gullans, T. D. Tiecke, D. E. Chang, J. Feist, J. D. Thompson, J. I. Cirac, P. Zoller, and M. D. Lukin, Phys. Rev. Lett. 109, 235309 (2012).

- Chapter 4: *Single-photon nonlinear optics with graphene plasmons*, M. Gullans, D. E. Chang, F. H. L. Koppens, F. J. García de Abajo and M. D. Lukin, submitted to Phys. Rev. Lett.(2013).

- Chapter 5: *All-Optical Switch and Transistor Gated by One Photon*, W. Chen, K. M. Beck, Q. Lin, R. Bücker, M. Gullans, M. D. Lukin, H. Tanji-Suzuki, and V. Vuletic, Science 341, 768 (2013) and W. Chen, K. M. Beck, Q. Lin, R. Bücker, M. Gullans, M. D. Lukin, H. Tanji-Suzuki, and V. Vuletic, in preparation (2013).

- Chapter 6: *Few Body Physics in Strongly Interacting Rydberg-Polariton Gases*, M. Gullans, I. Martin, O. Firstenberg, T. Pohl. Otterbach, and M. D. Lukin, in preparation (2013) and *Strongly Interacting Photons* W. Chen, K. Beck, M. Gullans, T. Peyronel, O. Firstenberg, Q. Liang, A. Gorshkov, M. D. Lukin and V. Vuletić ICOLS proceedings, to appear (2013)

Acknowledgments

The years of my PhD have been an incredible time of personal and professional growth for me, which is, in large part, due to the influence of the people I have interacted with during my time at Harvard. First I would like to thank my adviser Mikhail Lukin who has constantly supported me and challenged me in my work. His passion and vision for science and discovery is an inspiration. I would also like to thank the other members of my thesis committee Bertrand Halperin and Vladan Vuletic. Every time I discuss with them I learn a new piece of physics or insight. I look forward to continued collaboration with all three of my committee members.

In addition to my committee members I received helpful mentorship from Jake Taylor who guided me through my first research project in the group and has taught me a lot of physics and the "art of getting things done". I also benefited from much helpful advice and insightful discussions with Peter Zoller, while he was on sabbatical from Innsbrück. I would also like to thank my undergraduate adviser Jonathan Wurtele who has continued to guide and support me since coming to Harvard.

I would like to thank my collaborators over the years, especially Jacob Krich, who was my first collaborator. In addition to solid-state physics, Jacob taught me a lot about how to be clear and unbiased in approaching science and improved my communication and collaborative skills. I have also had many fruitful collaborations with Darrick Chang and I always appreciate the insights and unique perspective he brings to problems. I would also like to thank my collaborators Ivar Martin, Wenlan Chen, Kristin Beck, Hendrik Bluhm, Mark Rudner, Frank Koppens, Anders Sørensen, Johannes Feist, F. Javier Garcia de Abajo, Ignacio Cirac, and Amir Yacoby, all of whom have greatly influenced my approach to physics.

Of course I have to also thank the Lukin group members which form a passionate and vibrant community of scientists, as well as the occasional pick up basketball, softball, volleyball, hockey and tennis team. Both past and present members have influenced me starting with the generation before me including Mohammad Hafezi, Alexey Gorshkov, Sebastian Hofferberth, Liang Jiang, Jeronimo Maze, and Emre Togan, to the current generation including Norman Yao, Thibault Peyronnel, Jeff Thompson, Tobias Tiecke, Shimon Kolkowitz, Quirin Unterreithmeier, Eric Kessler, Mike Goldman, Alp Sipahigil, Ruffin Evans, Ofer Firstenberg, Johannes Otterbach, Steve Bennet, Alex Kubanek, Alex Sushkov, Peter Mauer, Nathalie Thompson, and Brendan Shields, as well as the up and coming members. I have so many fond memories formed with all of them over the years at work, conferences and our free time.

Along with the Lukin group I benefited from a close friendship with my physics classmates especially Yiwen, Jayson, Laura, Yiwen, Adi, Eddie, Jack, Nick, Sofia, Gio, Brian, and Julia. With many fun dinners, Rustica lunches, evenings, ski trips, and other outings they contributed greatly to my mental well being over the years and I hope we stay close as the years go by. Outside the department I benefited from what I hope are lifelong friendships with Serge, Sveta, Pavlo, David, Steffie, Jenny, Luke, and Deane.

I also want to acknowledge all the support and love I have received from my family. Including my immediate family in my parents, brother and sister and her husband, as well as my extended family of cousins, aunts and uncles. Finally, I want to thank my love, Christina, as we look forward to this next chapter in our lives.

Dedicated to my parents

Mark and Gayle Gullans

Chapter 1

Introduction

1.1 Motivation

Since its inception in the 80's and 90's quantum information science has developed into a mature field whose central goal is to develop new technologies based on the precise control of quantum systems. Realization of this goal requires contributions from many fields of science and engineering including physics, materials science, computer science, chemistry and, even, biology. Broadly speaking the applications for such quantum systems fall into two categories: information science, i.e. computation and communication, and measurement science, i.e. improved (broadly defined) sensors and precision. On the surface these two sets of applications seem unrelated, however, they are intricately linked in quantum science. As quantum information systems are pushed to their limits in terms of complexity they require increasing precision to characterize and operate. In addition, quantum systems developed for information science are so well isolated and controllable that developing them into precision sensors is a natural application. At the same time, quantum systems developed for their metrological applications have become good candidates for the building blocks of quantum computers.

This thesis will focus on the use of quantum systems for applications in information science. The challenges in this field include, first, scaling up the quantum systems and, then, achieving sufficient control to utilize them for information science. This is difficult on a technological level as it requires the development of new systems with improved control, but also on a fundamental level because the use of such systems requires a deep understanding of the many-body physics of interacting quantum systems. Gaining such understanding is, perhaps, the primary goal in theoretical efforts for quantum information science. A task which is often complicated by the fact that the systems under consideration are fundamentally out of equilibrium. The interplay between non-equilibrium many-body physics and quantum information science is a central theme in this thesis. In what follows we explore a range of physical systems currently being pursued for quantum information applications with the goal of harnessing their many-body behavior to achieve new applications as well as a deeper understanding of quantum physics.

1.2 Mesoscopic Quantum Systems

1.2.1 Electron and Nuclear Spins in Solids

A promising candidate for a qubit, the fundamental building block of a quantum computer, is the spin of an electron. The electron can be bound to an atom or ion in free space or confined in a solid state environment. In the former case the electron is well isolated with long coherence times; however, the fabrication and manipulation of such systems is cumbersome making it difficult to scale them up to many qubits. On the other hand, trapping electrons in solids holds promising potential for scaling up to a full size quantum computer, but has the tradeoff that the electrons interacts strongly with their host environment. Nevertheless there are several condensed matter systems where single electrons can be well enough isolated from their environment that they have coherence properties comparable to single atoms or ions.

Solid state spin qubits generally arise from the electron spin of an impurity atom or a quantum dot. Notable examples of impurity systems are Nitrogen Vacancy (NV) centers in diamond (Jelezko and Wrachtrup, 2006) and phosphorous donors in silicon (Zwanenburg et al., 2013). Such impurities, to a large degree, behaves as single trapped atoms. Quantum dots are artificially trapped electrons which are confined by a material interface, sometimes in combination with electric gates (Hanson et al., 2007). Many properties of quantum dot systems can also be explained by treating them as atoms, but the typical confinement energies (from meV to eV) and length scales (from several microns to a few nanometers) vary more dramatically than impurity based qubits. In this thesis we focus on electrically gated double quantum dots in type III-V semiconductors whose properties are illustrated in Fig. 1.1.

Many fundamental quantum operations have been demonstrated for such double quantum dot systems including, initialization, readout and single qubit operations (Petta et al., 2005) and two qubit entanglement (Shulman et al., 2012). However, a ubiquitous problem with these systems is that the electron spins interact with the

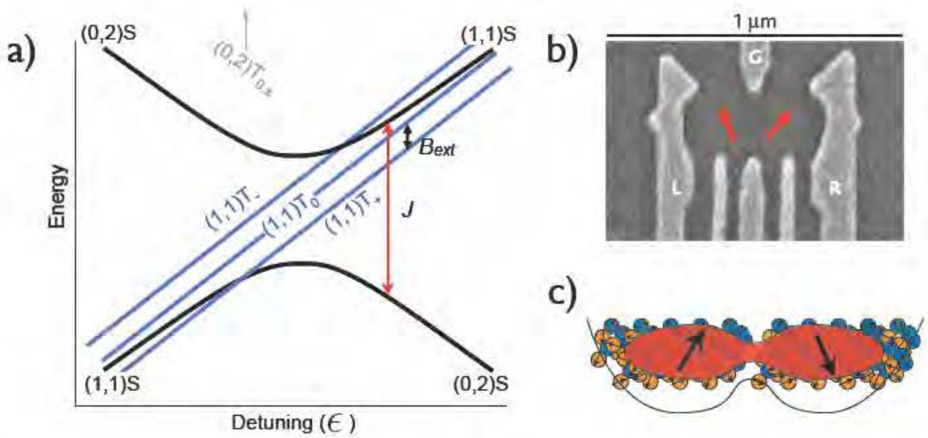
a)
(0,2)S
(0,2)T0,±
(1,1)S
Bext
J
(1,1)T-
(1,1)T0
(1,1)T+
(1,1)S
(0,2)S
Energy
Detuning (ϵ)
b)
1 μm
G
L
R
c)

Figure 1.1: a) Energy diagram of a GaAs double quantum dot, where (n, m) refers to the charge occupancy of the two dots and $S(T_m)$ refers to the two electron spin state in a singlet(triplet m) state. J is the exchange splitting between the two singlet states, B_{ext} is the magnetic field and ϵ is the voltage difference between the left and right dots. The qubit states are formed from the (1,1)S and (1,1)T_0 state. b) SEM image of a double quantum dot in GaAs (adapted from (Petta et al., 2005)). c) A double quantum dot with two electrons interacting with a large number of lattice nuclear spins.

nuclear spin of the GaAs host lattice through the hyperfine interaction. As the scale of these quantum dots is several hundred nanometers, the electrons interact with on the order of $10^5 - 10^6$ nuclei as illustrated in Fig. 1.1bc. A surprising feature of the nuclear spin environment is that, due to long nuclear spin coherence times, one can use the nuclear spins as a resource for quantum control of the double dot qubit (Foletti et al., 2009). In this thesis we explore theoretically how to achieve this control through dynamic nuclear polarization of the nuclear spins.

1.2.2 Optical Lattices for Ultracold Atoms

Building a general purpose quantum computer remains an outstanding challenge. A more immediate goal is to build a quantum simulator, which is a device that can solve the quantum dynamics of an interacting, many-body Hamiltonian. A powerful realization of a quantum simulator is an ensemble of cold atoms in an optical lattice, which is periodic potential for the atoms formed by interfering several laser beams. Such optical lattices allow one to realize analogous physics to strongly correlated electron systems, but in a controlled environment with much less noise.

The field of cold gases in optical lattices is by now a well developed with several seminal discoveries including the observation of the superfluid to Mott insulator transition in the Bose-Hubbard model, the crossover from a Bose-Einstein condensate (BEC) to a Bardeen-Cooper-Schriefer (BCS) superfluid and the quantum phase transition of an antiferromagnet in the Ising model (Bloch et al., 2012; Grimm et al., 2000; Simon et al., 2011). One of the main goals of quantum simulation in optical lattices is to realize the two dimensional Fermi-Hubbard model at very low temperatures to determine if there is a d-wave superfluid phase. This is an outstanding question in condensed matter physics with many implications for high-Tc superconductors and other strongly correlated systems. To explore these issues improvements to existing optical lattice systems must be made. In this thesis we explore a novel optical lattice system where the trapping field is formed from the scattered light off an array of plasmonic nanoparticles, which allows one to increase the energy scales of the system and achieve novel long-range interactions via the electromagnetic modes of the nanoparticles.

1.2.3 Quantum Nonlinear Optical Systems

Recent years have seen many breakthroughs in our ability manipulate and control light. On the one hand, advances in materials science and nanoscience have allowed the design of devices with structure well below the wavelength of light. Notable examples include photonic crystals in dielectric media (Joannopoulos et al., 2008), plasmonic structures in metallic systems (Barnes et al., 2008), metamaterial systems (Shalaev, 2007), and optomechanical systems (Marquardt and Girvin, 2009). On the other hand, the growing field of quantum information science has provided a new standard for controlling the quantum properties of light, as well as a host of novel platforms to achieve this control (O'Brien et al., 2009). A fundamental challenge for applications of these systems is achieving strong interactions between photons. The most stringent example is in quantum information, where one requires significant nonlinearities at the level of a single quanta. In addition, photonic and quantum optical systems offer a new paradigm in theoretical physics in that they are fundamentally non-equilibrium systems. Such systems provide an exciting opportunity to develop new technologies in both the classical and quantum domains, as well as probe fundamental questions regarding non-equilibrium many-body physics

In this thesis we analyze several systems where it is possible to realize nonlinear optical effects at the level of a few photons. First we show that the intrinsic nonlinearity for plasmons in graphene nanostructures is strong enough that the material can become nonlinear at the level of a single plasmon as illustrated in Figure 1 . Such effects occur due the subwavelength confinement of the plasmons compared to free space, which significantly enhances the electric field intensity per photon. We then go on to look at nonlinear effects in atomic ensembles where the long coherence times allow one to store the photons as matter for long times to achieve large interactions. We consider two approaches, one based on cavity quantum electrodynamics (QED) to achieve the interactions and the other based on excitation to strongly interacting Rydberg states.

1.3 Structure of Thesis

Chapter 2 of this thesis is focused on double dot electron spin qubits. We show how to control and prepare the nuclear spin environment of the electron spins through dynamic nuclear polarization. In Chapter 3 we propose and analyze a novel approach to the realization of high-density optical lattices using the optical potential formed from the near field scattering of light by an array of plasmonic nanoparticles. In chapters 4-6 we consider quantum nonlinear optical systems. In Ch. 4 we consider the enhanced nonlinearity for plasmons in graphene nanostructures. In Ch. 5 we theoretically analyze an all-optical single photon switch using slow light and cavity QED. Finally, in Ch. 6 we consider the few body physics of strongly interacting photons in Rydberg systems where we study the dynamics of two and three body bound states.

Chapter 2

Dynamic Nuclear Polarization in Double Quantum Dots

2.1 Introduction

The study of non-equilibrium dynamics of nuclei in solids has a long history (Abragam and Goldman, 1978) and has become particularly relevant as nanoscale engineering and improvements in control allow to probe mesoscopic collections of nuclear spins (Yusa et al., 2005; Dixon et al., 1997; Salis et al., 2001; Ono and Tarucha, 2004; Koppens et al., 2008; Bracker et al., 2005; Lai et al., 2006). This control has direct applicability to quantum information science, where nuclear spins are often a main source of dephasing (Hanson et al., 2007). The goal of developing an understanding of electronic control of nuclei is to circumvent this nuclear dephasing and to turn nuclear spins into a useful resource (Klauser et al., 2008), as indicated in recent experiments (Reilly et al., 2008b; Foletti et al., (2008, 2009; Bluhm et al., 2010, 2011;

Shulman et al., 2012; Frolov et al., 2012).

Double quantum dots in III-V semiconductors can be operated with two electrons coupled to approximately 10^4 to 10^6 nuclei by the contact hyperfine interaction. Repeated cycles transitioning from the electronic singlet to triplet states can be used to polarize the nuclear spins; electron spin flips between the singlet and triplet spaces occur due to the difference $\mathbf{D}$ in the Overhauser fields on the two dots (Petta et al., 2008). Early experimental (Reilly et al., 2008b) and theoretical (Ramon and Hu, 2007; Ribeiro and Burkard, 2009; Yao and Luo, 2010; Stopa et al., 2010) work suggested that the polarization process naturally drove the projection of the difference field onto the magnetic field axis D_z to zero. However, later experiments and theory both showed that the polarization is naturally accompanied by a growth in D_z and that the data in the original experiments showing a suppression in D_z was likely misinterpreted (Foletti et al., 2009; Gullans et al., 2010). Instead the results are more consistent with the growth of a large D_z accompanied by a reduction in measurement contrast between singlet and triplet states, which makes it appear as if D_z is small (Barthel et al., 2012).

In this chapter we develop a model to describe the long time dynamics of the nuclear spins undergoing adiabatic pumping. These results are in good agreement with the experiments described above (Foletti et al., 2009; Shulman et al., 2012). The main conclusion from this work was that when the dots are different sizes the Overhauser field becomes larger in the smaller dot; thereby resulting in large difference fields. In the present work, we present a detailed theoretical analysis of these problems. We describe the theoretical methods developed to study this system, including a novel method for efficient simulation of semiclassical central spin problems, and detail the experimentally relevant polarization phenomena we find in our model. The main results of the present work are that when nuclear spin noise is included, the more detailed theory presented here agrees with the results of Gullans et al. (2010); however, in the absence of nuclear spin noise, states with $D_z = 0$ can also be achieved for certain parameters.

Our theoretical methods are based on a semiclassical description of the nuclear spin dynamics in which the nuclear spins are grouped into small sets, each homogeneously coupled to the electron spin (Christ et al., 2007). The nuclei in each set may be treated as a single collective spin and a semiclassical treatment is justified provided the number of spins in each set remains large. Increasing the number of such sets improves the approximation to the true hyperfine coupling. More formally, we construct a systematic approximation to the true hyperfine coupling in terms of a reduced set of M coupling constants. For the optimal choice of coupling constants, we rigorously prove that our approximation reproduces the exact semiclassical time dynamics to within a fixed error for a time that increases linearly with M. For large M, this allows examination of the long timescales relevant for polarization experiments. This approach extends previous work that assumes that all nuclei on a given dot have equal coupling to the electron spin (Ramon and Hu, 2007; Ribeiro and Burkard, 2009; Yao and Luo, 2010; Stopa et al., 2010; Brataas and Rashba, 2011; Rudner and Levitov, 2012); an approach which often incorrectly predicts rapid saturation of the polarization. Other extensions to this homogenous coupling model, including semiclassical solutions for the central spin (Brataas and Rashba, 2012; Chen et al., 2007;

Al-Hassanieh et al., 2006; Tsyplyatyev and Loss, 2011), and cluster and diagramatic expansion techniques for short time non-equilibrium behavior (Witzel and Sarma, 2008; Wang et al., 2006; Coish and Loss, 2004) do not explore the wide range of time scales or relevant physics for the double dot case.

Our results can be broken up into two distinct cases depending on whether or not the dots are identical. When the dots are different sizes, then the hyperfine coupling, which scales inversely with the volume, is larger on the smaller dot and we find that the Overhauser field grows preferentially on the smaller dot as the polarization increases. This preferential growth results in a large Overhauser difference field D_z. For two dots with a difference in volume of less than $\sim 20\%$ we find a rich and complex phase diagram for the nuclear spin dynamics, which can be broken into two distinct regimes. The first regime occurs with large external magnetic fields or short cycle times. In this regime the system saturates without significant polarization because the perpendicular components of $\mathbf{D}$ rapidly approach zero and spin flips are suppressed; the system approaches a semiclassical "dark state." This occurs with no statistical change in the distribution of D_z. The second regime occurs in the limit of smaller magnetic fields or slower cycle times. In this regime, the dynamics are sensitive to the inclusion of nuclear spin noise. In the absence of nuclear spin noise we find one potential end state of polarization is a "zero state" in which all components of $\mathbf{D} \rightarrow 0$. In this state the singlet and triplet electronic subspaces are completely decoupled and spin flips no longer occur. Simultaneously, though, there are instabilities leading to the growth of large Overhauser difference fields. Crucially, when even a small amount of nuclear spin noise is added the zero states strongly destabilize and the system generically becomes unstable to the growth of large difference fields as shown by Gullans et al. (2010).

These results provide a clear picture of the polarization dynamics in such double quantum dot systems and will be a useful guide to future experiments aimed at more precise control of the nuclear spins. Although the paper is specific to double quantum dots in GaAs, many of the results and theoretical methods extend to other central spin systems under investigation (Takahashi et al., 2011; Sun et al., 2012; Högele et al., 2012). More generally, this work is of fundamental interest as we explore the dynamics of an interacting, many-body system when it is far from equilibrium (Urbaszek et al., 2013).

The paper is organized as follows. In section 2 we define the Hamiltonian for the double dot system and introduce the polarization cycle. In section 3 we systematically derive a semiclassical model for the nuclear spins starting from the coarse-grained evolution of the nuclear spin density matrix. In section 4 we present our results for identical and unequal dots in the presence and absence of nuclear spin noise. In appendix A.1 we provide a summary of the parameters used in our simulations. In appendix A.2 we describe our approach to coarse graining the electron wave function and provide rigorous bounds on the error in time evolution due to the course graining. In appendix A.3 we extend our simulations to the case of multiple nuclear species and find qualitatively the same results as for a single species.

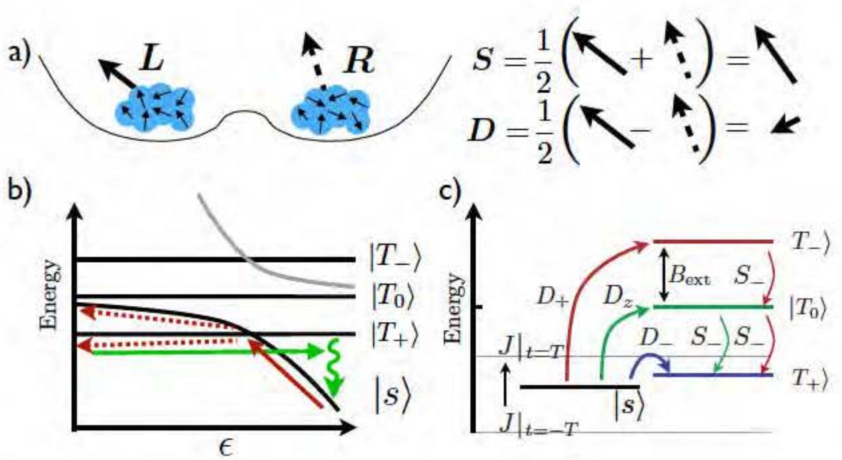

Figure 2.1: a) The Overhauser field in each dot gives rise to sum and difference fields which are relevant for the double dot system. b) Schematic of two-electron energy levels as a function of detuning ε between (1,1) and (0,2) charge states. Arrows indicate adiabatic sweep through avoided crossing (pink) and rapid sweep back to (0,2) with reload (green). c) Spin-flip pathways between the s and T_+ states as the exchange energy $J(\varepsilon)$ is swept through the crossing, showing the nuclear operators involved in each path. Each pathway is a term in $\tilde{D}_-$ in Eq. 2.2.

2.2 Setup

For a double quantum dot with two electrons, we can write the Hamiltonian for the lowest energy $(1,1)$ and $(0,2)$ electron states, where (n,m) indicates n (m) electrons in the left (right) dot. To model nuclear polarization, we first derive an effective two-level Hamiltonian to describe the system near the crossing of the singlet s and lowest energy triplet state, T_+, of this two-electron system, then solve the time dynamics. Dynamic nuclear polarization (DNP) experiments operate near this crossing, typically with an adiabatic sweep of the difference in the dots electric potential through the s-T_+ degeneracy (Fig. 2.1a), followed by a non-adiabatic return to (0,2) and reset of the electronic state via coupling to leads.

If $\psi_d(\mathbf{r})$ is the single-particle envelope wave function on dot $d = l,r$ (for the left, right dot), the effective hyperfine coupling for the nuclear spin at $\mathbf{r}_{kd}$ is $g_{kd} = a_{hf} v_0 |\psi_d(\mathbf{r}_{kd})|^2$ where a_{hf} is the hyperfine coupling constant, and v_0 is the volume per nuclear spin. We introduce two collective nuclear spin operators to denote the Overhauser fields in the left ($\hat{\boldsymbol{L}}$) and right ($\hat{\boldsymbol{R}}$) dots, $\hat{\boldsymbol{L}} = \sum_k g_{kl} \mathbf{I}_{kl}$ and $\hat{\boldsymbol{R}} = \sum_k g_{kr} \mathbf{I}_{kr}$, and further define $\hat{\boldsymbol{S}} = (\hat{\boldsymbol{L}} + \hat{\boldsymbol{R}})/2$, $\hat{\boldsymbol{D}} = (\hat{\boldsymbol{L}} - \hat{\boldsymbol{R}})/2$, where $\mathbf{I}_{kd}$ is the angular momentum of the kth nucleus on dot d. The rms Overhauser energy in the infinite temperature ensemble is $\Omega_d = (\sum_k g_{kd}^2 I(I+1)/3)^{1/2}$ where I is the magnitude of each nuclear spin. We define $\Omega = \sqrt{(\Omega_\ell^2 + \Omega_r^2)/2}$, and work in energy and magnetic field units such that $\Omega = -\frac{g^* \mu_B}{\hbar} = 1$, where g^* is the electron effective g-factor and μ_B is the Bohr magneton. In the basis $\{|s\rangle, |T_+\rangle, |T_0\rangle, |T_-\rangle\}$, where the T_m are the $(1,1)$ triplet states and s is the $(1,1)$-$(0,2)$ hybridized singlet state, the Hamiltonian is (Taylor et al., 2007)

$$H = \begin{pmatrix} -J(\varepsilon) & v\hat{D}_+ & -\sqrt{2} v \hat{D}_z & -v\hat{D}_- \\ v\,\hat{D}_- & -B_{\text{ext}} + \hat{S}_z & \hat{S}_-/\sqrt{2} & 0 \\ -\sqrt{2} v \hat{D}_z & \hat{S}_+/\sqrt{2} & 0 & \hat{S}_-/\sqrt{2} \\ -v\hat{D}_+ & 0 & \hat{S}_+/\sqrt{2} & B_{\text{ext}} - \hat{S}_z \end{pmatrix}.$$

where $D_\pm \equiv D_x \pm i D_y$ and similarly for $S_\pm$, B_{ext} is an external magnetic field, $v = v(\varepsilon) = \cos\theta(\varepsilon)/\sqrt{2}$, and $\cos\theta(\varepsilon)$ is the overlap of the (1,1) singlet state with the (1,1)-(0,2) hybridized singlet state $|s\rangle$. The parameters $\cos\theta(\varepsilon)$ and $J(\varepsilon)$, the splitting between s and T_0, are both functions of the energy difference ε between the $(1,1)$ and $(0,2)$ charge states. Here the nuclear spin variables refer to the full quantum mechanical operators on the nuclear spin space. In appendix A.3 we will consider the case of multiple nuclear species, but for now we consider the nuclei to be spin-3/2 of a single species, in a frame rotating at the nuclear Larmor frequency.

Assuming that $J, B_{\text{ext}} \gg \Omega$, we perform a formal expansion in the inverse electron Zeeman energy operator $\hat{m} = \Omega/(B_{\text{ext}} - \hat{S}_z + i\eta)$ where $\eta > 0$ is infinitesimal. We apply a unitary transformation that rotates the quantization axis of the triplet states to align with $\mathbf{B}_{\text{ext}} - \hat{\mathbf{S}}$ and find the Hamiltonian for the $\{|s\rangle, |T_+\rangle\}$ subspace to first order in J^{-1}, $\hat{m}$:

$$H_{\text{eff}} = \begin{pmatrix} -J(\varepsilon) + \hat{h}_s & v(\varepsilon)\tilde{D}_+ \\ v(\varepsilon)\tilde{D}_- & -B_{\text{ext}} + \hat{h}_T \end{pmatrix}, \tag{2.1}$$

where the effect of coupling to the higher energy states $|T_0\rangle$ and $|T_-\rangle$ enters as

$$\begin{aligned} \hat{h}_s &= -\frac{2v^2}{J}\tilde{D}_z^\dagger \tilde{D}_z - \tilde{D}_- \frac{v^2}{J + B_{\text{ext}} - \hat{S}_z}\tilde{D}_+, \\ \hat{h}_T &= \hat{S}_z - \frac{1}{4}(\hat{S}_-\hat{S}_+\hat{m} + \hat{m}\hat{S}_-\hat{S}_+), \\ \tilde{D}_- &= \hat{D}_- + \hat{m}\hat{S}_-\hat{D}_z - \frac{1}{4}\hat{m}\hat{S}_-^2\hat{m}\hat{D}_+ - \frac{1}{4}\hat{m}\,\hat{S}_-\hat{S}_+\hat{m}\hat{D}_-, \\ \tilde{D}_z &= \hat{D}_z - \frac{1}{2}\big(\hat{S}_+\hat{m}\,\hat{D}_- + \hat{S}_-\hat{m}\hat{D}_+\big). \end{aligned} \tag{2.2}$$

Of particular interest is that the off-diagonal term, which produces nuclear polarization, vanishes in the semiclassical limit of $\langle\hat{\mathbf{D}}\rangle \to 0$, i.e., in the zero states.

2.3 Model

We develop a model for the evolution of the nuclear spin density matrix after one pair of electrons has cycled through the system. We approximate the sweep through the $|s\rangle$-$|T_+\rangle$ degeneracy as a Landau-Zener process, which we solve approximately for the effect on the nuclear system. By coarse-graining this evolution over a cycle we derive a master equation for the nuclear spins. Finally, we add the effects of nuclear dipole-dipole interactions and quadrupole splittings phenomenologically. The derivation presented here is complementary to that of Gullans et al. (2010) and results in the same equations of motion.

The electron system is prepared in $|s\rangle$ at large negative $t = -T/2$, where T is the total cycle time. We identify the (nuclear spin) eigenstates of the operator $\tilde{D}_+\tilde{D}_-$, labeled $|D_\perp\rangle$ with eigenvalues $D_\perp^2$. Since the components of h_s and h_T that do not commute with $\tilde{D}_+\tilde{D}_-$ are perturbatively small in m_0 and $1/J$, we approximate them by keeping only the diagonal components in the two-level-system subspace, sending $h_s \to \langle D_\perp|\,\hat{h}_s\,|D_\perp\rangle$ and $h_T \to \langle D'_\perp|\,\hat{h}_T\,|D'_\perp\rangle$ where $|D'_\perp\rangle \equiv D_\perp^{-1}\hat{\tilde{D}}_-\,|D_\perp\rangle$. In this limit, the off-diagonal part of H_{eff} in Eq. 2.1 produces standard Landau-Zener behavior, while the diagonal components of H_{eff} are simply phases picked up by the nuclei, depending on which electronic state is occupied. For initial state $|\Psi_0\rangle = |s\rangle \otimes |D_\perp\rangle$, the crossing either leaves the electronic state unchanged or flips an electron and nuclear spin to the state $|T_+\rangle \otimes |D'_\perp\rangle$. We note that $|D'_\perp\rangle$ is an eigenstate of $\tilde{D}_-\tilde{D}_+$ with eigenvalue $D_\perp^2$. The problem is now reduced to finding Landau-Zener solutions for each independent two-level system $\{|s\rangle\otimes|D_\perp\rangle,\, |T_+\rangle\otimes|D'_\perp\rangle\}$. We model the actual sweep of ε by a linear sweep of J so $J(t) = -2\beta^2 t + B_{\text{ext}}$, where $\beta = \sqrt{\frac{1}{2}\,|dJ(\varepsilon)/dt|\,|_{t=0}}$. We take $v(\varepsilon)$ to be constant, valid in the limit of large tunnel coupling, and assume $\beta \ll B_{\text{ext}}$ to ensure the applicability of Eq. 2.1. For moderate magnetic fields $v(\varepsilon) \sim 1/\sqrt{2}$, but it decreases at large magnetic fields as the (1,1)-(0,2) hybridized singlet state has a smaller overlap with (1,1) at the s-T_+ crossing.

After one cycle, $|\Psi_0\rangle$ evolves into $|\Psi_1\rangle = c_S\,|s\rangle \otimes |D_\perp\rangle + c_T\,|T_+\rangle \otimes |D'_\perp\rangle$. For $\beta^2 T \gg 1$, the standard Landau-Zener formula gives the flip probability as $p_f = 1 - \exp(-2\pi\omega^2)$, where $\omega = v\langle\tilde{D}_\perp\rangle/\beta$, and

$$\begin{aligned}
c_S &= \sqrt{1-p_f}\,\exp(-i\phi_S), \quad c_T = \sqrt{p_f}\,\exp(-i\phi_T) \\
\phi_S &\approx \int_{-T/2}^{T/2} h_S dt \\
\phi_T &\approx \int_{-T/2}^{t_0} h_S dt + (T/2 - t_0)h_T + \phi_{AD}(\omega),
\end{aligned} \tag{2.3}$$

where the crossing occurs at a time $t_0 \approx S_z/\beta^2$. We include in ϕ_T the phase picked up by following the adiabat, ϕ_{AD}. We approximate ϕ_{AD} by interpolating between the limits $\omega = v\langle\tilde{D}_\perp\rangle/\beta \to 0$ and $\omega \to \infty$, giving (Vitanov and Garraway, 1996)

$$\phi_{AD} = 2\pi\omega^2 + p_f \left\{ \omega^2 \left[1 - 2\pi + \log\left(\frac{\tau^2}{\omega^2}\right) \right] - \pi/4 \right\},$$

where $\tau = T\beta/2$. More accurate approximations can easily be taken into account within our formalism; however we find such corrections have a negligible effect on the long term polarization dynamics because the polarization process rapidly drives ω to small values.

We move from the independent two-level systems to the general case by noting that the components of $|\Psi\rangle$ depend only on the eigenvalue $D_\perp$ and on the polarization S_z (which we approximate as commuting). Since the eigenstates of $\tilde{D}_+\tilde{D}_-$ form a complete basis for the nuclear spin states we can define the complete operator

$\hat{p}_f = \sum_{D_\perp} p_f(D_\perp) |D_\perp\rangle \langle D_\perp|$, and similarly for $\hat{\phi}_S, \hat{\phi}_T$. The nuclear spin density matrix after each cycle is given by tracing over the electronic states. The nuclear density matrix evolution is then

$$\begin{aligned}\rho_n = {} & \sqrt{1-\hat{p}_f}e^{-i\hat{\phi}_S}\rho_{n-1}e^{i\hat{\phi}_S}\sqrt{1-\hat{p}_f} \\ & + \left(\tilde{D}_-\sqrt{\frac{\hat{p}_f}{\tilde{D}_+\tilde{D}_-}}e^{-i\hat{\phi}_T}\right)\rho_{n-1}\left(e^{i\hat{\phi}_T}\sqrt{\frac{\hat{p}_f}{\tilde{D}_+\tilde{D}_-}}\tilde{D}_+\right),\end{aligned}$$

where ρ_n is the nuclear density matrix after n cycles.

Rather than solve for the exact dynamics of the nuclear density matrix–still an intractably hard computational problem for any reasonable number of nuclear spins–we instead adopt an approximate solution to the problem using the P-representation for the density matrix as an integral over products of spin coherent states. From the thermal distribution, we choose such a spin coherent state and evolve it, where we interpret expectation values $\langle ... \rangle$ as being taken in that state. The ensemble of such trajectories represents the physical system (Al-Hassanieh et al., 2006).

We organize this calculation by noting that the components of the Landau-Zener model $(\hat{\phi}_S, \hat{\phi}_T, \hat{p}_f, \tilde{D}_\pm)$ are only functions of $\hat{\boldsymbol{L}}$ and $\hat{\boldsymbol{R}}$. A spin coherent state is entirely described by its expectation values $\mathbf{i}_{id} = \langle \mathbf{I}_{id} \rangle$. For the kth spin on the left dot, we expand the discrete time difference $\langle \mathbf{I}_{kl} \rangle_n - \langle \mathbf{I}_{kl} \rangle_{n-1}$ after n and $n-1$ cycles in the small parameter g_{kl}, giving an evolution equation

$$\frac{d\mathbf{i}_{kl}}{dt} = g_{kl}\sum_{\mu=1}^{3} P_{l,\mu}\left\langle i[\partial_{g_{kl}}\hat{L}_\mu, \mathbf{I}_{kl}]\right\rangle = g_{kl}\boldsymbol{P}_l \times \mathbf{i}_{kl}, \tag{2.4}$$

with

$$\boldsymbol{P}_l = \frac{1}{T}\left[\langle 1-\hat{p}_f\rangle\langle\boldsymbol{\nabla}_l\hat{\phi}_S\rangle + \langle\hat{p}_f\rangle\langle\boldsymbol{\nabla}_l\hat{\phi}_T\rangle - \mathrm{Im}(\boldsymbol{\gamma}_l)\right],$$

where $\boldsymbol{\nabla}_l = (\partial_{L_x}, \partial_{L_y}, \partial_{L_z})$ and

$$\boldsymbol{\gamma}_l = \left\langle \tilde{D}_+ \frac{\hat{p}_f}{\tilde{D}_-\tilde{D}_+}\boldsymbol{\nabla}_l\tilde{D}_-\right\rangle, \tag{2.5}$$

and similarly for $\mathbf{i}_{kr}$, $\mathbf{P}_r$, and $\boldsymbol{\gamma}_r$, with $\mathbf{L}$ replaced by $\mathbf{R}$. The factorization of expectation values is a natural consequence of our spin-coherent state approximation, as it explicitly prevents entanglement between spins. Thus we have an effective, semi-classical picture of nuclear spins precessing and being polarized by their interaction with the electron spin, integrated over one cycle.

We approximate the electron wavefunction as a piecewise-flat function with M levels, which we refer to as the annular approximation, as illustrated in Fig. 2.2a. Each annulus defines $\mathbf{I}_{nd} = \sum_{k\in n}\mathbf{i}_{kd}$, where the sum is over all nuclei with the same hyperfine coupling to the electron. Since g_k is identical for all $k \in n$, we can simply replace $\mathbf{i}_{kd}$ with $\mathbf{I}_{nd}$ in Eq. 2.4. Furthermore, I_n^2 is a conserved quantity, so we can study the evolution of $M \ll N$ spins in a reduced Hilbert space. The typical size of I_n is $\sim \sqrt{N/M} \gg 1$, which allows us to replace the spin-coherent states used above with semi-classical spins, and makes taking expectation values straightforward: all quantum operators can be replaced by their expectation values directly. The annular approximation should correctly describe the nuclear dynamics for a time scale given by the inverse of the difference between the g_k of adjacent annuli.

To illustrate, to *first order* in $m_0 = B_{\text{ext}}^{-1}$, for $d = l, r$,

$$\begin{aligned}\mathbf{P}_d = & p_f \lambda \left(\Lambda_+ \hat{z} - \Lambda_0 \mathbf{S}_\perp\right) + m_0 \Gamma_0 \frac{p_f D_z}{2\pi\omega^2} \hat{z} \times \mathbf{D} \\ & + \Gamma_R p_f \boldsymbol{\nabla}_d \phi_{AD} \mp \Big[\Gamma_0 \frac{\beta^2}{4\pi v^2} \text{Im}\left(\boldsymbol{\gamma}_l - \boldsymbol{\gamma}_r\right) \\ & + (1 - p_f\lambda/2)(\Delta_0 D_z \hat{z} + \Delta_- \mathbf{D}_\perp)\Big]\end{aligned} \tag{2.6}$$

where the top sign applies for $d = l$, $\mathbf{D}_\perp = (D_x, D_y, 0)$, $\mathbf{S}_\perp = (S_x, S_y, 0)$, $\lambda = 1 - 2t_0/T$ gives the shift in the location of the crossing, and Δ_0, Δ_-, Λ_+, Λ_0, Γ_R, and Γ_0 are constants depending on the details of the pulse cycle (see below). We have replaced operators by their expectation values and removed the angle brackets since we are now in the semiclassical limit. To leading order in m_0, $\text{Im}(\boldsymbol{\gamma}_l - \boldsymbol{\gamma}_r) = 2(\mathbf{D} \times \hat{z}) p_f / D_\perp^2$. It is clear from Eqs. 2.4-2.6 that all dynamics stop in the zero states with $\mathbf{D} = 0$, consistent with the idea that true saturation of polarization requires that all components of $\mathbf{D}$ be small. We will focus on the stability of such states in various parameter regimes. The equations of motion in Gullans et al. (2010) are found from Eq. 2.6 by including only the lowest order in ΩT and Ω/β, which is the limit of fast cycles and small spin flip probability per cycle, respectively.

First we outline the meanings of the parameters in the model. As indicated schematically in Fig. 2.2b, the Γ_0 term originates in the hyperfine flip-flop, the Δ_0 and Δ_- terms are the off-resonant effects of coupling from the singlet state to the T_0 and T_- states, respectively, Λ_0 comes from coupling between the T_+ and T_0 states, and Λ_+ comes from Knight shifts due to occupation of the T_+ state. To leading order in m_0, for a pulse sequence consisting of only the Landau-Zener sweep, with

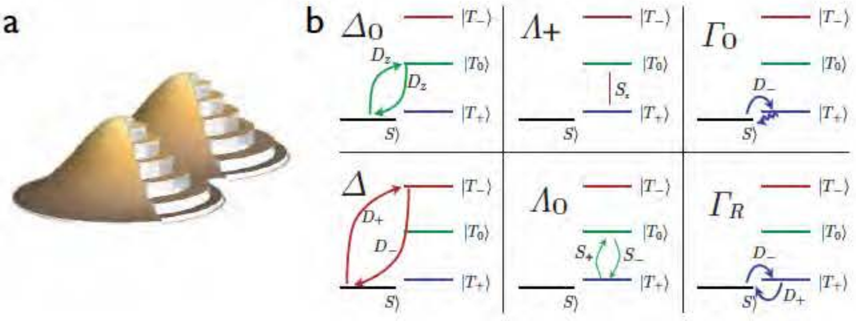

Figure 2.2: a) Independent Random Variable Annular Approximation (IRVAA) to the electron wavefunction in the double dot. b) Key processes contributing to Eq. 2.6.

instantaneous eject and reload, the parameters have values

$$\Delta_0 = \left\langle \frac{2v^2}{J(t)} \right\rangle_{\rm c} \approx m_0, \qquad \Delta_- = \left\langle \frac{v^2}{J(t) + B_{\rm ext}} \right\rangle_{\rm c} \approx m_0/4$$

$$\Lambda_+ = 1/4, \qquad \Lambda_0 = m_0/4$$

$$\Gamma_0 = \frac{2\pi v^2 f_c}{\beta^2}, \qquad \Gamma_R = f_c$$

where $f_c = 1/T$ is the cycle frequency and $\langle . \rangle_{\rm c}$ indicates an average taken over a full cycle; these values can be modified readily by changing the details of the pulse cycle, while leaving the Landau-Zener portion unchanged. In Appendix A.1 we provide a reference for all parameters used in the simulations.

Equation 2.4 is a good approximation of the nuclear dynamics over a few DNP cycles because other nuclear processes are slow compared to a typical experimental cycle (~10-100 ns (Reilly et al., 2008b)). However, the full DNP may last millions of cycles at which point these other nuclear processes become important. Apart from Larmor precession, which is only relevant for the case of multiple nuclear species considered in Appendix A.3, nuclear quadrupole splittings and nuclear dipole-dipole interactions are the dominant processes. They become relevant on a timescale of a few hundred microseconds in these systems (Taylor et al., 2007). We include them in our model phenomenologically by adding a fluctuating magnetic field $h_{kd}(t)$ in the z-direction at each site (the transverse terms are strongly suppressed by the external field), such that

$$\frac{d\boldsymbol{i}_{kd}}{dt} = g_{kd}\boldsymbol{P}_d \times \boldsymbol{i}_{kd} - \gamma_n\, h_{kd}\, \hat{z} \times \boldsymbol{i}_{kd} \tag{2.7}$$

where γ_n is the nuclear gyromagnetic ratio. We further assume that the this field can be treated as noise and characterized by a Gaussian, uncorrelated white noise spectrum

$$\gamma_n^2 \langle h^z_{kd}(t) h^z_{k'd'}(t') \rangle_n = 2\eta\, \delta(t-t')\delta_{kk'}\delta_{dd'} \tag{2.8}$$

where $\langle \cdot \rangle_n$ are averages over the noise (Reilly et al., 2008a).

2.4 Results

The polarization dynamics display three characteristic behaviors: growth of large difference fields, saturation in nuclear dark states defined by $D_\perp = 0$, and preparation in zero states $\boldsymbol{D} = 0$ which are global fixed points of the nuclear dynamics in the absence of noise. In Gullans et al. (2010) this system was studied in a restricted model focusing on the case where noise was present. Therein it was found that when the two dots have different hyperfine couplings the system generically grows large difference fields, while for identical dots, depending on parameters, the system is either unstable to the growth of large difference fields or saturates in dark states; however, the zero states were not found to be a relevant steady state in any parameter regime. In the present work we focus on extending the results of Gullans et al. (2010) to a larger, more experimentally relevant, parameter regime by using equations of motion correct to second order in m_0 with a more complete model of the Landau-Zener sweep as described in the previous section. In addition, we consider the nuclear dynamics in the absence of noise. We also present the full analytical calculations which were omitted from Gullans et al. (2010). In all *physical* parameter regimes we find qualitatively consistent results with Gullans et al. (2010); however, for a limited, *unphysical* parameter regime we do find solutions to the equations of motion in the absence of noise where the zero state is uniformly reached starting from a completely uncorrelated nuclear spin ensemble.

The simulations shown below were performed with the equations of motion correct to second order in m_0 with $\psi_d(\mathbf{r})$ a 2D Gaussian. Taking $v^2 \approx 1/2$, we estimate that for experiments performed with $B_{\text{ext}} = 10$ mT with $T = 25$ ns (Reilly et al., 2008b), $m_0 \approx 0.18$, $\Gamma_0 \approx 0.20$, but the Δ and Λ terms depend on the rest of the cycle. In each of the simulations, we choose initial magnitudes and directions of the spins $\mathbf{I}_n$ by a procedure equivalent to choosing initial directions for each of the N_n spin-3/2 nuclei in the nth annulus and evaluating $\mathbf{I}_n = \sum_{k \in n} \mathbf{i}_k$ explicitly (see Appendix A.2). The relationship between simulation time and laboratory time depends on the details of the pulse cycle, including pauses and reloads not considered explicitly here, but simulation time is roughly in units of g_{max}^{-1}, where $g_{max} \approx 2\Omega^2/a_{hf}$ is the largest value of g_k, so $t = 400$ is approximately 10 ms.

To organize our results we recall the phase diagram for identical dots and the

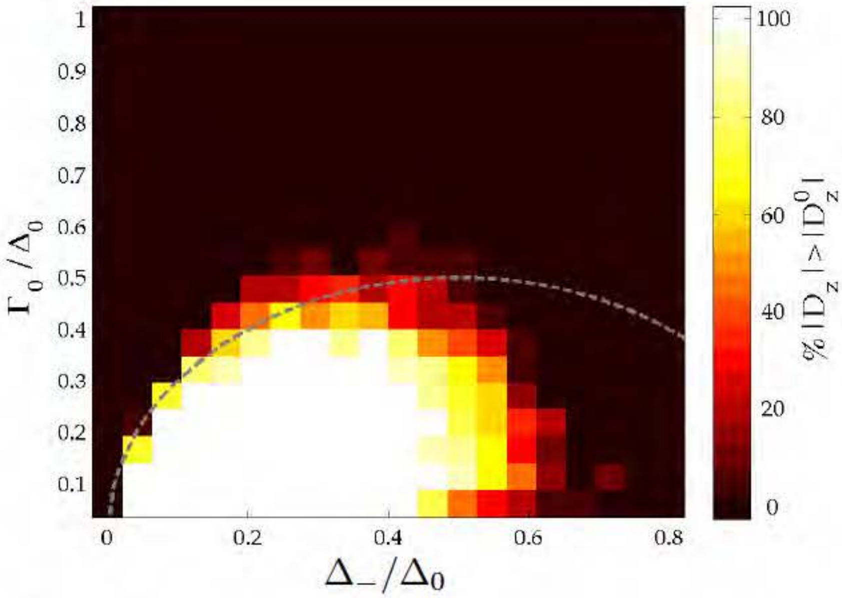

Figure 2.3: Phase diagram for the simplified model presented in Gullans et al. (2010). At each value of parameters, twenty runs were started with $D_z = -2$, $S_z = -10$, and all other components chosen randomly according to the infinite temperature ensemble. The colorscale indicates how many of those runs ended with $|D_z|$ increased. The dark region is of saturation and the light region is of instability. The dashed line shows the prediction of the simple model of Eq. 2.30, which captures the phase boundary, especially at low Δ_-/Δ_0. For parameters used, see Table I.

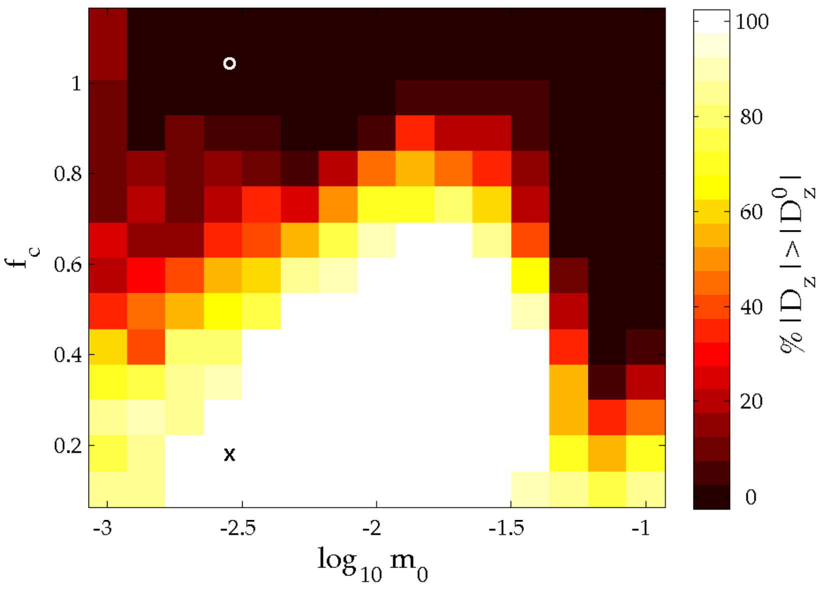

Figure 2.4: Phase diagram as in Fig. 2.3, except with varying external magnetic field and without any noise added. The parameters were scaled with m_0 as shown in Section III. There is a clear boundary between saturation at large Γ_0 and instability at lower values of Γ_0, with appropriately large values of Δ_0 and Δ_-. See Table I for parameters. The symbols 'x' and 'o' mark the parameters used for Fig. 2.7 below.

simplified model derived in Gullans et al. (2010) in which the only non-zero parameters are $\Delta_{0,-}$, Γ_0 and η, which corresponds to the limit of large magnetic fields and fast sweeps including nuclear spin noise. To obtain the phase diagram we consider for each set of parameters whether the system supports self-consistent growth of $|D_z|$ starting from large values of $|D_z|$ and $|S_z|$. This approach avoids complications with the metastability of zero states discussed later. Such simulations produce the phase diagram in Fig. 2b of Gullans et al. (2010), which is reproduced in Fig. 2.3 with the full data presented. From this figure it is clear that we can separate the dynamics into two regimes depending on parameters. For large ratios of Γ_0/Δ_0, which corresponds to large magnetic fields or strong pumping the system quickly saturates with no growth of large difference fields. For small ratios there is an instability towards large difference fields. In the first section we explore the dynamics in the absence of noise for identical dots with all parameters included. In the second section we include nuclear spin noise and asymmetry in the dot sizes.

2.4.1 Noise Free Nuclear Spins

From the general arguments given in the introduction it is clear that when the dots have different hyperfine couplings the system naturally grows a large difference field. Furthermore, in Gullans et al. (2010) it was shown that even identical dots display similar behavior in the presence of noise. In this section we analyze the case of identical dots in the absence of noise to better understand the role of the coherent nuclear dynamics. We begin by deriving a phase diagram analogous to the one obtained in the presence of noise except we now look in the space of the

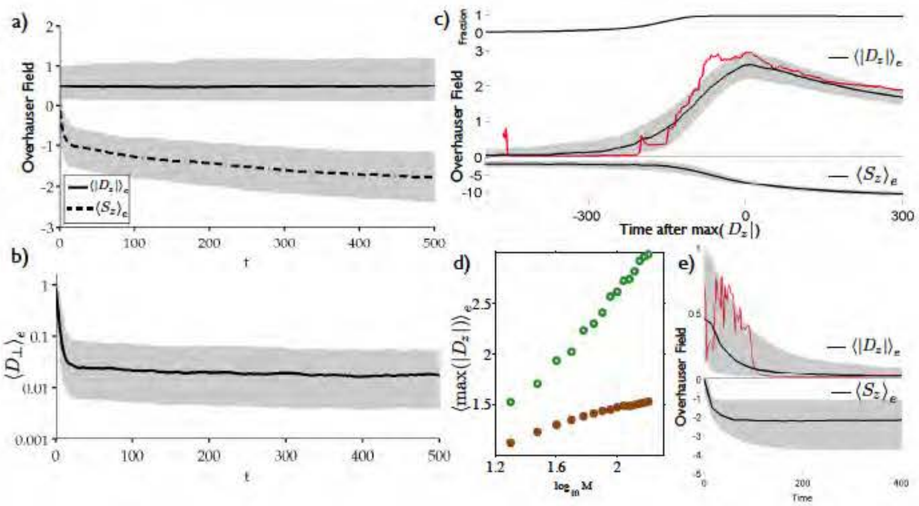

Figure 2.5: a-b) Simulations corresponding to the saturation region of the phase diagram. The solid lines are the median values of $|D_z|$ (a), S_z (a) and $D_\perp$ (b) at each time step in an ensemble of 1000 trajectories. In all plots shaded regions show the 84th and 16th percentiles. c) Simulations showing growth of $\langle|D_z|\rangle$ with the time shifted for each trajectory so that its maximum $|D_z|$ occurs at time zero. Bottom shows the median value of S_z $\langle S_z\rangle_e$ at each time step in an ensemble of 1000 trajectories. In the middle is similar $\langle|D_z|\rangle_e$. Thin red line is a single trajectory. The curve at top shows the fraction of trajectories contributing to the ensemble at each time; this increases with time because some trajectories reach their maximum D_z much later than others while the simulation time is fixed for each trajectory. 4.5% of the trajectories, which do not show this peak in $|D_z|$, are not included. Approximately 10% of the trajectories show behavior similar to that shown in the thin red line, where $|D_z|$ is reduced initially and then goes unstable to large $|D_z|$. d) Mean of the maximum value of $|D_z|$ reached on each trajectory for the same parameters as in (c) (open circles) except M varied between 20 and 160, with 5000 trajectories per point. Closed circles show similar results with $m_0 = 0.05$, $\tau = 4$ and all other parameters scaled appropriately. The physical system has $M \to N \approx 10^6$, so we interpret this as an instability to large $|D_z|$, which is supported by simulations including transverse noise (see section 2.4.2). e) With different parameters, simulations showing reduction of $\langle|D_z|\rangle$ plotted as in (c) without the time shift. For these parameters, the trajectories have $|D_z| \to 0$ quickly, without time for strong polarization.

experimentally accessible parameters cycle rate f_c and inverse magnetic field m_0. The results are shown in Fig. 2.4 where we see the same qualitative behavior as shown in Fig. 2.3. However, the dynamics are much richer than indicated by this simple phase diagram. In the following subsections we give examples of what happens to a nuclear spin ensemble starting from equilibrium for different parameters and regions of the phase diagram.

Before proceeding, however, we note that in the absence of noise the inhomogeneity of the electron wavefunction plays a crucial role. This is because weak inhomogeneity is equivalent to choosing the number of annuli M to be small and in this case the system moves rapidly to its maximally polarized state, with $\mathbf{I}_n \approx -I_n \hat{z}$ for all n. Dynamics completely cease in this state, as can clearly be seen from Eq. 2.4, despite the fact that this state does not correspond to all of the nuclei being polarized, which would also require $I_n = 3N_n/2$. On the other hand, for strong inhomogeneity, or large M, when the system is not fully polarized other terms in $\boldsymbol{P}_d$ compete with the polarization saturation and sustain the dynamics. (Christ et al., 2007)

Polarization Saturation

When the magnetic field is large or the cycle rate is fast (i.e., $\Delta_0 \ll \Gamma_0$), the system rapidly moves toward dark states (i.e., states with $D_\perp = 0$), sending $p_f \to 0$ without statistical change in the distribution of D_z, as shown in Fig. 2.5a. This limit is additionally characterized by only a small change in nuclear polarization as seen in Fig. 2.5b. When the effects of the $|s\rangle$-$|T_0\rangle$ coupling are important (i.e., $\Delta_0 \approx \Gamma_0$), the Δ_0 term in Eq. 2.6 causes $D_\perp$ to increase, “rebrightening” the $D_\perp \approx 0$ dark states and allowing dynamics to continue. Coupling from the singlet to the T_0 state is an essential ingredient in all of the effects discussed below. When Δ_0 is significant, dynamics only stop near zero states with $\mathbf{D} = 0$.

Growth of Difference Fields

Second, we observe the growth of large Overhauser fields. We consider a prototypical pulse sequence motivated by experiments with moderate/large magnetic field, $m_0 = 0.01$ In this case, over 95% of the trajectories display a growth in $|D_z|$, as shown in Fig. 2.5c. We observe this behavior over a range of experimentally accessible magnetic fields and cycle frequencies. This increase in $|D_z|$ indicates that the spin flips are occurring predominantly in one dot. We interpret these results as showing a continuing increase of $|D_z|$, where the peak of $|D_z(t)|$ is an artifact of the annular approximation. Near the peak, many of the annular spins artificially reach their maximal polarization, at which point they should be broken into more annuli. Similar trajectories with different M show the maximum value of $|D_z|$ increasing with M (Fig. 2.5d). The physical cause of this increase in $|D_z|$ is not clear, but it is associated with both Δ_0/Γ_0 and Λ_+/Γ_0 being sufficiently large. When nuclear spin noise is included, the growth in $\langle |D_z| \rangle_e$ continues (Gullans et al., 2010). This could be the same phenomenon as seen by Foletti et al. (2009), with transverse dephasing helping to produce the large $|D_z| \approx B_{\text{ext}}$ of that work, though unequal dot sizes could also produce that effect (Gullans et al., 2010).

Zero States

For moderate to small magnetic fields, when $\Delta_0 \approx \Gamma_0$, two different characteristic behaviors of particular note are observed. First, in the physical parameter regimes, which do not display general motion to zero states, the zero states are still important for the dynamics as they are a metastable state. That is, many trajectories spend a long time with $|D_z|$ near zero before escaping away to large $|D_z|$. This phenomenon is shown in the individual trajectory (thin red line) of Fig. 2.5c.

Second, for parameters in our model which are not experimentally accessible there is a mechanism that gives rise to attraction towards zero states. This is illustrated in Fig. 2.5e, where we show an ensemble of trajectories in which $\mathbf{D}$ rapidly reduces toward zero. For the parameters of Fig. 2.5e, the standard deviation of D_z was reduced by a factor of 28. We remark that as $\mathbf{D} \to 0$, the singlet state ceases mixing with the triplets and nuclear spin dynamics stop. Until something (outside this model, such as nuclear dipole-dipole coupling) restores $\mathbf{D}$, the polarization process is shut off, limiting the total nuclear polarization that can build up. While not shown in Fig. 2.5e, we observe a dramatic reduction of the total $|D|$, not just D_z, consistent with this qualitative observation. However, because we have not observed this phenomenon in any physical parameter regimes we shall not study it further.

Crossover

For many choices of parameters, we find both trajectories in which $D_z \to 0$ and $|D_z|$ remains large, depending on initial conditions, as shown in Fig. 2.6a. Note that when we add a small amount of transverse dephasing to these trajectories, as shown

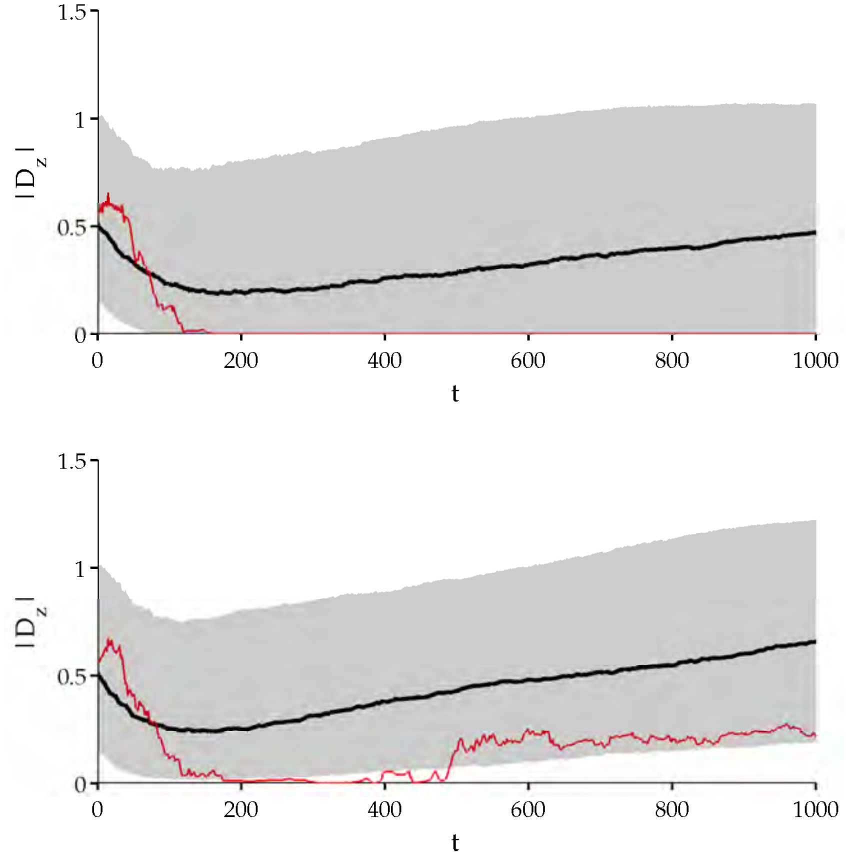

Figure 2.6: a) 1000 trajectories were run with initial conditions chosen from the thermal distribution with no noise. The mean value of $|D_z|$ is shown in black, and the the gray region enclosing 67% of the trajectories. A single trajectory is shown in the thin red line. For parameters, see Table 1. These parameters are not represented in the phase diagram since they have very large Λ_+. For these parameters, many trajectories are attracted near $D = 0$, as in the single trajectory shown, for extended periods of time. b) Trajectories were begun from identical configurations as in a, this time with noise added. With noise included, the metastability of the zero state is removed, and the gray region is now bounded away from zero.

in Fig. 2.6b, the median value of $|D_z|$ does not markedly change, but there are no longer trajectories with $D_z \to 0$; the noise apparently disrupts the fragile attraction toward $|D_z| \to 0$. Simulations performed with parameters intended to approximate experiments (Reilly et al., 2008b; Foletti et al., 2009) are in this crossover regime.

Stability of Zero States

We now investigate more carefully the stability of the zero states. Near the zero state the EOM are greatly simplified because many of the terms in $\boldsymbol{P}_d$ arise from perturbative processes involving multiple applications of $\boldsymbol{D}$. Keeping only the terms linear in $\boldsymbol{D}$ and working to first order in m_0 we can write

$$\dot{D}_+ = \big(\Gamma_0 + i\Delta_-\big)S_z^* D_+ + (\Gamma_0 m_0 S_z^* S_+ - i\Delta_0 S_+^*)D_z \tag{2.9}$$

$$\dot{D}_z = -\mathrm{Re}\big[(\Gamma_0 + i\Delta_-)D_+ S_-^*\big] - \Gamma_0 m_0 \boldsymbol{S}_\perp \cdot \boldsymbol{S}_\perp^* D_z, \tag{2.10}$$

where we have introduced the variable $\boldsymbol{S}^* = \sum_{kd} g_{kd}^2 \boldsymbol{I}_{kd}/2$. Because $d\boldsymbol{S}/dt, d\boldsymbol{S}^*/dt \sim O(D)$, we can neglect the time dependence of $\boldsymbol{S}$ and $\boldsymbol{S}^*$ in the EOM for $\boldsymbol{D}$ near the zero state. After a long time the system becomes polarized so that $S_z^* \ll 0$, this allows us to adiabatically eliminate D_+ to obtain

$$D_+ = \frac{-i\Delta_0 S_+^* + m_0 \Gamma_0 S_z^* S_+}{(\Gamma_0 + i\Delta_-)\,|S_z^*|} D_z + O(D^2) \tag{2.11}$$

$$\dot{D}_z = 0 + O(D^2) \tag{2.12}$$

This linear stability analysis gives no conclusion about the stability of the zeros states. This result implies that within this model the stability of the zero state is only determined at higher order. This is a little surprising because at first glance Eq. 2.10 appears to have an attractive force towards $D_z = 0$. This arises from the same mechanism described by Stopa et al. (2010); however, a more careful treatment reveals that this effect actually cancels. Our simulations indicate that the nonlinear corrections make the zero state repulsive in the experimentally relevant parameter regimes. When we include the nuclear spin noise we shall show analytically that the system is repelled from the zero states.

2.4.2 Effect of Nuclear Spin Noise

Unequal Dots

Our results that zero states are unstable to the growth of large difference fields in the presence of asymmetry in the size of the dots and nuclear noise can be be understood in the following heuristic picture first given by Gullans et al. (2010). We assume the nuclear spins have equal spin flip rates on the two dots, which is borne out by the analytical and numerical calculations presented below. Then the build-up of the total Overhauser field S_z is proportional to $-(g_\ell + g_r)$, where $g_{\ell(r)}$ are the effective hyperfine interactions on the left (right) dot and the negative sign arise because nuclear spins are flipped down in the experimental cycles. Similarly D_z grows as $-(g_\ell - g_r)$ so that the ratio

$$D_z/S_z \to (g_\ell - g_r)/(g_\ell + g_r). \tag{2.13}$$

In this section we demonstrate a similar result within our full model. We assume

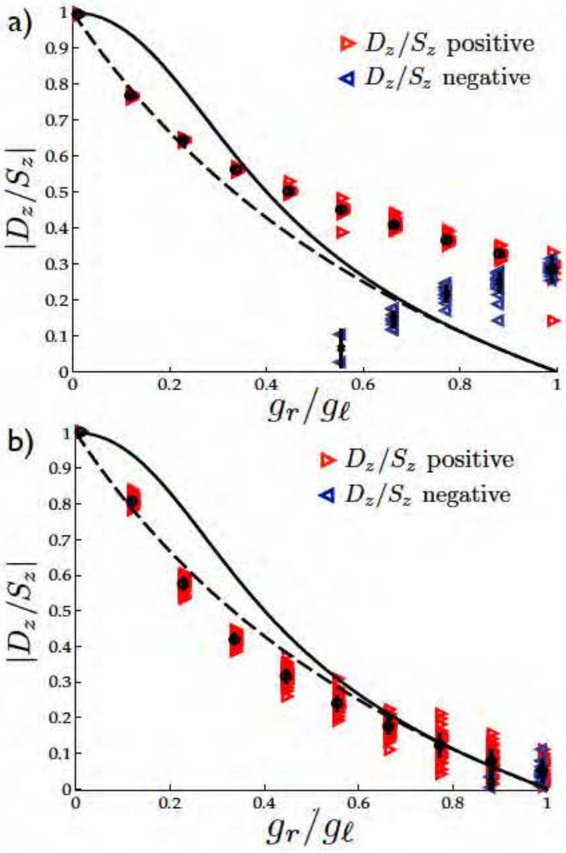

Figure 2.7: a) Asymptotic value of $|D_z/S_z|$ as a function of dot asymmetry with parameters chosen as in the location marked with an x in Fig. 2.4, strongly in the instability regime. The horizontal access corresponds to the left dot decreasing in size from right to left, which, by our simple argument, should result in a positive ratio of D_z/S_z. Trajectories which show the opposite sign indicate a competition with the coherent instability mechansim. For each value of dot asymmetry R, we initialized fifty runs in a single initial spin configuration chosen from the thermal distribution (with $D_z = -0.72$ and $S_z = -1.57$). We plot the asymptotic value of D_z/S_z. The runs that ended with D_z/S_z greater (less) than 0 shown are shown as red (blue) points. The circles (crosses) indicate the mean value of the red (blue) points, with error bars showing the standard deviations. The solid and dashed lines are given by Eq. 2.24 and Eq. 2.13, respectively. b) As in (a), with parameters chosen in the location marked with an o in Fig. 2.4, strongly in the saturation regime. Here the sign of the ratio D_z/S_z follows what is expected from the natural asymmetry.

homogeneous coupling and work in the high field, large J, limit where we can set $\Delta_0 = \Delta_- = 0$ in $\mathbf{P}_d$. The local noise processes included in Eq. 2.7 give rise to a mean decay of the collective nuclear spin variables and associated fluctuations $\mathcal{F}_{\ell(r)}$, for $\dot{L}_+(\dot{R}_+)$, defined by $\langle \mathcal{F}_d(t)\, \mathcal{F}^*_{d'}(t')\rangle_n = 2\Omega_d^2\, \delta_{dd'}\delta(t-t')$. The semiclassical EOM for the nuclear spins reduce to

$$\dot{L}_+ = g_\ell \Gamma_0\, L_z(L_+ - R_+)/2 - \eta\, L_+ + \sqrt{2\eta}\,\mathcal{F}_\ell, \tag{2.14}$$

$$\dot{L}_z = -\frac{g_\ell}{2}\Gamma_0\left(L_\perp^2 - \mathbf{R}_\perp \cdot \mathbf{L}_\perp\right), \tag{2.15}$$

and similarly for $\mathbf{R}$, where η is defined in Eq. 2.8. From Eq. 2.14, we see that if we start in a zero state, $\mathcal{F}_d$ will produce a fluctuation in $D_\perp$, and the contribution to $\dot{L}_z$ of the form $-g_\ell\Gamma_0 L_\perp^2$ results, in the long time limit, in $L_z \ll -1$ and similarly for R_z. Thus, $|\dot{L}_z/L_z| \ll 1$ and we can treat L_z, R_z as static to find $\langle L_\perp^2\rangle_n$, $\langle R_\perp^2\rangle_n$ and $\langle \mathbf{L}_\perp \cdot \mathbf{R}_\perp\rangle_n$, which allow us to find the slow evolution of L_z, R_z.

In particular, assuming L_z, R_z are constant we can write the closed set of equations for L_+ and R_+

$$\begin{aligned}\begin{pmatrix} \dot{L}_+ \\ \dot{R}_+ \end{pmatrix} &= \frac{\Gamma_0}{2}\begin{pmatrix} g_\ell L_z & -g_\ell L_z \\ -g_r R_z & g_r R_z \end{pmatrix}\begin{pmatrix} L_+ \\ R_+ \end{pmatrix} \\ &\quad - \eta \begin{pmatrix} L_+ \\ R_+ \end{pmatrix} + \sqrt{2\eta}\begin{pmatrix} \mathcal{F}_\ell \\ \mathcal{F}_r \end{pmatrix}\end{aligned} \tag{2.16}$$

Introducing the variables

$$\begin{pmatrix} \tilde{S}_+ \\ D_+ \end{pmatrix} = \frac{1}{2} \begin{pmatrix} -1 & -\frac{g_\ell L_z}{g_r R_z} \\ 1 & -1 \end{pmatrix} \begin{pmatrix} L_+ \\ R_+ \end{pmatrix} \tag{2.17}$$

we find

$$\tilde{S}_+(t) = -\sqrt{\frac{\eta}{2}} \int_{-\infty}^{t} dt' e^{-\eta(t-t')} \big(\mathcal{F}_\ell + \frac{g_\ell L_z}{g_r R_z} \mathcal{F}_r\big), \tag{2.18}$$

$$D_+(t) = \sqrt{\frac{\eta}{2}} \int_{-\infty}^{t} dt' e^{-(\eta+\gamma_S)(t-t')} (\mathcal{F}_\ell - \mathcal{F}_r) \tag{2.19}$$

here $\gamma_S = -\Gamma_0(g_\ell L_z + g_r R_z)/2 > 0$. We can use this solution to calculate $\langle L_\perp^2 \rangle_n$, $\langle R_\perp^2 \rangle_n$, and $\langle \boldsymbol{L}_\perp \cdot \boldsymbol{R}_\perp \rangle_n$. For example to lowest order in $1/L_z$, $1/R_z$

$$\begin{aligned} \langle L_\perp^2 \rangle_n &= \frac{4\eta/\bar{g}}{(1+p)^2} \\ &\times \Big(\frac{g_\ell + g_r p^2}{2\eta} + \frac{(g_\ell + g_r)p^2}{2\gamma_S} + \frac{2p(g_\ell - g_r p)}{\gamma_S} \Big), \end{aligned} \tag{2.20}$$

where we have defined $p = g_\ell L_z / g_r R_z$, $\bar{g} = (g_\ell + g_r)/2$ and used the fact that $\Omega_d^2 = g_d/\bar{g}$ in our units.

Inserting this solution into the EOM for D_z, S_z gives reduced EOM for the slow, noise-averaged evolution of D_z and S_z. After some straightforward manipulations we arrive at

$$\begin{pmatrix} \dot{S}_z \\ \dot{D}_z \end{pmatrix} = \frac{g_\ell \, \eta}{2\bar{g}} \frac{g_\ell \, g_r}{|S_2^z|^2} \; E \begin{pmatrix} S_z \\ D_z \end{pmatrix} \tag{2.21}$$

where $S_2^z = (g_\ell L_z + g_r R_z)/2 = -\gamma_S/\Gamma_0$ and

$$E = \frac{1}{4R}\begin{pmatrix} (1+R)(1-R^2) & (1-R)^3 \\ (1-R)(1+R)^2 & -(1+R)(1-R^2) \end{pmatrix} \tag{2.22}$$

and $R = g_r/g_\ell$. After rescaling time to

$$\tau = \int_0^t dt' \, \frac{g_\ell \, \eta}{\bar{g}} \frac{g_\ell \, g_r}{|S_2^z(t')|^2} \tag{2.23}$$

this becomes a purely linear system characterized by the matrix E. For all $R > 0$, this matrix has one positive and one negative eigenvalue; thus, it has one growing mode and one decaying mode. In the long time limit, both S_z and D_z will be proportional to their overlap with the growing mode. Thus D_z/S_z approaches a constant, which is easily found from E as

$$\frac{D_z}{S_z} \to \frac{1-R^2}{2R + \sqrt{4R^2 + (1-R)^4}}. \tag{2.24}$$

In Fig. 2.7 we compare this result and Eq. 2.13 to the full numerics including all the parameters. The horizontal access corresponds to the left dot decreasing in size from right to left, since $D_z/S_z \sim (g_\ell - g_r)/(g_\ell + g_r)$ according to our simple argument we expect this to result in a positive ratio of D_z/S_z. In Fig. 2.7a, however, we see that for small asymmetry $g_r/g_\ell > 0.5$, many trajectories have the opposite sign indicates that in this regime the coherent instability mechanism (which does not prefer either sign) competes with the natural asymmetry. For larger asymmetries $g_r/g_\ell < 0.5$ all trajectories are seen to follow the direction of the natural asymmetry.

Fig. 2.7b shows the same simulations performed in the saturation regime. As there is no coherent instability mechanism competing with the dot asymmetry, the sign of D_z is determined by the asymmetry in all but the most symmetric dots. D_z/S_z is in good agreement with the simple prediction given by Eq. 2.13 and Eq. 2.24.

Identical Dots

For identical dots the arguments given in the previous subsection break down; however, we shall now show that for certain parameters there still exists a mechanism for self-consistent growth of $|D_z|$. Growth of $|D_z|$ requires nonzero $D_\perp$. For intermediate field and exchange, the $\Delta_{0,-}$ contributions to $\boldsymbol{P}_d$ become comparable to the Γ_0 term. In particular, the $\Delta_0 D_z \hat{z}$ term acts as a source term for $D_\perp$ (see Eq. 2.25). Consequently, for weak enough noise $D_\perp$ will only be appreciable when $|\Delta_0 D_z/\Gamma_0 S_z|$ is appreciable, which provides a self-consistency condition for the continued growth of D_z.

These properties of identical dots can be seen analytically in the following limiting case: we assume a wave function where the coupling takes two values, $g_1 \gg g_2, \eta$ and that initially $-g_2 S_z \gg g_1 |D_z| \gg g_1$, $S_\perp \sim 1$ and $D_\perp \sim D_z/S_z \ll 1$. We denote the *total* angular momentum of nuclear spins in dot d with coupling constant g_k by $\boldsymbol{J}_{kd}$ and assume $J_{1d}^\perp \sim J_{2d}^\perp \sim J_{2d}^z \ll J_{1d}^z$ so that the majority of the polarization resides in the strongly coupled spins. We can write a closed set of equations for the evolution of $\boldsymbol{D}$ and $\boldsymbol{S}$

$$\begin{aligned}
\dot{D}_+ &= g_1 i\tilde{\Delta}_- S_z D_+ - g_1 i\Delta_0 D_z S_+ \\
&\quad + g_2\,\delta\, i\,\Delta_0 D_z (J_{2\ell}^+ + J_{2r}^+)/2 - g_2\,\delta\, i\tilde{\Delta}_-\, D_+(J_{2\ell}^z + J_{2r}^z)/2, \\
\dot{S}_+ &= -g_1 i(\Delta_0 - \tilde{\Delta}_-) D_z D_+ + g_2\,\delta\, i\,\Delta_0 D_z (J_{2\ell}^+ - J_{2r}^+)/2 \\
&\quad - g_2\,\delta\, i\,\tilde{\Delta}_- D_+ (J_{2\ell}^z - J_{2r}^z)/2, \\
\dot{D}_z &= g_1\,\mathrm{Im}\big[\tilde{\Delta}_- D_+ S_-\big] - g_2\,\delta\,\mathrm{Im}\big[\tilde{\Delta}_- D_+ (J_{2\ell}^- + J_{2r}^-)/2\big], \\
\dot{S}_z &= -g_1 \Gamma_0 D_\perp^2 - g_2\,\delta\,\mathrm{Im}\big[\tilde{\Delta}_- D_+ (J_{2\ell}^- - J_{2r}^-)/2\big], \\
\dot{J}_{2d}^+ &= \pm g_2 i\Delta_0 D_z J_{2d}^+ \mp g_2 i\tilde{\Delta}_- D_+ J_{2d}^z - \eta J_{2d}^+ + f_d, \\
\dot{J}_{2d}^z &= \pm g_2\,\mathrm{Im}\big[\tilde{\Delta}_- D_+ J_{2d}^-\big],
\end{aligned}$$

where the top sign is for $d = \ell$, $\tilde{\Delta}_- \equiv \Delta_- - i\Gamma_0$, $\delta \equiv g_1 - g_2$, f_d is a gaussian, white noise process derived analogously to $\mathcal{F}_d$ such that $\langle f_d f_d^* \rangle_n = 2\eta\sigma^2$, and we have neglected to write the noise terms in the EOM for D_+ and S_+ because we have assumed they are higher order. Furthermore, we can neglect all terms proportional to $g_2 D_+ J_{2d}^\mu$ because these are second order. This leads to the somewhat simpler set of equations

$$\dot{D}_+ = g_1 i\tilde{\Delta}_- S_z D_+ - g_1 i\Delta_0 D_z S_+ \tag{2.25}$$

$$+ g_2\,\delta\,i\,\Delta_0 D_z (J_{2\ell}^+ + J_{2r}^+)/2,$$

$$\dot{S}_+ = -g_1 i(\Delta_0 - \tilde{\Delta}_-) D_z D_+ \tag{2.26}$$

$$+ g_2\,\delta\,i\,\Delta_0 D_z (J_{2\ell}^+ - J_{2r}^+)/2,$$

$$\dot{J}_{2d}^+ = \pm g_2 i\Delta_0 D_z J_{2d}^+ - \eta J_{2d}^+ + f_d, \tag{2.27}$$

$$\dot{D}_z = g_1\,\mathrm{Im}\big[\tilde{\Delta}_- D_+ S_-\big] \tag{2.28}$$

$$\dot{S}_z = -g_1 \Gamma_0 D_\perp^2, \tag{2.29}$$

These equations can be solved perturbatively in $1/S_z$,$1/D_z$ by the same method as in the previous section. The only difference in the structure of the two problems is that in this case the source terms for D_+ and S_+ are proportional to J_{2d}^+ instead of white noise; as a result we have to take into account the coherent evolution of the source term. We can expand the resulting EOM for D_z in $g_1 D_z/g_2 S_z$ to find the noise-averaged equation

$$\begin{aligned}\dot{D}_z = &-g_1\Gamma_0 2\,\delta^2\sigma^2\left(\frac{\Delta_0^2}{\Gamma_0^2+\Delta_-^2}\right)\\ &\times\frac{\left(\Gamma_0^2+\Delta_-^2-\Delta_0\Delta_-\right)}{\Gamma_0^2+\Delta_-^2}\,\frac{g_1}{g_2}\left(\frac{D_z}{|S_z|}\right)^3\end{aligned} \tag{2.30}$$

from which we see that the sign of $\Gamma_0^2 + \Delta_-^2 - \Delta_0\Delta_-$ determines whether or not there is continued growth of D_z. Note that the perturbation theory breaks down as $g_2 \to 0$. This reflects the importance of including the coherent evolution of J_{2d}^+ in solving for

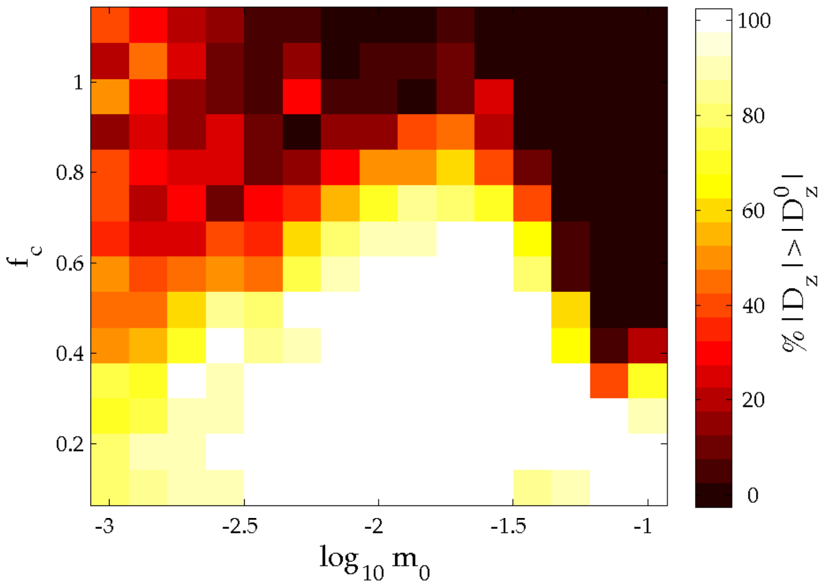

Figure 2.8: Phase diagram as in Fig. 2.4 except with noise added. The phase diagram is nearly identical. See Table I for parameters.

the dynamics. Without g_2, we would have found $\dot{D}_z = 0$. This phase boundary is shown as the dashed line in Fig. 2.3. In Fig. 2.8 we show the phase diagram as a function of cycle frequency and inverse magnetic field, where we see qualitatively the same behavior as Fig. 2.4.

2.5 Relevance to Other Central Spin Systems

Although this work has focused on lateral double quantum dots in GaAs, the methods, and some of the results, can be applied to vertical double dots (Takahashi et al., 2011), InAs quantum dots (Sun et al., 2012; Högele et al., 2012), silicon based quantum dots (Maune et al., 2012), and NV-centers in diamond (Childress et al., 2006). A few important differences for these other central spin systems are that the sign of the electron g-factor may be positive (compared to its negative sign in GaAs) and the spin-orbit coupling can be much larger in other systems than it is in GaAs (Stepanenko et al., 2012). The results presented in the paper are not dependent on the sign of the g-factor. Changing the sign would reverse the direction of the nuclear polarization from negative to positive, but all of our analysis would carry through essentially unchanged. The competition between spin-orbit coupling and DNP is more dramatic and can have a qualitative effect on the polarization dynamics for large spin-orbit coupling (Rudner and Levitov, 2010).

2.6 Conclusions

We have shown that dynamic nuclear polarization experiments in double quantum dots give rise to a rich set of phenomena. We find that after many thousands of nuclear spin pumping cycles, corresponding to experimental timescales of several hundred microseconds, the total nuclear polarization is driven to $10-30\%$ of full polarization. The polarization is aligned opposite the magnetic field as opposed to the thermal polarization. In addition to this large polarization, we find the competition between polarization, noise processes and coherent evolution mediated by the electrons allows one to carefully control the final nuclear spin state in the two dots. We have developed detailed numerical and analytical methods to theoretically describe such dynamics; however, our analysis is semiclassical and leaves out effects such as spin-orbit coupling and a full description of the nuclear dipole-dipole interactions (which we approximate as nuclear spin noise), both of which may be important for a complete understanding of the experiments.

The main implication of the paper for DNP experiments in double dots is that the nuclear spin dynamics are dominated by either rapid saturation of polarization or an instability to the growth of large difference fields. These results are consistent with the experimental observations reported in Petta et al. (2008), Foletti et al. (2009) and Barthel et al. (2012); however, we see evidence that the dynamics are much richer as the experiments have not resolved whether or not the instability to large difference fields results from dot asymmetry or coherent electron-nuclear interactions. These two cases could be experimentally distinguished by measuring the sign of D_z in a given double dot. Furthermore, we showed that the zero states may be experimentally observable as metastable states in certain parameter regimes, indicating that there is still much to explore in the polarization dynamics of double quantum dots.

Chapter 3

Nanoplasmonic Lattices for Ultracold Atoms

3.1 Introduction

Coherent optical fields provide a powerful tool for manipulating ultracold atoms (Bloch et al., 2012; Grimm et al., 2000). However, diffraction sets a fundamental limit for the length-scale of such manipulations, given by the wavelength of light (Hecht, 1998). In particular, the large period of optical lattices determines the energy scale of the associated many-body atomic states (Buluta and Nori, 2009; Yi et al., 2008; Leung et al., 2012; Lewenstein et al., 2012). The resulting scaling can be best understood by noting that in the first Bloch band the maximum atomic momentum $\sim 1/\ell$, where ℓ is the lattice spacing. This sets the maximum kinetic energy to $h^2/m\ell^2$ (Jaksch et al., 1998). For conventional optical lattices the lattice spacing is set by half the wavelength of the trapping light ~ 500 nm; this yields corresponding tunneling rates of up to a few tens of kHz. Additionally, for atoms in their electronic ground states interactions are restricted to short range.

Recent experimental (Stehle et al., 2011) and theoretical (Murphy and Hau, 2009; Chang et al., 2009) work has demonstrated that integrating plasmonic systems with cold atoms represents a promising approach to achieving subwavelength control of atoms. In particular, the experiments of Ref. (Stehle et al., 2011) showed that ultracold atoms can be used to probe the near fields of plasmonic structures, paving the way to eventually trap atoms above such structures. In this chapter we propose and analyze a novel approach to the realization of high-density optical lattices using the optical potential formed from the near field scattering of light by an array of plasmonic nanoparticles. By bringing atom trapping into the subwavelength and nanoscale regime we show that the intrinsic scales of tunneling and onsite interaction for the Hubbard model can be increased by several orders of magnitude compared to conventional optical lattices. In addition, subwavelength confinement of the atoms results in strong radiative interactions with the plasmonic modes of the nanoparticles (de Leon et al., 2012). The coupled atom-plasmon system can be considered as a scalable cavity array that results in strong, long range spin-spin interactions between the atoms with both dissipative and coherent contributions (Cirac et al., 1997; Kimble, 2008). Such a system can be used for entanglement of remote atoms as well as for novel realizations of coherent and dissipative many-body systems.

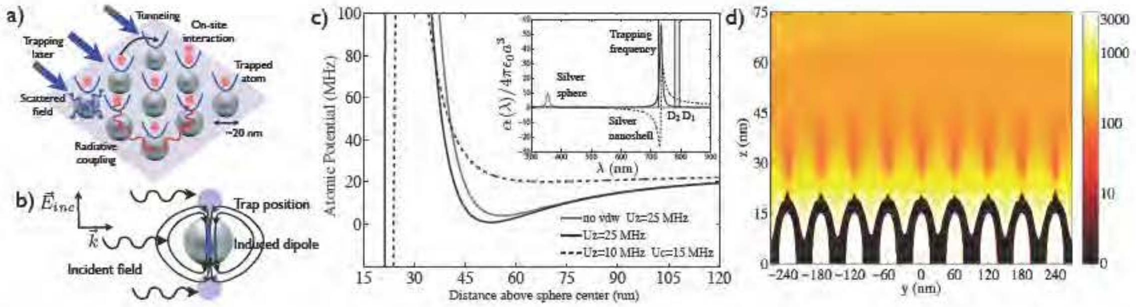

Figure 3.1: a) Illustration of the relevant physics in the plasmonic lattice. b) Illustration of how to engineer a blue-detuned optical dipole trap by driving on the blue side of the plasmon resonance. c) Atomic potential for Rb including van der Waals (vdw) for trapping above a single silver nanoshell. Dotted line shows how to weaken the trap by applying circularly polarized light perpendicular to the trapping light. (Inset) Real (dashed) and imaginary (solid) part of the dipole polarizability for a sphere and the nanoshell with a 15 nm radius and 13.85 nm SiO_2 core. d) y-z contours of atomic potential in MHz for a line of nine spheres in the center of a 45x45 square lattice with a 60 nm lattice spacing, black regions are where the potential is negative due to vdw, spheres are shown in white. The nanoshells are silver with a 15 nm radius and 13.65 nm SiO_2 core, the trapping light is red detuned (704 nm) wrt to the plasmon resonance (682 nm) and applied from above with rotating x-y polarized light.

3.2 Atom Trapping Above a Single Metallic Nanoparticle

To illustrate our approach we first consider a single metallic nanosphere in vacuum illuminated by a plane wave. For spheres small compared to a wavelength the dominant contribution to the scattered field is the dipole term, where the induced dipole moment is given by $\boldsymbol{p} = \alpha(\omega)\boldsymbol{E}_0$ with

$$\alpha(\omega) = 4\pi\epsilon_0 a^3 \frac{\varepsilon(\omega) - 1}{\varepsilon(\omega) + 2} \tag{3.1}$$

where a is the radius of the sphere and ε is the permitivity (Jackson, 1999). The total electric field is

$$\boldsymbol{E} = \boldsymbol{E}_0 + \frac{\alpha(\omega)}{4\pi\epsilon_0} \frac{3(\hat{r}\cdot\boldsymbol{E}_0)\hat{r} - \boldsymbol{E}_0}{r^3} \tag{3.2}$$

Near $\varepsilon(\omega_{sp}) = -2$ there is a plasmon resonance and the scattered field can be engineered to create an optical dipole trap as depicted in Fig. 3.1b. Specifically, when the applied field is linearly polarized on the blue side of the plasmon resonance then the induced dipole will be $\sim \pi$ out phase with the incident field, leading to two intensity minima along the polarization direction at the positions $z_T^3 = \pm 2a^3\omega_{sp}^2/(\omega^2 - \omega_{sp}^2)$, where we took a Lorentzian polarizability near the resonance $\alpha(\omega) = 4\pi\epsilon_0 a^3\omega_{sp}^2/(\omega_{sp}^2 - \omega^2 - i\omega\kappa)$, with κ the linewidth. For red detuned, circularly polarized light, there will be two minima along the propagation axis. An atom can be trapped in these intensity minima via optical dipole forces (Grimm et al., 2000). The trapping potential is given by $\hbar\Omega^2/\delta$, where $\Omega = \boldsymbol{\mu}_0 \cdot \boldsymbol{E}/\hbar$ is the Rabi frequency, $\boldsymbol{\mu}_0$ is the atomic dipole moment, and $\delta = \omega_a - \omega$ is the detuning between the atom and laser. Expanding near the trap minima gives the trapping frequency $\omega_T^2 = 9\frac{\hbar\Omega_0^2}{\delta\, m\, z_T^2}\mathrm{Re}(\alpha)^2/\left|\alpha\right|^2 \sim \hbar\,\Omega_0^2/\delta\, m\, a^2$.

The trap depth can be controlled by applying a second field with the opposite polarization, as illustrated in Fig. 3.1c. Using this method, the atoms can be loaded into the near field traps by starting with a cold, dense gas of atoms in a large trap and then adiabatically turning on the near field traps.

We now address several practical considerations. First, for alkali atoms there is a large disparity between the natural plasmon resonance and the atomic trapping transitions. For a solid silver sphere the plasmon resonance occurs near 350 nm (Johnson and Christy, 1972), compared to 780 nm for the D2 line in Rb. However, the plasmon resonance is easily tuned by changing the geometry. Adding an inert core, such as SiO_2, will shift the plasmon resonance into the red (Bohren and Huffman, 1983), as illustrated in the inset to Fig. 3.1c.

There will also be significant surface interactions. In Appendix B.1 we calculate the Van der Waals (vdw) interaction between a single metal sphere and an atom. These vdw forces can be overcome with relatively modest laser power because of the sphere's plasmonic enhancement (Murphy and Hau, 2009; Chang et al., 2009). There are two dominant sources of heating and decoherence arising from incoherent transitions induced by the trapping laser or thermal magnetic field noise in the nanoparticle. The first effect scales as $\gamma\,\Omega^2/\delta^2$, where γ is the atomic linewidth, and is suppressed at large detuning. To estimate the effect of magnetic field noise we approximate the nanoshell as a current loop of radius and height a, thickness

t, and resistivity ρ. Then the incoherent transition rate between hyperfine states is $\sim (g_F \mu_0 \mu_B)^2 k_B T (a^4 t / r^5)/\hbar^2 \rho\, r$, where r is the distance of the atom to the sphere center, g_F is the hyperfine g-factor, μ_B is the Bohr magneton, and T is the temperature (Henkel et al., 1999).

3.3 Atom Trapping Above a Lattice of Nanoparticles

Figures 3.1cd show the atomic trapping potential for a single sphere and an array, respectively. We numerically obtained the trapping potential in Fig. 3.1c using Mie theory and the vdw potential was obtained using the methods in Ref. (Reid et al., 2009). To solve for the trapping potential in the array in Fig. 3.1d we approximated the scattered field from each nanoshell by a dipole and solved for the total field self-consistently. Using the parameters in Fig. 3.1c for trapping ^{87}Rb above a silver nanoshell at room temperature with $\Omega_0 = 25$ GHz (corresponding to $\sim 10^8 I_{\text{sat}}$, where $I_{\text{sat}} \approx 1.7$ mW/cm^2) and $\delta = 25$ THz, we estimate a trap depth of ~ 25 MHz and a trapping frequency of ~ 5 MHz. Both the magnetic field noise and laser detuning limit the decoherence rate to ~ 10 Hz and the heating rate to ~ 1 Hz, meaning that the atom can be trapped for ~ 1 second.

The controlled patterning of arrays of metallic nanoparticles can be done lithographically in a top-down approach or through the controlled self-assembly of metallic nanoparticles in a bottom-up approach (Nagpal et al., 2009; Lindquist et al., 2012; Fan et al., 2010; Grzelczak et al., 2010). In any nanofabricated system one must contend with disorder; the relevant disorder in this system occurs in the particle positioning and particle formation. In lithographic approaches one can control the particle formation at the level of 1-2 nm (Lindquist et al., 2012). In bottom-up, self-assembly approaches it is possible to create large regions of well ordered crystal with a finite density of point and line defects, much like a conventional solid (Grzelczak et al., 2010). Due to the local nature of the traps the disorder in the particle positioning will not affect the trapping. Errors in the particle formation can influence the trap by shifting the plasmon resonance and the field enhancement of each particle. To achieve consistent traps the fractional error in the plasmon resonance should be smaller than its inverse quality factor $Q = \omega_{sp}/\kappa$, which for silver(gold) nanospheres goes up to 80(20) (Johnson and Christy, 1972; Hartland, 2011). Currently, metallic nanoshells can be made with a fractional error in the radius of less than 5%, which is comparable to the inverse of Q (Rycenga et al., 2011).

3.4 Hubbard Models in Nanoscale Lattices

As a first example application of this system we consider a realization of the single-band Hubbard model in the novel regime of large atomic density (Bloch et al., 2012). As an example, Fig. 3.1d shows that a well defined lattice potential can be achieved with a period of 60 nm, which is within current fabrication limits. Figure 3.2a illustrates the scaling for the maximum tunneling in the lowest band and the corresponding on-site interaction U_0. (Jaksch et al., 1998). In Appendix B.3 we show that the tunneling rate can also be tuned through appropriate polarization control.

These nanoscale traps reach a regime of atomic confinement where the ground state uncertainty becomes comparable to the free space scattering length. For two atoms in a 3D isotropic trap the two-body scattering problem can be solved exactly, leading to an effective scattering length $a_{\text{eff}}(\omega_T)$ which depends on the confinement energy (Busch et al., 1998; Bolda et al., 2002). The inset of Figure 3.2 shows that a resonance emerges in the effective scattering length as a function of trap frequency. We show how this is calculated in Appendix B.4.

Disorder in the lattice will also effect the Hubbard model. The dominant effect arises from shifts in the local atomic potential at each sphere as the plasmonic enhancement factor changes from site to site. From Eq. 2 one can show that the rms of the disorder potential is given by $U_{dis} \approx \frac{\Omega^2}{2\delta}(z_T^9/a^9Q^2)\eta/\omega_{sp}$, where η is the rms error in the plasmon resonance. If we take $\eta/\omega_{sp} \sim 5\%$, then for a wide range of parameters, including those in Fig. 3.1d, we find that U_{dis} can be made smaller than, or comparable to, the maximum tunneling. In addition, since the disorder is static one can reduce it using the techniques described in Ref. (Pichler et al., 2012). The effect of disorder on the single-particle physics is well understood (Lagendijk et al., 2009); moreover, the interplay between interactions and disorder in the Hubbard model, as studied in Ref. (Belitz and Kirkpatrick, 1994; Basko et al., 2006; Byczuk et al., 2005; Fallani et al., 2007), is an interesting new regime which can be explored in the present system.

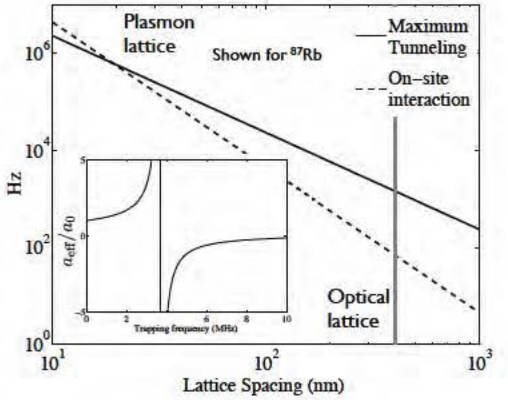

Figure 3.2: Shows the scaling of the maximum tunneling in the lowest band, and the corresponding on-site interaction. Calculated using the Wannier functions for a sinusoidal potential. (Inset) Energy dependent scattering length for two ^{87}Rb atoms on a single site as a function of the trap frequency.

3.5 Plasmon Mediated Interactions and Entanglement in the Nanolattice

We now consider long range interactions within the plasmonic lattice, associated with the strong radiative coupling between the atoms and spheres (Genov et al., 2011). This can be viewed as a strongly coupled cavity QED system. The coupling between the atoms and the near field of the sphere is given by $g \sim \mu_0 d_0/\epsilon_0 r^3$ where $d_0 = \sqrt{\hbar\omega_{sp}\alpha(0)/2}$ is the quantized dipole moment of the sphere (de Vries et al., 1998). Since the plasmons are overdamped the relevant coupling is given by the Purcell factor $P = g^2/\kappa\gamma$. The plasmon linewidth κ has contributions from radiative and ohmic losses. The radiative damping rate is $k^3 d_0^2/3\pi\epsilon_0\hbar \sim k^3 a^3 \omega_{sp}$. Large spheres are radiatively broadened and, in this case, $P \sim (kr)^{-6}$, while for small spheres $P \sim Qa^3/k^3r^6$. In both limits, when $r \ll \lambda/2\pi \sim 100$ nm the atoms enter the

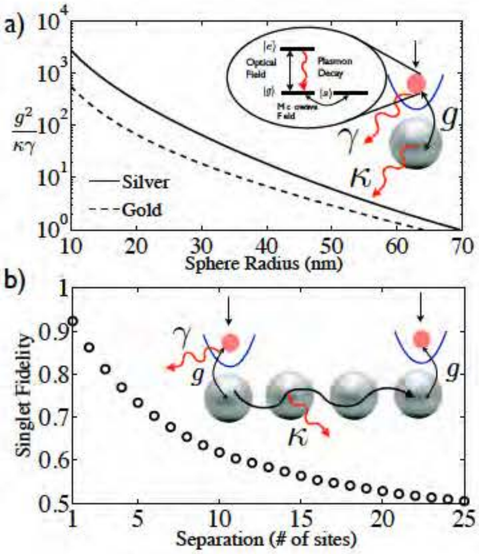

Figure 3.3: a) Shows the cavity QED figure of merit $g^2/\kappa\gamma$ with changing system size assuming the atom is trapped at a distance of twice the sphere radius. We show the scaling for both silver and gold nanoshells with a Q of 80 and 20, respectively. (Inset) Single atom trapped above a nanosphere acts as cavity QED system with atomic and cavity losses γ and κ, respectively, and a coherent coupling g. b) Fidelity for generating a ground state singlet state between two atoms on the lattice with their separation after optimization. The entanglement is generated through interaction with the collective plasmon modes, where we took the metal losses of bulk silver. (Inset) Scalable cavity QED array of atoms and plasmons.

strong coupling regime $P \gg 1$, see Figure 3.3a. Note that there are also multipolar corrections to the Purcell factor, but in Appendix B.1-2 we show these scale as $\mathrm{Im}((\epsilon-1)/(\epsilon+1))a^5/r^5 \sim 10^{-4}$ for silver.

For a lattice of nanospheres, intersphere coupling is also present and leads to delocalized plasmon modes in the lattice (Quinten et al., 1998; Krenn et al., 1999). We calculate the interaction of two atoms through these modes in a 1D chain of nanospheres. For each sphere in the chain we can write the self-consistent equation for their dipole moments as (Park and Stroud, 2004)

$$\boldsymbol{p}_n = \alpha(\omega)\big(\boldsymbol{E}_n + \boldsymbol{N}_{nm}\boldsymbol{p}_m\big) \tag{3.3}$$

where $\boldsymbol{p}_n$ is the induced dipole moment of the nth nanopoarticle, $\boldsymbol{E}_n$ is the incident field, and $\boldsymbol{N}_{nm}$ is the 3x3 matrix that gives the dipole field at site n due to the dipole at site m. In 1D two sets of transverse modes where the dipoles are oriented perpendicular to the chain and one set of longitudinal modes for parallel orientation. Defining $\tilde{\boldsymbol{p}}_q$ to be the qth eigenvector of $\boldsymbol{N}_{nm}$ with eigenvalue D_q, then the effective polarizability of the qth mode is $\alpha_q^{-1} = \alpha^{-1} - D_q$, i.e. $\tilde{\boldsymbol{p}}_q = \alpha_q \tilde{\boldsymbol{E}}_q$. For a Lorentzian polarizability the real part of D_q gives the shift in the resonance frequency of the qth mode and the imaginary part gives the change in the linewidth. N_{nm} is diagonalized by Fourier transform and if we neglect all but nearest neighbor terms $D_q = 2N_{01}^r \cos q - ik^3/6\pi\epsilon_0$, where $N_{01}^r = \mathrm{Re}(N_{01})$.

Let us consider atoms trapped above the 1D array of spheres. The plasmonic modes can be adiabatically eliminated using standard methods in quantum optics (Gross and Haroche, 1982). For two-level atoms polarized parallel to the 1D chain the atomic density matrix evolution is

$$\begin{aligned}\dot{\rho} &= -\frac{i\omega_{at}}{2}\sum_n [\sigma^z_n, \rho] - \frac{i}{2}\sum_{nm} \delta\omega_{nm}\left[\sigma^+_n\sigma^-_m, \rho\right] \\ &\quad - \frac{1}{2}\sum_{n,m} \gamma_{nm}\big(\{\sigma^+_n\sigma^-_m, \rho\} - 2\sigma^-_m\,\rho\,\sigma^+_n\big) \qquad (3.4) \\ \delta\omega_{nm} &= -\frac{3\,\ell^3}{8k^3z^6}\Gamma_0\,\mathrm{Re}\left(\frac{i\,e^{iq^*_r|n-m|}}{\sin q^*}\right)e^{-q^*_i|n-m|} \qquad (3.5) \\ \gamma_{nm} &= \frac{3\,\ell^3}{8k^3z^6}\Gamma_0\,\mathrm{Im}\left(\frac{i\,e^{iq^*_r|n-m|}}{\sin q^*}\right)e^{-q^*_i|n-m|} \qquad (3.6)\end{aligned}$$

where z is the position of the atoms above the sphere and $q^* = q^*_r + i\,q^*_i$ is the resonant wavevector such that $\alpha^{-1}_{q^*}(\omega_a) = 0$. The first line in Eq. 3.4 describes the coherent evolution and the second line describes the collective dissipation. Here we have neglected the contribution to the interaction from free-space radiative modes.

The coherent and dissipative contributions to Eq. 3.4 are equally strong when the atom and plasmon are near resonant. Working far off resonance, however, results in purely coherent dynamics, which can be used to implement long-range interacting spin models including frustration (Strack and Sachdev, 2011; Gopalakrishnan et al., 2009; Gardner et al., 2010). Alternatively, the collective dissipative dynamics can be used to prepare correlated atomic states (Verstraete et al., 2009). As an example, we now show how to directly prepare a ground state singlet between two atoms separated by large distances on the lattice. We take two ground states $|g\rangle$ and $|s\rangle$ and an excited state $|e\rangle$ which is coupled to $|g\rangle$ via an external field and only decays via the plasmons back to $|g\rangle$ (see inset to Fig. 3.3a). An external microwave field mixes the two ground states. To prepare the singlet state $|S\rangle = |gs\rangle - |sg\rangle$ we use a similar approach to

Ref. (Kastoryano et al., 2011) whereby the singlet state is engineered to be the steady state of a driven, dissipative evolution. We take a separation n such that $\cos q_r^* n = 1$ and

$$\dot{\rho} = -\gamma_{0n}\mathcal{D}[\sigma_1^{ge} + \sigma_2^{ge}]\rho - \delta\gamma_n(\mathcal{D}[\sigma_1^{ge}] + \mathcal{D}[\sigma_2^{ge}])\rho \tag{3.7}$$

where $\mathcal{D}[c]\rho = 1/2\{c^\dagger c, \rho\} - c\rho c^\dagger$ and $\delta\gamma_n = \gamma_{00} - \gamma_{n0} \sim \gamma_{00}\,(\ell^3/a^3)n/Q$ for $n \ll Q$. The dynamics can be mapped to a cavity QED system by identifying γ_{0n} with the collective decay g^2/κ and $\delta\gamma_n$ with the free space decay γ. The two excited states $|eg\rangle$ and $|ge\rangle$ split into a superradiant state $|eg\rangle + |ge\rangle$ and a subradiant state $|eg\rangle - |ge\rangle$ with decay rates $2\gamma_{0n} + \delta\gamma_n$ and $\delta\gamma_n$, respectively.

The singlet preparation proceeds as follows. First, we selectively excite the subradiant transition $|gg\rangle$ to $|ge\rangle - |eg\rangle$ by driving with a weak external laser field $\Omega \sim \delta\gamma_n \ll \gamma_{00}$, which we take to have a π phase difference on the two atoms. Second, in order to make the singlet state a unique steady state, we apply a global microwave field to mix the triplet ground states without affecting the singlet state. In the resulting dynamics, the pumping rate into the singlet state is $\Omega^2/\delta\gamma_n$, while the pumping rate back into the triplets is Ω^2/γ_{00} (see Appendix B.5 for more details). The steady state of this process gives the singlet state with fidelity $F = \langle S|\,\rho\,|S\rangle \sim 1 - 1/P'$ where $P' = \gamma_{00}/\delta\gamma_n$. Fig. 3.3b shows the fidelity for two atoms with variable separation obtained from numerical simulation of Eq. 3.4.

To measure the correlations in this system, an all optical approach could be realized by making the nanoparticle array in the near field of a solid immersion lens (SIL), which enhances the resolution beyond the diffraction limit by a factor of n, the index of refraction of the SIL (Wu et al., 1999). Combining a SIL with e.g. super resolution microscopy techniques would allow one to reach the requisite resolution of $\sim$50 nm at optical wavelengths (Huang et al., 2009).

3.6 Conclusions

Our analysis shows that combining cold atom techniques with nanoscale plasmonics reaches new regimes in controlling both the collective motion of atoms and atom-photon interactions. Combining excellent quantum control of isolated atoms with nanoscale localization, may open up exciting new possibilities for quantum control of ultracold atoms.

Chapter 4

Single Photon Nonlinear Optics with Graphene Plasmons

4.1 Introduction

Nonlinear optical processes find ubiquitous use in modern scientific and technological applications, facilitating diverse phenomena like optical modulation and switching, spectroscopy, and frequency conversion (Boyd, 2003). A long-standing goal has been to realize nonlinear effects at progressively lower powers, which is difficult given the small nonlinear coefficients of bulk optical materials. The ultimate limit is that of single-photon nonlinear optics, where individual photons strongly interact with each other. Realization of such nonlinear processes would not only facilitate peak performance of classical nonlinear devices, but also create a unique resource for implementation of quantum networks (Kimble, 2008) and other applications that rely on the generation and manipulation of non-classical light.

One approach to reach the quantum regime involves coupling light to individual quantum emitters (Duan and Monroe, 2008; Kimble, 2008), in order to take advantage of their intrinsically nonlinear electronic spectrum. While a number of remarkable phenomena have been demonstrated using these systems (Haroche, 2013), their realization remains a challenging task. Specifically, in contrast to conventional bulk nonlinear systems, coherent single quantum emitters are generally unable to operate under ambient conditions, suffer from relatively slow operating speeds, and have limited tunability of their properties.

Motivated by these considerations, recently there has been renewed interest in bulk nonlinear systems that can reach the quantum regime (Matsuda et al., 2009; Mabuchi, 2011; Ferretti and Gerace, 2012). In particular, recent experiments demonstrated realization of a quantum nonlinear medium, featuring single photon blockade (Peyronel et al., 2012) and conditional nonlinear two-photon phase shifts (Peyronel et al., 2013), based on strongly interacting ultracold atoms. The essence of this approach is that the probability for two photons to interact can become substantial if the photons are confined to a sufficiently small mode volume of the nonlinear medium for sufficiently long times. Motivated by these recent developments, in this Letter we explore the potential for using nanoscale surface plasmon excitations in graphene (Mikhailov and Ziegler, 2007; Jablan et al., 2009) for quantum nonlinear optics. In particular, recent theoretical (Mikhailov and Ziegler, 2007; Jablan et al., 2009; Koppens et al., 2011) and experimental (Fei et al., 2012; Chen et al., 2012) results indicate that graphene plasmons can be confined to volumes millions of times smaller than the diffraction limit. We show that under realistic conditions, this field confinement enables deterministic interaction between two plasmons (*i.e.*, photons) over picosecond time scales, which is much shorter than the anticipated plasmon lifetime (Principi et al., 2013). We show how one can take advantage of this interaction to realize a single photon switch and produce non-classical light.

4.2 Graphene Plasmonics

Graphene, a single atomic layer of carbon atoms, has attracted tremendous interest for its unique electronic, mechanical, and quantum transport properties (Geim and Novoselov, 2007; Castro Neto et al., 2009). More recently, its optical response has also been explored. For example, it has been demonstrated that the graphene band structure yields a constant attenuation rate of light through a single layer of $\pi\alpha \approx 2.3\%$ when the graphene is in its intrinsic (undoped) state, where $\alpha \approx 1/137$ is the fine-structure constant (Nair et al., 2008). The band structure also produces remarkable properties for guided electromagnetic surface waves in the form of surface plasmons (SPs) (Wunsch et al., 2006), as we now describe.

Through electrostatic gating, it is possible to introduce a net carrier concentration, which shifts the Fermi energy $\hbar\omega_F$ away from the Dirac point to a non-zero value. The in-plane conductivity of graphene is well-approximated by the expression $\sigma(\omega) \approx \frac{ie^2}{\pi\hbar}\frac{\omega_F}{\omega+i\gamma}$ at frequencies below twice the Fermi frequency $\omega < 2\omega_F$ (Falkovsky, 2008), which describes a Drude-like response of electrons within a single band. In realistic systems the conductivity will also have a small term γ describing dissipation due impurity or phonon-mediated scattering. There are two limits on the existence of low-loss SP modes in graphene. First, at frequencies $\omega > 2\omega_F$, graphene suffers from strong inter-band absorption (*e.g.*, giving rise to its attenuation of 2.3%) (Jablan et al., 2009; Koppens et al., 2011). Second for frequencies above the the optical phonon frequency $\hbar\omega_{op} \approx 0.2$ eV, there is additional loss due to scattering into optical phonons (Jablan et al., 2009; Yan et al., 2013). With this in mind, we focus on the regime where the frequencies fall below $2\omega_F$ and ω_{op}. In this regime, we can approximate $\gamma = ev_F^2/\mu\,\hbar\omega_F$ where μ is the mobility. The ability to tune ω_F, and consequently the optical properties, through electrostatic gating makes graphene unique compared to normal metals.

Like in noble-metal plasmonics (Maier, 2007), the free nature of charge carriers described by the Drude response gives rise to SP modes in graphene (Mikhailov and Ziegler, 2007; Jablan et al., 2009), which are combined excitations of charge-density and electromagnetic waves bound to the surface. At first order in k_{sp}/k_F the SP dispersion is given by

$$\omega_{sp}^2 = \frac{e^2\omega_F}{2\pi\epsilon_0\varepsilon\hbar}k_{sp} \approx 2\omega_F\, v_F\, k_{sp} \tag{4.1}$$

where $\varepsilon \approx 2.4$ is the effective dielectric constant and $v_F \approx 10^6$ m/s is the Fermi velocity (Wunsch et al., 2006). This dispersion relation implies a remarkable reduction of the SP wavelength compared to the free space wavelength $\lambda_0 = 2\pi c/\omega_{sp}$, as $\lambda_{sp}/\lambda_0 \sim v_F/c \sim 3\cdot 10^{-3}$. Thus, the smallest possible mode volume of a graphene SP resonator, $V \sim \lambda_{sp}^3$, can be $\sim 10^6$ times smaller than in free space (Koppens et al., 2011).

4.3 Nonlinear Plasmonics in Graphene

Because the plasmons are intra-band excitations of electrons near the Fermi surface, the nonlinear conductivity can be calculated from the semiclassical Maxwell-Boltzmann equations, as detailed in Appendix C.1. In summary, the distribution function $f(\boldsymbol{x},\boldsymbol{k},t)$ for an electron at in-plane position $\boldsymbol{x}$ and with Bloch momentum $\boldsymbol{k}$ evolves under the Maxwell-Boltzmann equation as

$$\partial_t f + v_F \hat{k} \cdot \partial_{\boldsymbol{x}} f + e \partial_{\boldsymbol{x}} \varphi \cdot \partial_{\boldsymbol{k}} f = 0, \tag{4.2}$$

where the electostatic potential $\phi(\boldsymbol{x}, z, t)$ satisfies Poisson's equation $\nabla^2 \phi = en\delta(z)/\epsilon_0 \epsilon$. Here z is the out-of-plane coordinate and $n = \int d\boldsymbol{k}\, f$ is the 2D electron density. For weak excitations of the electron distribution, the term $\partial_{\boldsymbol{k}} f$ in the Maxwell-Boltzmann equation can be replaced by the equilibrium value $\partial_{\boldsymbol{k}} f^{(0)}$, yielding a linear equation supporting SPs with the dispersion given in Eq. (4.1) and an electrostatic wave given by $E = -\nabla\phi \propto \delta n \sin(kx - \omega t)$.

For sufficiently large density perturbations δn, the nonlinear interaction between the non-equilibrium distribution $\partial_{\boldsymbol{k}} f$ and potential must be accounted for. This effect can be interpreted as a backaction induced by the electrostatic wave on the electrons via a ponderomotive force $F_p \sim \partial_x E^2 \sim k\delta n^2 \sin 2kx$, which grows with the amplitude of the SPs. This nonlinear force directly excites a second plasmon wave at wavevector $2k$ and frequency 2ω, i.e. second harmonic generation, and gives rise to the second order conductivity calculated by Mikhailov (2011). We show (see Appendix C.1) that this leads to a nonlinear shift at the original wavevector k and frequency ω, with an effective third order conductivity for the SPs given by

$$\sigma^{(3)}(k_{sp},\omega) = -i\frac{3\pi}{4}\frac{v_F^4}{\omega_F^3}\frac{\epsilon_0^2\varepsilon^2}{\hbar\omega}. \tag{4.3}$$

This result differs from the nonlinear conductivity as seen by free-space light normally incident on a graphene sheet, where one finds that $\sigma^{(3)} \sim 1/\omega^3$ (Mikhailov and Ziegler, 2008). Remarkably, as we discuss next, the tight confinement of SPs in graphene implies that the fields associated with even single quantized SPs are strong enough that nonlinear effects are observable.

4.4 Graphene Macro-Atom

Anticipating the large strength of nonlinear interactions at the level of single SPs in nanoscale graphene resonators, we are motivated to introduce a quantum description of such a system. We write the Hamiltonian as $H = H_0 + H_c$, where H_0 characterizes solely the excitation spectrum of the graphene resonator, and H_c describes an external coupling to the resonator (such as in Fig. 4.3a), which allows one to probe the resonator properties or utilize the nonlinearities for applications such as a single-photon transistor.

We first consider the intrinsic properties of the resonator given by H_0. Considering the fundamental SP mode of the resonator with corresponding annihilation operator a_q and number operator $n_q = a_q^\dagger a_q$, the effective Hamiltonian H_0 is given by (Denardo

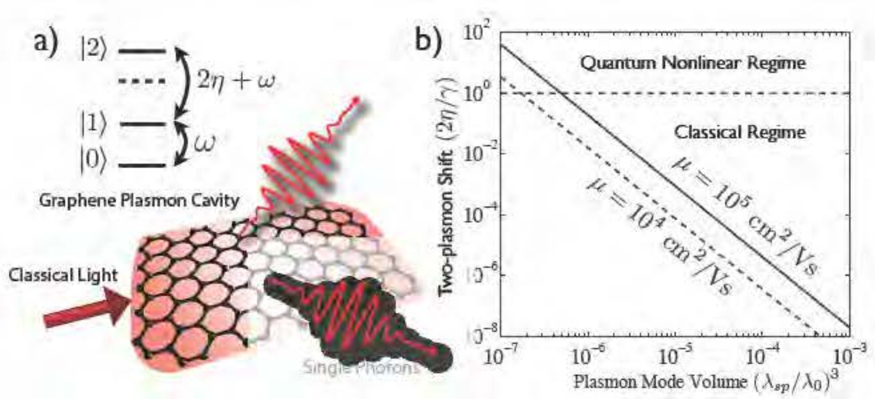

Figure 4.1: a) Schematic of the graphene macro-atom. A doped graphene disk confines photons as plasmons to mode volumes millions of times smaller than free space. This induces a large dispersive nonlinearity so that only a single photon can resonantly excite the cavity. b) Shows the nonlinear shift from Eq. 4.5 for the fundamental mode relative to the plasmon linewidth with decreasing mode volume $V_0 = (\lambda_{sp}/\lambda_0)^3$. Here we took the linewidth as $\gamma = ev_F^2/\mu\,\hbar\omega_F$ with the Fermi energy $\hbar\omega_F = 0.2$ eV and a mobilities of $\mu = 10^5(10^4)$ cm^2/Vs corresponding to quality factors of roughly 600(60).

and Putterman, 1988; Gervasoni and Arista, 2003)

$$H_0 = \left(\omega_q - i\kappa/2 + \eta_q(n_q - 1)\right) n_q. \tag{4.4}$$

See Appendix C.2 for a detailed derivation. This Hamiltonian describes the quantum analog of a cavity exhibiting an intensity-dependent refractive index, where the effective resonant frequency $\omega_q + \eta_q(n_q - 1)$ shifts depending on the intra-cavity photon number. Here we have also included the total cavity linewidth $\kappa = \kappa_{ex} + \gamma$ into the cavity description which includes both the intrinsic losses due to impurity and phonon scattering, given by γ and radiative losses of the cavity into other optical or plasmonic modes, given by κ_{ex}. For graphene, the nonlinear interaction strength is given by

$$\eta_q = \frac{7\,\pi\,\omega_q}{64\,A\;k_F^2}\sqrt{\frac{\varepsilon\,q^3}{2\alpha_g k_F^3}}, \tag{4.5}$$

where $\alpha_g \equiv e^2/4\pi\epsilon_0\,\hbar\,v_F \approx 2$ and A is the mode area of the resonator, which can be given by $A = \lambda_{sp}^2/4$ for a diffraction-limited structure. The $\eta_q \propto A^{-1}$ scaling reflects that the field intensity of a single SP grows inversely like its confinement.

At the quantum level, the interaction parameter $2\eta_q$ indicates the additional energy cost to excite two versus one photon in the cavity, as can be seen in the cavity excitation spectrum (inset of Fig. 4.2a). When $2\eta \gg \kappa$, the graphene sheet behaves as a two-level atom because it can only resonantly absorb a single photon as illustrated in Fig. 4.1a; thus we describe this as the quantum nonlinear regime. The ratio $2\eta_q/\kappa$ is then a good measure of the quality of the cavity as a quantum emitter. Fig. 4.1b shows $2\eta_q/\gamma$ for the fundamental mode with decreasing mode volume (assuming mobilities of 10^5 and 10^4 cm^2/Vs), where we see that this ratio can be as large as 100. The parameter $\eta/\kappa \propto Q/A$, where Q is the quality factor of the resonator. Intuitively then, the nonlinear cavity can exhibit quantum effects if two photons interact within a small enough volume and for long enough time.

The enabling mechanism for a two-level atom to be useful for quantum information processing is that it can only emit single photons at a time. This can be characterized by the second order correlation function of the emitted light, which is identical to that of the cavity mode, $g^{(2)}(t) = \langle a^\dagger(\tau)a^\dagger(t+\tau)a(t+\tau))a(\tau)\rangle/\langle a^\dagger(\tau)a(\tau)\rangle$. For a stationary process, $g^{(2)}(0) < 1$ indicates non-classical “anti-bunching” and approaches $g^{(2)}(0) = 0$ in the limit of an ideal two-level emitter. We consider the case where the resonator is driven by an external laser from the side and emission is collected from

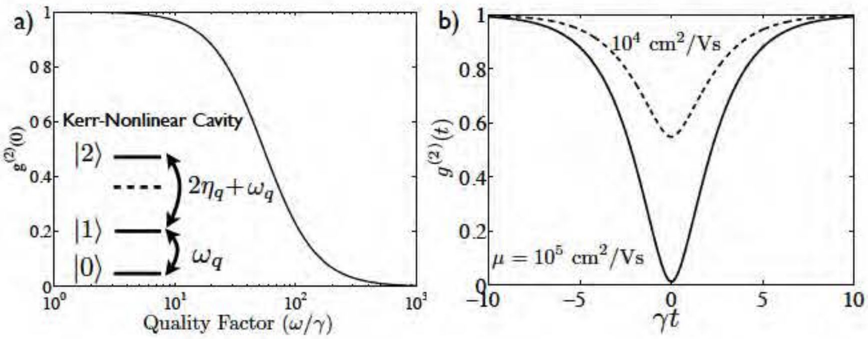

Figure 4.2: a) Shows $g^{(2)}(0)$ for the graphene macro-atom driven by a weak coherent state. As the plasmon lifetime increases $g^{(2)}(0)$ becomes much less than one, indicating its transition to an effective two-level system (illustrated in *inset*). b) Shows $g^{(2)}(t)$ for $\hbar\omega_{sp} = 0.2$ eV and two different mobilities.

a different direction. In the limit of weak driving we find that

$$g^{(2)}(0) = \frac{\kappa^2}{4\eta^2 + \kappa^2}, \tag{4.6}$$

thus establishing $\eta \lesssim \kappa$ as the regime where quantum properties become observable. In Fig. 4.2ab we take $\kappa_{ex} = 0$ and we see that, for the largest nonlinearities, $g^{(2)} < 1$ can be readily observed, even in the presence of significant loss.

4.5 Efficient Coupling and a Single-photon Switch

In order to exploit the large nonlinearity of graphene, we need an efficient method to convert SPs into external optical modes on time scales short compared to the intrinsic losses. Specifically, one needs that the total linewidth $\kappa = \kappa_{ex} + \gamma$ contains a large component κ_{ex} that goes into desirable external channels compared to the intrinsic losses γ. One approach is to use the direct dipolar emission of the cavity

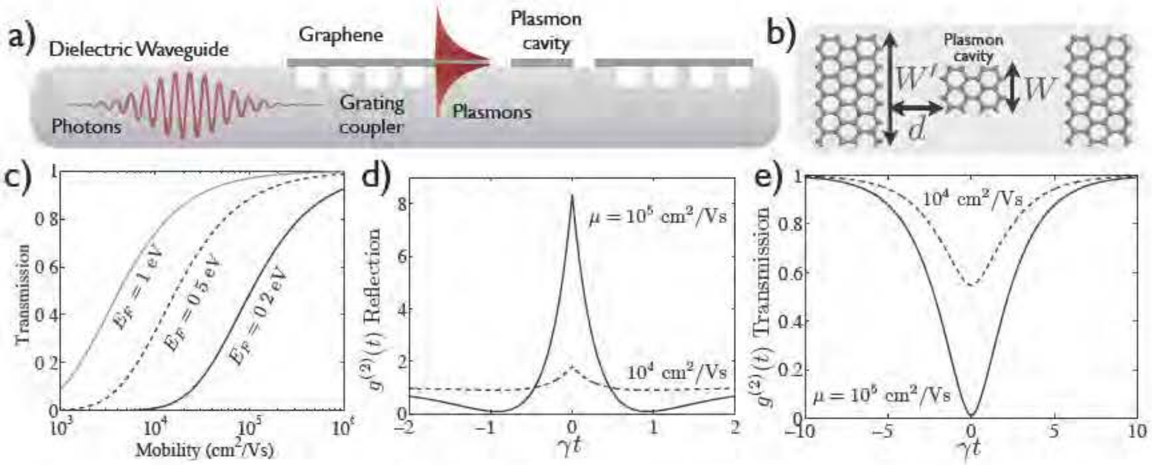

Figure 4.3: a) Integrated nonlinear optical circuit for interfacing the graphene macro-atom with photons. First the photons are converted into bulk plasmons via a grating, then they couple to the graphene macro atom, after which they are converted back into waveguide photons. b) Shows a top down view near the plasmon cavity. c) Shows the single photon transmission through the system which is less than one due to losses during the grating coupling, here we took $\xi = k_0$ and $P \gg 1$ so the only losses are in the nanoribbons. The plasmon frequency is taken to be less than the cutoff from optical phonons (0.2 eV) and we assume the decay rate γ is dominated by impurity scattering. The three curves are for a fixed plasmon frequency with increasing Fermi energy, which increases the spatial propagation length of the plasmons. d) Shows bunching in reflection for two incident photons from the left with $\hbar\omega_{sp} = 0.2$ eV, $E_F = 0.23$ eV, $P = 2$, and mobilities $\mu = 10^4(10^5)$ cm^2/V·s (dashed(solid)) corresponding to a lifetime of 0.2(2) ps and a cavity quality factor of 60(600). e) Shows antibunching in transmission for $P = 0.1$ with other parameters as in (c).

into free space radiation. For the square cavities described above, the dipole moment is given by $p = 2\, e\, k_F^2/k_{sp}^3$ which gives a decay rate into radiation of

$$\kappa_{ex} = \frac{k_0^3\, p^2}{3\pi\epsilon_0\hbar} = \frac{16\,\alpha_g}{3}\frac{k_F^3}{k_{sp}^3}V_0\,\omega_F \tag{4.7}$$

where $V_0 \equiv (\lambda_{sp}/\lambda_0)^3$. For cavities in the quantum nonlinear regime, this is a small contribution to the total losses; thus, while it may be a convenient method for probing the system a more practical approach is needed.

We envision a two-step process illustrated in Fig. 4.3ab: first a waveguide photon is converted into a bulk plasmon via a dielectric grating, then this plasmon can tunnel directly into the nonlinear cavity. We first consider the direct coupling between the cavity and the bulk plasmons. We take the cavity to be separated a distance d from a long nanoribbon of width W. For $d \gg W, \lambda_{sp}$ the coupling is dipolar and small, which allows us to calculate the decay of the fundamental cavity mode into the nanoribbon via Fermi's golden rule (see Appendix C.3)

$$\kappa_{c-r} = \frac{32}{\pi^2}\frac{k_F^r}{k_F^c}\frac{W\,\omega}{k_{sp}^* k_{sp}^4 d^6} \tag{4.8}$$

where $k_F^{r;c}$ is the Fermi wavevector in the nanoribbon (r) and cavity (c) and k_{sp}^* is the wavevector for the nanoribbon plasmon that is resonant with the cavity mode. The cavity can be efficiently controlled through the nanoribbon by operating at a distance d such that this decay is the dominant loss channel for the cavity.

Once the plasmon is in the bulk it still remains to out-couple it to the waveguide. Due to the large mismatch in wavevectors, $k_{sp}/k_0 \sim c/v_F$, the bare coupling of the plasmons to waveguide mode will be very small. A simple and convenient solution is to fabricate a dielectric grating to enable momentum conservation. For parallel propagation, the grating wavector k_g should be given by $k_g = k_{sp} - k_0$.

Here we consider the case of a single-mode dielectric slab waveguide in vacuum coupled via the grating to a graphene nanoribbon. This geometry can be analyzed via coupled mode theory and optimized as a function of the slab thickness (Snyder and Love, 1983). Taking the grating profile to be of the form $\epsilon_g(x) = \delta\epsilon \cos k_g x$ gives the power conversion for weak losses between the waveguide and plasmon mode as $\cos^2(\xi x)$ where ξ is spatial coupling between the TM mode of the waveguide and nanoribbon (see Appendix C.4)

$$\xi \approx \sqrt{\frac{W}{W'}}\, \delta\epsilon\, e^{-\gamma_\perp h} k_0 \tag{4.9}$$

here $W' > W$ is the width of the waveguide, $\gamma_\perp^2 = \beta^2 - k_0^2$ is the transverse wavevector of the slab mode, β is the longitudinal wavevector, and h is the distance between the slab and the graphene. Because the factor in ξ in front of k_0 is order unity, the plasmon conversion for a weak grating is limited to distances $\sim \lambda_0 \gg \lambda_{sp}$. As a result the spatial decay rate of the plasmons must be much larger than k_0 to achieve efficient conversion. For plasmon frequencies below the cutoff from optical phonons (~ 0.2 eV) the spatial decay rate is given by $\gamma\, k_{sp}/\omega_{sp} \approx e v_F\, \hbar\omega_{sp}/2\,\mu\, E_F^2$, which strongly decreases with the Fermi energy E_F. In Fig. 4.3c we show the transmission of a single photon through the geometry displayed in Fig. 4.3ab.

The device depicted in Fig. 4.3ab can be used as a nonlinear single-photon switch. To characterize this process, it is first necessary to understand how an input field through the waveguide is transformed upon interacting with the nonlinear resonator, which can be done through an input-output formalism. In the case of Fig. 4.3ab of a resonator equally coupled to two waveguides, the resonator evolves under the incoming fields of the left- and right-going modes under the Hamiltonian $H_c = \sqrt{\kappa_{ex}}(a_{in}^r + a_{in}^l)a^\dagger + h.c.$, while the output fields are given by $a_{out}^{r(l)} = a_{in}^{r(l)} + i\sqrt{\kappa_{ex}}a$.

This one dimensional model has been solved exactly for the case of one and two resonant photons input from a single direction in the waveguide (Liao and Law, 2010). The response is characterized by the effective Purcell factor $P = \kappa_{ex}/\gamma$, which measures the fraction of cavity emission into the waveguide, and the normalized nonlinearity $\tilde{\eta} = \eta/\kappa$. The transmission t and reflection r coefficients for a single photon incident on resonance with the cavity are given by $t = -P/(1+P)$ and $r = 1/(1+P)$. The two photon response, however, is modified by the nonlinearity. For example two photons at frequency ω_{sp} will be blocked from entering the cavity due to the nonlinearity. This leads to antibunching in the transmission and bunching in the reflection as shown in Figures 4.3de. The suppression in the transmission scales as $\tilde{\eta}^2$ similarly to Eq. 4.6, while the bunching in reflection scales as P^4 for $\tilde{\eta} \gg P \gg 1$ (Liao and Law, 2010). Fig. 4.3e shows that such a device essentially realizes a single photon transistor where one control photon can block several signal photons from propagating through the cavity for a time given by the inverse cavity lifetime. In addition, the signal photons do not have to be at the same frequency as the control photon so long as they have significant nonlinear interaction in the cavity.

4.6 Conclusions

Our analysis shows that graphene plasmonics may provide a powerful platform for the nonlinear quantum optical control of light. Combined with the scalable fabrication of graphene this could allow the creation of complex quantum networks for many applications in quantum information and quantum simulation, as well as in classical nonlinear optics (Carusotto and Ciuti, 2013). Such a system is ultimately limited either by the losses in graphene or the strength of the nonlinearity. We estimate currently achievable quality factors for the plasmon cavity range from $10 - 10^3$; however, estimates of the ultimate limit to the graphene plasmon lifetime suggest that quality factors greater than 10^4 are possible (Principi et al., 2013). To enhance the nonlinearity further hybrid structures can be envisioned if one could fabricate the structure on top of a strong nonlinear substrate.

Chapter 5

All-Optical Switch and Transistor Gated by One Photon

5.1 Introduction

In this chapter we report on the theoretical analysis of an experimental realization of an all-optical transistor where one 'gate' photon controls a 'source' light beam. Using a slowed a light pulse in an atomic ensemble contained inside an optical resonator, we demonstrate that one stored gate photon can control the resonator transmission of subsequently applied source photons. In continuous operation, signal and gate photons derived from different lasers become anti-correlated with an equal-time cross-correlation function $g^{(2)}(0) = 0.89 \pm 0.01$.

Photons are excellent carriers of quantum information, but it is difficult to induce the strong interactions between individual photons that are required for, e.g., all-optical quantum information processing. Nevertheless, advances toward such interactions have been made in cavity quantum electrodynamics (QED) systems with atoms (Birnbaum et al., 2005; Brennecke et al., 2007; Colombe et al., 2007; Kubanek et al., 2008; Tanji-Suzuki et al., 2011; Brooks et al., 2012) or artificial atoms (Michler et al., 2000; Press et al., 2007; Fushman et al., 2008; Volz et al., 2012; Bose et al., 2012), and in a cavity-free system using atomic Rydberg states (Dudin and Kuzmich, 2012; Peyronel et al., 2012) or dye molecules (Hwang et al., 2009). All-optical switching of one beam by another(Bajcsy et al., 2009) and cross-phase modulation(Lo et al., 2011) have been demonstrated at the level of a few hundred photons by means of electromagnetically induced transparency (EIT)(Fleischhauer et al., 2005). At the few-photon level, nonclassical light has been generated (Michler et al., 2000; Birnbaum et al., 2005; Press et al., 2007; Kubanek et al., 2008; Dayan et al., 2008; Fushman et al., 2008; Bose et al., 2012; Dudin and Kuzmich, 2012; Peyronel et al., 2012; Brooks et al., 2012), and optical nonlinearities of 16° in phase shift(Turchette et al., 1995) and up to ∼20% in two-photon attenuation(Fushman et al., 2008; Tanji-Suzuki et al., 2011; Volz et al., 2012) have been observed in cavity QED systems. While switching of the cavity transmission by a single atom has also been achieved (Thompson et al., 1992), the realization of an optical transistor exhibiting gain with gate signals at the few- or one-photon level (Chang et al., 2007) remains a challenge.

Here we theoretically analyze a cavity QED version (Grangier et al., 1998; Imamoglu et al., 1997) of a single-photon switch based on EIT in a four-level system (Fleischhauer et al., 2005). Combining this technique with slow light allows one to implement an all-optical transistor where one gate photon can switch multiple signal photons. The device performance is quantified by measuring interaction-induced photon-photon anticorrelations between two distinct modes driven by independent lasers.

The system (Tanji-Suzuki et al., 2011) consists of an ensemble of laser-cooled cesium atoms optically trapped inside a high-finesse optical cavity (Fig. 5.1A) operating in the strong-coupling regime (Birnbaum et al., 2005; Brennecke et al., 2007; Colombe et al., 2007; Kubanek et al., 2008; Tanji-Suzuki et al., 2011; Brooks et al., 2012) of cavity QED. Each atom has a four-state N-type level structure $|g\rangle \leftrightarrow |d\rangle \leftrightarrow |s\rangle \leftrightarrow |e\rangle$ with two stable ground states $|g\rangle$, $|s\rangle$, and two electronic excited states $|d\rangle$, $|e\rangle$ (Fig. 5.1B). For atoms prepared in state $|g\rangle$, this atomic structure mediates an effective interaction between free-space photons (photons resonant with the $|g\rangle \rightarrow |d\rangle$ transition serving as gate photons) and cavity photons (photons resonant with the $|s\rangle \rightarrow |e\rangle$ transition serving as the source)(Schmidt and Imamoğlu, 1996; Imamoglu et al., 1997; Harris and Yamamoto, 1998). These two transitions are connected via a control laser that addresses the $|d\rangle \rightarrow |s\rangle$ transition and induces transparency (EIT) for the gate photons.

Without the signal beam, the gate photons are transmitted through the ensemble, traveling in the medium as slow-light polaritons, a superposition of a photon and a collective atomic excitation to the state $|s\rangle$. In the absence of gate photons, the state $|s\rangle$ is unpopulated so resonant signal photons are transmitted through the cavity. Thus photons arriving individually in either the gate or the signal mode are transmitted through the system. However, when photons are simultaneously present in the two modes, they affect each others propagation. A signal photon inside the cavity introduces a decoherence path for the state $|s\rangle$ via coupling to the unstable excited state $|e\rangle$ and reduces the EIT transmission for the gate photon. Conversely, when a gate photon travels in the atomic medium as a slow-light polariton, the polaritons atomic component in state $|s\rangle$ reduces the cavity transmission by introducing additional cavity loss through photon scattering on the $|s\rangle \to |e\rangle$ transition. If the coupling between the cavity and a single atom in state $|s\rangle$ is sufficiently strong, a single photon in the gate or the signal mode will each block the other mode (Thompson et al., 1992).

The strength of this effective photon-photon interaction essentially depends on two parameters: the free-space resonant optical depth $\mathcal{N}$ on the gate transition that measures the collective coupling of the atomic ensemble to the gate photon, and the single-atom cavity cooperativity η that sets the interaction strength between one atom in $|s\rangle$ and one signal photon (Birnbaum et al., 2005; Kubanek et al., 2008; Tanji-Suzuki et al., 2011). The optical depth $\mathcal{N}$ sets an upper limit of $1-e^{-\mathcal{N}}$ for the atomic component $|s\rangle$ of the slow light polariton (Fleischhauer et al., 2005) (the component that can interact with the cavity mode). The reduction of the cavity transmission by a single intracavity atom in state $|s\rangle$, on the other hand, is given (Tanji-Suzuki et al., 2011) by the factor $(1+\eta)^{-2}$. For deterministic two-mode photon-photon interactions, the gate photon must be converted with reasonable efficiency into an atomic population in state $|s\rangle$ which then needs to block the cavity. Hence we require both strong collective coupling on the gate transition ($\mathcal{N} \gg 1$) and strong single-atom-cavity coupling (Imamoglu et al., 1997; Grangier et al., 1998) on the signal transition ($\eta \gg 1$).

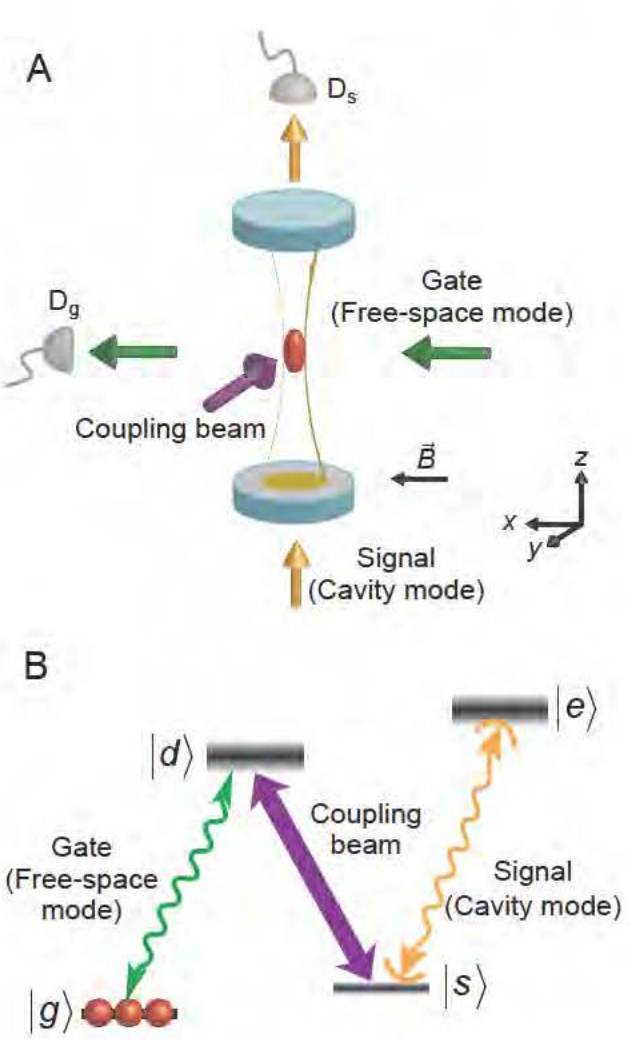
A
D_s
D_g
Gate
(Free-space mode)
Coupling beam
$\vec{B}$
z
x
y
Signal
(Cavity mode)
B
$|e\rangle$
$|d\rangle$
Coupling beam
Gate
(Free-space mode)
Signal
(Cavity mode)
$|s\rangle$
$|g\rangle$

Figure 5.1: All-optical single-photon transistor. Setup (A) and atomic level scheme (B). An ensemble of laser cooled atoms is trapped inside an optical resonator operating in the single- atom strong-coupling regime. The atoms are prepared in state $|g\rangle$ by optical pumping, and the coupling beam on the $|s\rangle \rightarrow |d\rangle$ transition induces transparency (EIT) for gate photons on the $|g\rangle \rightarrow |d\rangle$ transition. The gate photons travel slowly through the medium as quasi- particles (dark-state polaritons) with an atomic spin-excitation component in the state $|s\rangle$ that interacts with signal photons on the $|s\rangle \rightarrow |e\rangle$ transition. The interaction results in photon-photon anticorrelations that are measured with photon counters Dg and Ds. The atomic states of ^{133}Cs used in this experiment are $|g\rangle = |6S_{1/2}, F=3, m_F=3\rangle, |d\rangle = |6P_{3/2}, 4, 4\rangle, |s\rangle = |6S_{1/2}, 4, 4\rangle, |e\rangle = |6P_{3/2}, 5, 5\rangle$, where F and m_F denote the hyperfine and magnetic sublevels.

5.2 Theoretical Model

Including the decay, the effective Hamiltonian for this system can be written as

$$\begin{aligned} H_{eff}/\hbar = &\sum_k c\,|k|\,a_k^\dagger a_k + (\omega_c - i\kappa/2)b^\dagger b + i\mathcal{E}(b^\dagger - b) \\ &+ \left(\omega_{gd} - i\frac{\gamma}{2}\right)\sum_i |d\rangle_i \langle d| + \left(\omega_{se} - i\frac{\gamma}{2}\right)\sum_i |e\rangle_i \langle e| \\ &+ \sum_i \left(\Omega_c\, e^{i\omega_{ds}t}\,|s\rangle_x \langle d| + g_g\, a^\dagger(x)\ |g\rangle_x \langle d| + g_s\, b^\dagger\,|s\rangle_i \langle e| + h.c.\right) \end{aligned} \tag{5.1}$$

Here, c is the speed of light, k is the wavenumber of the gate field, ω_c is the cavity frequency and κ is the decay rate of the cavity. The electric field operators for the two fields can be written as $\hat{\mathcal{E}}_g(x) = \sqrt{\frac{\hbar c k_0}{\epsilon_0 V}}a(x)$ and $\hat{\mathcal{E}}_s = \sqrt{\frac{\hbar\omega_c}{\epsilon_0 V}}b$, where $a(x) = N^{-1/2}\sum_k e^{ikx}a_k$ and b are bosonic annihilation operators, ck_0 is the center frequency of the gate field, and V is the quantization volume. Additionally, $\mathcal{E}$ is the amplitude of the cavity input field, $\omega_{\mu\nu}$ is the atomic transition energy between states μ and ν, Ω is the classical Rabi field for the coupling field, Γ is the linewidth of the excited states $|d\rangle$ and $|e\rangle$, γ is decoherence rate of two stable ground states $|g\rangle$ and $|s\rangle$, and g_g, g_s are the bare couplings of the atomic transition to the two fields. We take the gate and signal fields to be resonant with the atoms so that $ck_0 = \omega_{gd}$ and $\omega_c = \omega_{se}$.

The use of this effective Hamiltonian is sufficient to describe the steady state for the case of weak input fields $g_g\left\langle a^\dagger a\right\rangle \ll \Omega^2/\Gamma$ and $g_s\left\langle b^\dagger b\right\rangle \ll \kappa$. In this limit we can take the approach of Carmichael et al. (1991) to calculate the two time correlation function between the two fields

$$g^{(2)}_{gs}(x,\tau) = \frac{\langle b^\dagger(t)a^\dagger(x,t+\tau)a(x,t+\tau)b(t)\rangle}{\langle a^\dagger(x,t)a(x,t)\rangle\langle b^\dagger(t)b(t)\rangle} \tag{5.2}$$

In this limit we can write the density matrix as a product state $\rho = |\chi(\tau)\rangle\langle\chi(\tau)|$ and we truncate the available states in the system at the level of two excitations from the state with zero photons and all atoms in $|g\rangle$, which we refer to as $|g,0,0\rangle$. The one excitation states are $|g,1_x,0\rangle = a^\dagger(x)|g,0,0\rangle$, $|g,0,1\rangle = b^\dagger|g,0,0\rangle$, $|d_x,0,0\rangle \equiv \sigma^x_{dg}|g,0,0\rangle$, and $|s_x,0,0\rangle \equiv \sigma^x_{sg}|g,0,0\rangle$, where $\sigma^x_{\mu\nu} = |\mu\rangle_x\langle\nu|$. The two excitation states that are relevant for $g^{(2)}_{gs}$ are $|g,1_x,1\rangle \equiv a^\dagger(x)|g,0,1\rangle$, $|d_x,0,1\rangle \equiv b^\dagger|d_x,0,0\rangle$, $|s_x,0,1\rangle \equiv b^\dagger|s_x,0,0\rangle$, and $|e_x,0,0\rangle \equiv \sigma^x_{es}|s_x,0,0\rangle$.

We then expand $|\chi(t)\rangle$ in these states and find the evolution according to $i\frac{d|\chi\rangle}{dt} = H_{eff}|\chi\rangle$ applying the boundary condition that the free space input field is a weak coherent state. The only terms in H_{eff} which create excitations are the driving fields, which are perturbative implying that the amplitude of the one excitation states are proportional to $\mathcal{E}$ and the two excitation amplitudes are proportional to $\mathcal{E}^2$.

To calculate $g^{(2)}_{gs}(\tau)$ we take the picture where the detection corresponds to a quantum jump from the steady state $|\chi_{ss}\rangle$ into the state $a(x,t)|\chi_{ss}\rangle$ for $\tau < 0$ and $b(t)|\chi_{ss}\rangle$ for $\tau > 0$ (Carmichael et al., 1991). To find $g^{(2)}_{gs}(\tau)$ we can then simply evolve the operator $n_s(t)$ or $n_g(x,t)$ for a time τ under H_{eff} starting from the jump state.

To find the steady state we expand $|\chi(t)\rangle$ in the zero, one and two excitation states

$$|\chi(x,t)\rangle = |f,0,0\rangle + A_0^1(x)\,|f,1_x,0\rangle + A_1^1(x)\,|g_x,0,0\rangle + A_2^1(x)\,|d_x,0,0\rangle + A_3^1\,|f,0,1\rangle$$
$$+ A_1^2(x)\,|f,1_x,1\rangle + A_2^2(x)\,|g_x,0,1\rangle + A_3^2(x)\,|d_x,0,1\rangle + A_4^2(x)\,|e_x,0,0\rangle \tag{5.3}$$

where we neglect the one and two excitations in the normalization because they are perturbative. The equations of motion are for the A_i^j are found from $i\frac{d|\chi\rangle}{dt} = H_{eff}\,|\chi\rangle$.

$$(\partial_t + c\,\partial_x)A_0^1(x) = -ig_{fd}\sqrt{N}\,A_2^1(x), \tag{5.4}$$
$$\partial_t A_2^1(x) = -\Gamma/2A_2^1(x) - ig_g\sqrt{N}\,A_0^1(x) - i\Omega/2A_1^1(x), \tag{5.5}$$
$$\partial_t A_1^1(x) = -\gamma/2A_1^1(x) - i\Omega/2A_2^1(x), \tag{5.6}$$
$$\partial_t A_3^1 = -\kappa/2A_3^1 + \mathcal{E}, \tag{5.7}$$
$$(\partial_t + c\,\partial_x)A_1^2(x) = -\kappa/2A_1^2(x) + \mathcal{E}A_0^1(x) - ig_g\sqrt{N}A_3^2(x), \tag{5.8}$$
$$\partial_t A_3^2(x) = -(\Gamma+\kappa)/2A_3^2(x) - ig_g\sqrt{N}A_1^2(x) - i\Omega/2A_2^2(x) + \mathcal{E}A_2^1(x), \tag{5.9}$$
$$\partial_t A_2^2(x) = -(\kappa+\gamma)/2A_2^2(x) - ig_sA_4^2(x) - i\Omega/2A_3^2(x) + \mathcal{E}A_1^1(x), \tag{5.10}$$
$$\partial_t A_4^2(x) = -\Gamma/2\,A_4^2(x) - ig_sA_2^2(x) \tag{5.11}$$

These eight equations are the only ones relevant for $g^{(2)}_{gs}(t)$, they give the steady state

$$\bar{A}^1_0(x) = \alpha \exp\Big(-\frac{2g_g^2 N}{\Gamma + \Omega^2/\gamma}\frac{x}{c}\Big) = \alpha \exp\Big(-\frac{\mathcal{N}}{2(1+\Omega^2/\gamma\Gamma)}\frac{x}{L}\Big) \tag{5.12}$$

$$\bar{A}^1_1(x) = -\frac{2g_g\sqrt{N}\,\Omega}{\Omega^2 + \gamma\Gamma}\bar{A}^1_0(x), \tag{5.13}$$

$$\bar{A}^1_2(x) = -\frac{i2g_g\sqrt{N}}{\Gamma + \Omega^2/\gamma}\bar{A}^1_0(x), \tag{5.14}$$

$$\bar{A}^1_3 = \frac{\mathcal{E}}{\kappa/2}, \tag{5.15}$$

$$\frac{\bar{A}^2_1(x)}{\bar{A}^1_0(x)\bar{A}^1_3} = \frac{1}{1+\eta} + \frac{\eta}{1+\eta}\exp\Big(-\frac{\mathcal{N}}{2\zeta}\frac{x}{L}\Big) + \mathcal{O}(\kappa/\Gamma) \tag{5.16}$$

where α is the amplitude of the input coherent state, N is the number of atoms, $\mathcal{N} = 4g_g^2 NL/c\Gamma$ is the optical depth, L is the length of the medium, $\eta = 4g_s^2/\kappa\Gamma$ is the cooperativity, and we have defined

$$\zeta = \Big(1 + \frac{\gamma\Gamma}{\Omega^2}\Big)\Big(1 + \frac{\Omega^2/\kappa\Gamma + \gamma/\kappa}{1+\eta}\Big) \tag{5.17}$$

a correction factor that arises from imperfect EIT, which reduces the effective switching by decreasing the atomic-excitation component of the polariton.

When $\tau < 0$ the free space photon is detected first leading to a quantum jump into the state

$$|\chi_J\rangle = \frac{a(L,\tau)\,|\chi_{ss}\rangle}{\sqrt{\langle\chi_{ss}|\,a^\dagger(L,\tau)a(L,\tau)\,|\chi_{ss}\rangle}} = |f,0,0\rangle + \frac{\bar{A}^2_1(L)}{\bar{A}^1_3}\,|f,0,1\rangle \tag{5.18}$$

Now

$$g_{gs}^{(2)}(\tau) = \frac{\langle\chi_J(t)|\, b^{\dagger}(\tau)b(\tau)\,|\chi_J(t)\rangle}{\langle\chi_{ss}|\, b^{\dagger}(\tau)b(\tau)\,|\chi_{ss}\rangle} = \frac{|\tilde{A}_3^1(t)|^2}{\left|\bar{A}_3^1\right|^2} \tag{5.19}$$

$$= \left[1 - \left(1 - e^{-\mathcal{N}/2\zeta}\right)\frac{\eta}{1+\eta}e^{-\kappa_<|\tau|/2}\right]^2 \tag{5.20}$$

where $\kappa_< = \kappa$. For $\tau > 0$ the procedure is the same, except we have to evolve Eqs. 4-6 starting from the initial conditions $A_0^1(x,\tau) = \bar{A}_1^2(x)$, $A_1^1(x,\tau) = \bar{A}_2^2(x)$, and $A_2^1(x,\tau) = \bar{A}_3^2(x)$. This corresponds to the state $|\chi_J\rangle \propto b\,|\chi_{ss}\rangle$. The result can be expressed in the same form as Eq. 5.19 with $\kappa_<$ replaced by $\kappa_> = \Omega^2/\Gamma + \gamma(v_g/L)$ in the limit of small(large) optical depth.

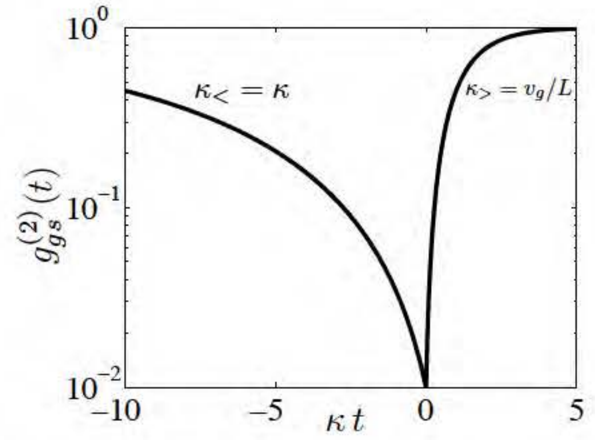

Figure 5.2: Time ordered cross-correlation function $g_{gs}^{(2)}(t)$ of the gate and signal field in steady state in the limit of large $\mathcal{N}$. Parameters are such that the cooperativity is $\eta = g_s^2/\kappa\Gamma = 4.5$, the group velocity for the gate field is $v_g/c = \Omega_c^2/g_1^2 N = 10^{-4}$, and $\kappa = 10^{-3}c/L$.

5.3 Experimental Results

In the limit of large optical depth $\mathcal{N}/\zeta \gg \ln\eta$ every incoming gate photon is converted into a slow-light polariton (Fleischhauer et al., 2005) with a near-unity atomic excitation component in state $|s\rangle$. In this case, the cavity transmission is modified by the single intracavity atom (Tanji-Suzuki et al., 2011) and is given by $(1+\eta)^{-2}$, which is also the minimum value of the cross-correlation function $g_{gs}^{(2)}(0)$ in this limit. This is the limit shown theoretically in Fig. 5.2 In the opposite limit of large cooperativity $\eta \gg 1$ and moderate optical depth, $\mathcal{N}/\zeta \ll \ln\eta$, the signal photon completely destroys EIT, and $g_{gs}^{(2)}(0) \approx e^{-\mathcal{N}}$ is simply the probability for the gate photon to pass through the absorbing medium in the absence of EIT. Interestingly, the correlation function $g_{gs}^{(2)}(t)$ is asymmetric in the time separation t between the photons (Hennessy et al., 2007). This can be understood as follows: the detection of a signal photon at time $t = 0$ implies that the EIT transmission must have been reduced for times $t < 0$ on a time scale on the order of the cavity lifetime κ^{-1}, and will approach its uncorrelated steady-state value $g_{gs}^{(2)} = 1$ for times $t > 0$ with a time constant determined by the polariton lifetime, which depends on the EIT linewidth Ω^2/Γ in the limit of small optical depth. (An analogous argument can be made if one assumes the gate photon to be detected at t = 0.)

The measured cross-correlation function $g_{gs}^{(2)}(t)$ displayed in Fig. 5.3 shows that photons in the two modes are uncorrelated for large time separation t, but display a marked anticorrelation dip near $t = 0$: when the two photons derived from independent lasers arrive near-simultaneously, they reduce each others transmission. The data in Fig. 5.3 are well described by Eq. 5.19 using a three-parameter fit with the

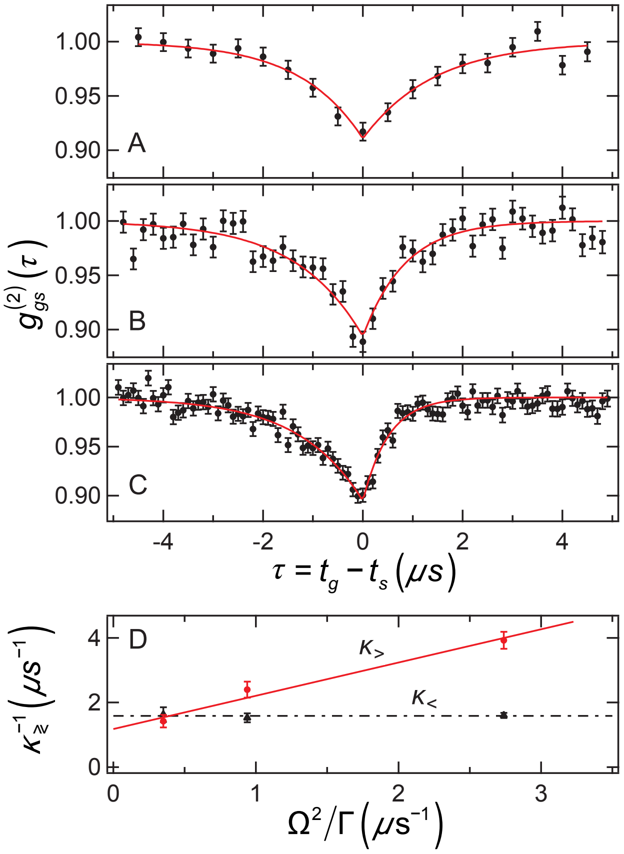

Figure 5.3: Mutual photon-photon switching in continuous operation. The second-order cross correlation function $g^{(2)}_{gs}(\tau)$ is displayed versus time separation $\tau = t_g - t_s$ between photons in the gate and signal modes for different coupling beam Rabi frequencies: (A) $\Omega/2\pi = 0.5$ MHz, (B) $\Omega/2\pi = 0.9$ MHz, and (C) $\Omega/2\pi = 1.5$ MHz. Fits of the data to the model (see text) yield (A) $g^{(2)}_{gs}(0) = 0.91 \pm 0.01, \kappa_< = (1.6 \pm 0.2)\ \mu s{-}1, \kappa_> = (1.4 \pm 0.2)\ \mu\mathrm{s}^{-1}$, (B) $g^{(2)}_{gs}(0) = 0.89 \pm 0.01, \kappa_< = (1.5 \pm 0.1)\ \mu\mathrm{s}^{-1}, \kappa_> = (2.4 \pm 0.3)\ \mu\mathrm{s}^{-1}$, and (C) $g^{(2)}_{gs}(0) = 0.90 \pm 0.01, \kappa_< = (1.6 \pm 0.1)\ \mu\mathrm{s}^{-1}, \kappa_> = (3.9 \pm 0.3)\ \mu\mathrm{s}^{-1}$. (D) Fitted rate constants $\kappa_{><}$ versus EIT linewidth Ω^2/Γ. The positive-time rate constant fits to $\kappa_> = a\Omega^2/\Gamma + b$ with slope $a = 1.0 \pm 0.1$ and y-axis intercept $b = 2\pi(190 \pm 30)$ kHz, which agrees with the expected values a = 1 and $b = \gamma = 2\pi(179 \pm 10)$ kHz. The negative-time rate constant $\kappa_< = 1.6\ \mu\mathrm{s}^{-1}$ is independent of the coupling laser intensity and is larger than the cavity linewidth $\kappa = 0.89\ \mu\mathrm{s}^{-1}$ due to incomplete optical pumping leading to cavity absorption. The measurements were performed at photon numbers $\langle n_s \rangle \approx 0.1$ and $\langle n_g \rangle \approx 0.2$ when integrated over a time windows $1/\kappa_<$ and $1/\kappa_>$, respectively.

zero-time value $g_{gs}^{(2)}(0)$ and the two decay rate constants κ/γ. The time constants obtained from the fit confirm the asymmetric shape of the cross-correlation function (Fig. 5.3D): $\kappa_< = (1.6 \pm 0.1)\ \mu\mathrm{s}^{-1}$ is independent of control Rabi frequency and 80% larger than the cavity linewidth κ, presumably due to the occasional presence of absorbing atoms in the state $|s\rangle$ due to imperfect optical pumping. (Note that even only one atom out of $\mathrm{N} = 2 \cdot 10^4$ is sufficient to substantially increase the cavity linewidth by a factor $1+\eta$.) On the other hand, the positive-time constant $\kappa_>$ is linearly dependent on coupling beam intensity and agrees with the prediction $\Omega^2/\Gamma+\gamma$, where Ω^2/Γ and $\gamma/(2\pi) = (179 \pm 10)$ kHz have been independently determined from separately measured EIT spectra. The fitted $g_{gs}^{(2)}(0)$ is between 0.89 ± 0.01 and 0.91 ± 0.01 for the three values of the coupling Rabi frequency. This agrees well with the prediction from Eq. 5.19 with values between 0.87 ± 0.02 and 0.93 ± 0.02, using the independently measured optical depth, fitted $\kappa_{><}$, and reduced cooperativity $\eta' = \eta\, \kappa/\kappa_<$ due to imperfect optical pumping. The measured zero-time correlation $g_{gs}^{(2)}(0)$ corresponds to a mutual photon-photon switching efficiency of $1 - g_{gs}^{(2)}(0) = 11\%$ of one photon by the other in continuous operation.

5.4 Conclusions

This system constitutes a testbed in which we have explored the physical principles relevant to an all-optical transistor based on cavity QED with an atomic ensemble. Before it can be used as a practical device, it will be necessary to improve the input and output coupling efficiencies for the gate and source photons. The combined storage and retrieval efficiency of 3% for the gate photon is limited primarily by the optical density. The latter could be improved by using a deeper trap, in combination with further cooling of the atomic ensemble, which would also increase the gate photon storage time that is currently limited by Doppler broadening. The cavity outcoupling efficiency for the source photons of 0.66 could be improved to 0.97 by using state-of-the-art mirrors (Birnbaum et al., 2005; Brennecke et al., 2007; Kubanek et al., 2008).

The present work opens up new perspectives for all-optical information processing with strong deterministic interactions between initially uncorrelated, distinguishable photons. The correlations between one gate and multiple source photons produced by the effective photon-photon interaction can be used to create two-mode entangled states of many photons. Finally, cavities with larger cooperativity (Birnbaum et al., 2005; Brennecke et al., 2007; Colombe et al., 2007; Kubanek et al., 2008), may enable high-fidelity deterministic photonic quantum gates.

Chapter 6

Few Body Physics in Strongly Interacting Rydberg-Polariton Gases

6.1 Introduction

Electromagnetically Induced Transparence (EIT) can be used to convert photons coherently into atomic excitations and back (Fleischhauer et al., 2005). However, EIT by itself is linear in the photon field, and as such cannot be used to induce interactions between individual photons. In the optical transistor described in the previous chapter, the gate photon is converted into an atomic excitation by means of EIT, and then the strong interaction between the one excited atom and the source photons is accomplished via cavity QED, resulting in strong coupling. In an alternative free-space approach one can directly realize strong photon-photon interactions via EIT involving atomic Rydberg levels with strong mutual atom-atom interactions. The basic idea is that while a photon is traveling through the medium as a Rydberg polariton with substantial population amplitude in the Rydberg level, within a certain characteristic distance range of the first photon (the so-called blockade radius) the second photon cannot experience EIT because the Rydberg level is shifted due to the atomic Rydberg-Rydberg interaction (Lukin et al., 2001; Pritchard et al., 2010; Gorshkov et al., 2011). For a sufficiently dense atomic sample, such that a photon can be absorbed on a distance scale comparable to the blockade radius, this causes optical nonlinearities at the level of individual photons.

The basic mechanism underlying the interaction is outlined in Fig. 6.1a. The probe light $\mathcal{E}_p$ couples the ground state $|g\rangle$ to the Rydberg state $|r\rangle$ via an unstable intermediate state $|e\rangle$ of linewidth $\Gamma/2$ by means of a control field Ω_c that is detuned below the resonance frequency of the upper transition $|e\rangle \rightarrow |r\rangle$ by Δ (Fig. 6.1a. Under these conditions, EIT is established when the probe detuning matches that of the control field. However, the Rydberg medium is extremely nonlinear and the medium quickly saturates due to the Rydberg blockade (Gorshkov et al., 2011; Pritchard et al., 2010). This results in a two photon spectrum close to the bare two level response, such that when $\Delta \gg \Gamma$ the nonlinearity is purely dispersive.

Previous work has demonstrated nonlinear phase shifts at the level of two photons and showed that these phase shifts are associated with the formation a two photon bound state in the steady state response (Peyronel et al., 2013). Fig. 6.1b shows an example of such a state, as evidenced by the bunching in the two time correlation function $g^{(2)}(t_2 - t_1)$ that appears when the time separation between the two photons

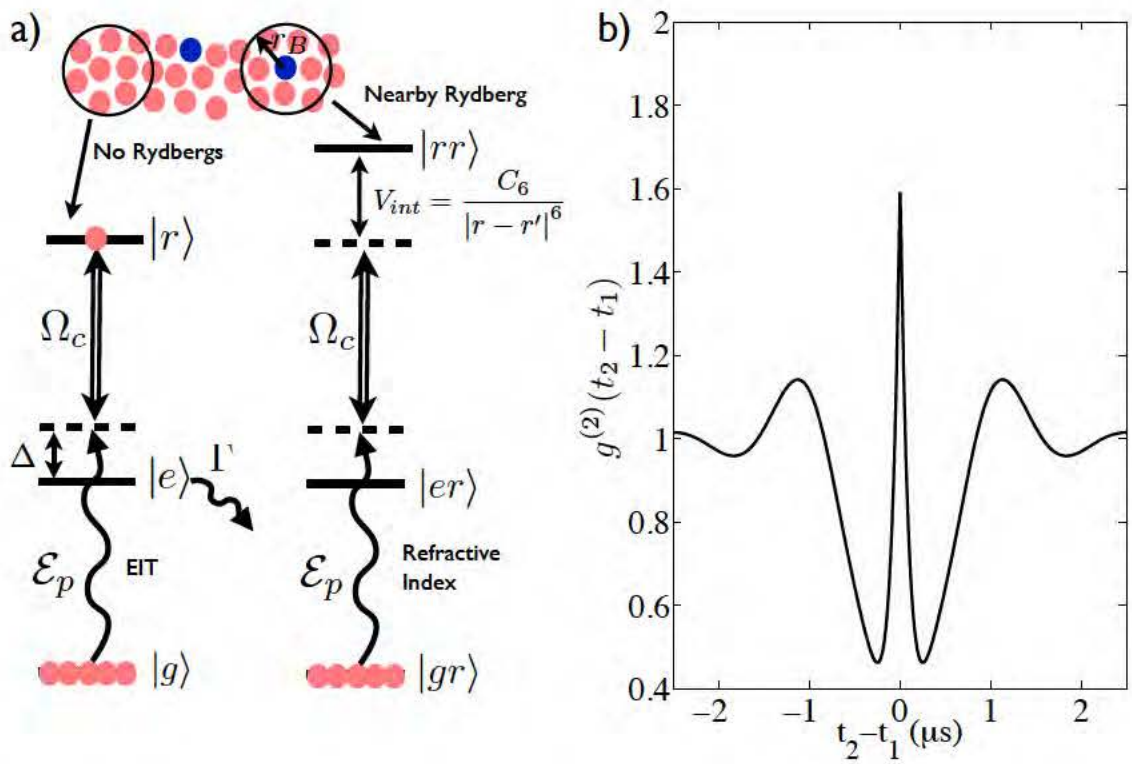

Figure 6.1: a) Schematic of the Rydberg mechanism leading to large dispersive nonlinearities. r_B is the blockade radius, Ω_c is the EIT control field, $\mathcal{E}_p$ is the probe field, Γ is the linewidth of the intermediate state $|e\rangle$ and V_{int} is the Rydberg interaction potential. b) Numerical simulation of $g^{(2}(t)$ in steady state for weak probe fields. We took $\Delta/\Gamma = 2$ a Rydberg blockade radius of 10 μm, a medium of length 100 μm, $\Omega_c = 10$ Mhz and an optical depth of 15, corresponding to a slow light group velocity of $v_g = 600$ m/s.

goes to zero. This figure was obtained from numerical simulations of the steady state two photon problem similar to what is shown in (Peyronel et al., 2013). In what follows we look more closely at the time dependent dynamics of the two photon states, including their formation and the change in their group velocity as the interaction strength is increased. We then look at the formation of three photon bound states in steady state and calculate the three time correlation function $g^{(3)}(t_1, t_2, t_3)$.

6.2 Numerical Approach for Atom-Photon Interactions

Atoms are nonlinear optical elements that can be used to make single photon cavities, photon transistors, etc. Simulation of even single atom-single photon interaction problem is non-trivial, particularly if photon is not a "single-mode" (e.g. lives in a waveguide). Our approach is to directly simulate the unitary evolution of the atom(s)-photon(s) system wavefunction,

$$|\Psi(t)\rangle = e^{iHt}|\Psi(0)\rangle \tag{6.1}$$

where the Hamiltonian is

$$\begin{aligned} H &= H_0 + H' && (6.2)\\ H_0 &= \sum_k \epsilon_k a_k^\dagger a_k + \sum_a \frac{E_a}{2}(\sigma_a^z + 1), && (6.3)\\ H' &= \sum_a g_a(a_{r_a}^\dagger \sigma_a^- + a_{r_a}\sigma_a^+). && (6.4) \end{aligned}$$

The complication is that photon parts of H_0 and H' are diagonal in different spaces, in momentum and real, respectively. To deal with this complication we can use the Trotter decomposition:

$$|\psi(t)\rangle = \mathcal{T}e^{-i\int_0^t dt' H}|\psi(0)\rangle = \Pi_i e^{-iH\Delta t}|\psi(0)\rangle \approx \Pi_i e^{-iH'\Delta t}e^{-iH_0\Delta t}|\psi(0)\rangle \tag{6.5}$$

$$= \Pi_i \Big(|r\rangle\langle r|e^{-iH'\Delta t}|r\rangle\langle r|k\rangle\langle k|e^{-iH_0\Delta t}|k\rangle\langle k|\Big)\,|\psi(0)\rangle. \tag{6.6}$$

In other words, the state at a given time step is expressed in terms of the state on the previous step as

$$|\psi(t_i)\rangle = e^{-iH'\Delta t}|r\rangle\langle r|k\rangle\langle k|e^{-iH_0\Delta t}|k\rangle\langle k|\psi(t_{i-1})\rangle. \tag{6.7}$$

By (Fourier) transforming between momentum and real space bases, each step of evolution can be processed very efficiently. Here we apply these ideas to the simulation of photons and strongly interacting atoms in Rydberg-Polariton systems.

6.3 Results

Following Gorshkov et al. (2011) we let $\hat{\mathcal{E}}_p^\dagger(z)$, $\hat{\mathcal{S}}^\dagger(z)$ and $\hat{\mathcal{P}}^\dagger(z)$ be the slowly varying operators for the creation of a photon, a Rydberg state $|r\rangle$ and an intermediate state $|e\rangle$, respectively. They satisfy the commutation relations $[\hat{\mathcal{E}}(z), \hat{\mathcal{E}}(z')] = \delta(z-z')$, $[\hat{\mathcal{S}}(z), \hat{\mathcal{S}}(z')] = \delta(z-z')$ and $[\hat{\mathcal{P}}(z), \hat{\mathcal{P}}(z')] = \delta(z-z')$. The equations of motion are

$$\partial_t \hat{\mathcal{E}}_p = -c\partial_z \hat{\mathcal{E}} + ig_p/2\hat{\mathcal{P}} \tag{6.8}$$

$$\partial_t \hat{\mathcal{P}} = -\Gamma/2\hat{\mathcal{P}} + ig_p/2\hat{\mathcal{E}} + i\Omega_c/2\hat{\mathcal{S}} \tag{6.9}$$

$$\partial_t \hat{\mathcal{S}} = i\Omega_c/2\hat{\mathcal{P}} - i\int dz' V(z-z')\hat{\mathcal{S}}^\dagger(z')\hat{\mathcal{S}}(z')\hat{\mathcal{S}}(z) \tag{6.10}$$

where g_p is the collective atom photon coupling which we define by $g_p^2 = \Gamma c/\ell_a$ where $\ell_a = L/OD$ is the absorption length and OD is the optical depth. $V(z-z') = C_6/(z-z')^6$ is the Rydberg interaction which is characterized by the blockade radius $r_B = (2C_6\Gamma/\Omega_c)^2$ defining the boundary where $V(r)$ is greater than the EIT linewidth Ω_c^2/Γ.

By projecting Eqs. 6.8-10 onto the two excitation manifold we obtain a closed set of equations for the two photon dynamics, which we solve numerically using the techniques described in section 6.2 As an example Fig. 6.2a shows a pulse with detuning $\Delta = 2\Gamma$ and no two photon detuning after traveling through the medium. We clearly see the bunching, indicating the presence of the bound state analogously to Fig. 6.1b.

Since the Rydberg interaction is a short range interaction (note: a $1/r^n$ potentials is considered short ranged if n¿d the dimension) it is reasonable to ask whether it can be approximated by a delta potential. Therefore, as an ansatz for the system we use a modified Nonlinear Schrodinger Equation (NLSE) governed by the Hamiltonian

$$H = -\sum_i i v_G \frac{\partial}{\partial x_i} + \frac{1}{2m}\frac{\partial^2}{\partial x_i^2} - \frac{U}{2}\sum_{i,j}\delta(x_i - x_j) \tag{6.11}$$

where $v_g = c/(1+g_p^2/\Omega_c^2)$ is the EIT group velocity and $m = -\frac{1}{16\pi}\frac{c}{v_g}\frac{\lambda}{\ell_a}\frac{1}{i+\Delta/\Gamma}\frac{\hbar\omega}{c^2}$ is the effective photon mass arising from the finite bandwidth of EIT (Fleischhauer et al., 2005). The interaction paramter U is given by

$$U = \frac{c_0}{8\,m}\frac{\Gamma^2}{\Delta^2}\frac{r_B}{\ell_a^2} = \frac{c_0}{8m}\frac{\Gamma^2}{\Delta^2}\frac{OD_B}{\ell_a} \tag{6.12}$$

where $OD_B = r_B/\ell_a$ and $c_0 = 0.92$ is a numerical factor. In order for the NLSE to be self-consistent it is necessary that the extent of the bound states is much larger than the blockade radius. Note that U is negative, which normally corresponds to repulsion, but because $m < 0$ it acts as an attractive potential.

6.3.1 Two Photon Solitons

Solving for the two photon bound states with Eq. 6.11 gives the dispersion of the bound states as (Ben-Aryeh, 1999)

$$E_B(k) = v_g k + \frac{k^2}{2m} - \frac{1}{4} m U^2 \tag{6.13}$$

To calculate the expected change in group velocity in this model we note that since our input state is at zero two photon detuning it excites the bound state at $E_B(k) = 0$ which is shifted away from $k = 0$. This gives rise to additional phase accumulation as discussed by Peyronel et al. (2013), but also a change in the group velocity

$$\frac{\delta v_g}{v_g} = \sqrt{1 + \frac{U^2}{2 v_g^2}} - 1 = \sqrt{1 + \frac{c_0^2}{2} \frac{\Gamma^2}{\Delta^2} OD_B^2} - 1 \tag{6.14}$$

Since the approximation of a delta potential is uncontrolled we also calculated the change in v_g using full time dependent simulations. In Fig. 6.2 these results are compared to Eq. 6.14 where we see that the agreement is good for small OD_B, but they diverge at larger OD_B suggesting other effects are becoming important and the NLSE is not sufficient to describe the dynamics. Finally, we remark that the change in group velocity is a large effect; thus it should be readily observable in experiments.

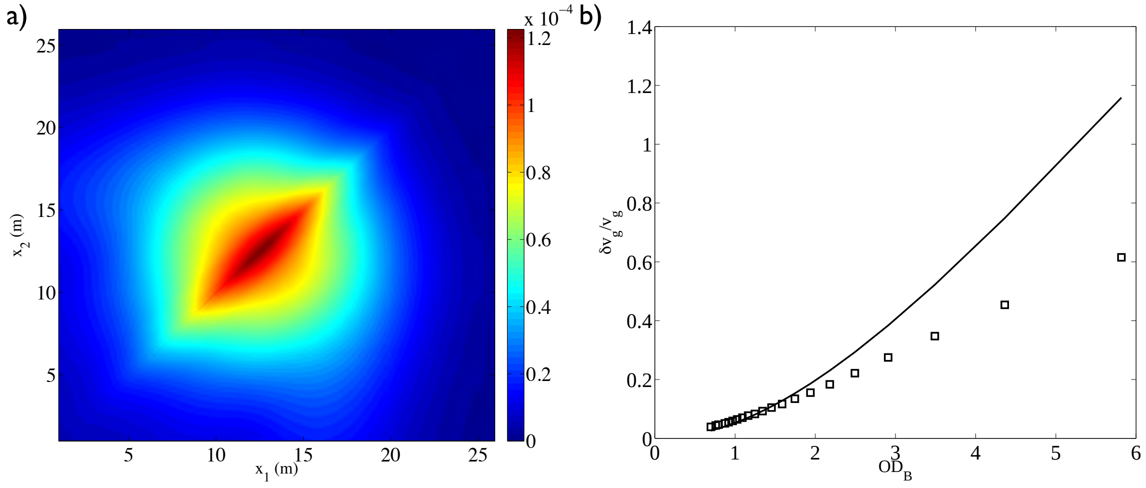

Figure 6.2: a) Two photon pulse after traveling through the medium. We took a gaussian input pulse of width $5(\Omega^2/\Gamma)^{-1}$, otherwise the parameters are as in Fig. 6.1b. b) Comparison between numerical simulations of the change in group velocity vs the change in group velocity for the NLSE. They agree well at small OD_b, but quickly diverge as OD_b increases.

6.3.2 Three Photon Solitons

In addition to the two photon bound states there should also be a manifold of three photon bound states (Ben-Aryeh, 1999). We looked for these by doing numerical simulations of the steady state solution for three photons. The results are shown in Fig. 6.3 in the three time correlation function of the three photons

$$g^{(3)}(t_1, t_2, t_3) = \frac{\langle N_1(t_1) N_2(t_2) N_3(t_3)\rangle}{\langle N_1(t_1)\rangle\langle N_2(t_2)\rangle\langle N_3(t_3)\rangle} \tag{6.15}$$

where $N_i(t_i)$ are photon number operators. Fig 6.3a shows the case where $\Delta = 0$ where we expect no bound state, but instead the three photon version of the dissipative blockade reported by Peyronel et al. (2012). Fig. 6.3b is for the same parameters as Fig. 6.1b with $\Delta = 2\Gamma$ where we see a distinct peak when all three photons arrive

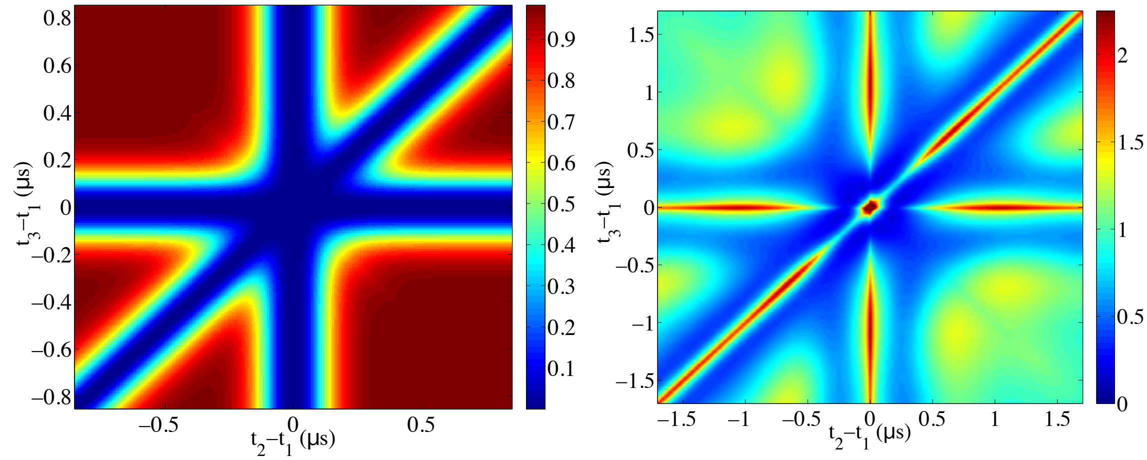

Figure 6.3: a) Three time correlation function $g^{(3)}(t_2 - t_1, t_3 - t_1)$ in steady state with $\Delta = 0$. The lines of reduced probability correspond to regions where two or more photons overlap in the medium. Parameters are as in Fig. 6.1b except with $\Delta = 0$ b) Same parameters as (a) except $\Delta = 2\Gamma$. The peak in the middle corresponds to the three photon bound state while the additional features arise from two photon bound states.

simultaneously. We identify this peak with the three photon bound state.

6.4 Conclusions

We have studied the dynamics and formation of two and three photon solitons in a strongly interacting Rydberg-polariton gas. Such states may be useful for achieving quantum gates between photons and creating large entangled states. In future work we will add repulsion interactions, which may drive the system to a crystalline state of photons.

Appendix A

Appendices to Chapter 2

A.1 Parameters Used in Simulations

In table A.1 below we provide a summary of the parameters used in the simulations for each figure. While many parameters are chosen to be consistent with experiments, not all those presented are self-consistent or experimentally realistic. In particular, in Fig. 2.5e the Λ_0 parameter is unphysically large and in Figures 2.4, 2.5ab and 2.8 the small m_0 values correspond to very large magnetic fields.

A.2 Φ Variables

In this appendix we describe a systematic approach to coarse graining the electron wavefunction in solving the semiclassical equations of motion, which we refer to as the Independent Random Variable Annular Approximation (IRVAA). We construct a sequence of discretizations of the wavefunction for which we can provide a rigorous

Table A.1: Parameters used in the simulations shown in the figures of Chapter 2 and Appendix A.

Fig.	Δ_0	Γ_0	Δ_-	Λ_+	Λ_0	Γ_R	m_0	η	M
2.3	0.5	$0.005 - 0.5$	$0 - 0.4$	0	0	0	0	0.005	400
2.4	$5 \cdot m_0$	$f_c/2$	$1.25 \cdot m_0$	5	$5 \cdot m_0$	$2.7 \cdot \Gamma_0$	$10^{-3} - 10^{-1}$	0	400
2.5ab	0.19	1	0.0048	5.8	0.002	2.7	$5 \cdot 10^{-4}$	0	100
2.5c	0.78	1	0.19	5.8	0.08	1	0.01	0	100
2.5e	1	1	0.25	0.5	1	1	0.05	0	100
2.6a	1.99	1	0.143	626	0.5	2.7	0.01	0	100
2.6b	1.99	1	0.143	626	0.5	2.7	0.01	10^{-4}	100
2.7a	0.014	0.36	0.0034	5	0.014	$2.7 \cdot \Gamma_0$	0.0027	$4 \cdot 10^{-4}$	200
2.7b	0.013	2.1	0.0034	5	0.013	$2.7 \cdot \Gamma_0$	0.0027	$2 \cdot 10^{-3}$	200
2.8	$5 \cdot m_0$	$f_c/2$	$1.25 \cdot m_0$	5	$5 \cdot m_0$	$2.7 \cdot \Gamma_0$	$10^{-3} - 10^{-1}$	10^{-4}	400
A.1a	0	1	0	0	0	0	0	10^{-3}	600
A.1b	0.5	$0.005 - 0.5$	$0 - 0.4$	0	0	0	0	$5 \cdot 10^{-5}$	1200

bound on the error in time evolution compared to the exact solution. In the process we also introduce a new set of statistically independent nuclear spin variables, which are a convenient basis for numerical simulations.

We see from Eqs. 2.4 and 2.6 that the semiclassical evolution of each spin depends only on the vectors $\mathbf{L}$ and $\mathbf{R}$ (or equivalently on $\mathbf{D}$ and $\mathbf{S}$). That is, if we know $\boldsymbol{P}_d(t)$ (which depends only on $\mathbf{L}$ and $\mathbf{R}$), then we can solve for the dynamics of the entire system. However, even if we know $\boldsymbol{P}_d(t)$, if we look at the equation of motion for $\boldsymbol{L}$ we find that it generates an infinite hierarchy of equations

$$\frac{d\boldsymbol{L}}{dt} = \boldsymbol{P}_l \times \mathbf{L}^*, \tag{A.1}$$

where we defined $\boldsymbol{L}^* \equiv \sum_k g_{kl}^2 \mathbf{i}_{kl}$. Now $\dot{\boldsymbol{L}}^*$ couples to the variable $\sum_k g_{kl}^3 \mathbf{i}_{kl}$ and so on.

To find an approximate solution to the dynamics we would like to find an effective method to truncate this infinite hierarchy of equations. For simplicity we focus on the case where $\boldsymbol{P}_\ell$ is only a function of $\boldsymbol{L}$, reducing it to a single dot problem, and drop the dot indices in the following discussion. We also work in the continuum limit, which is defined by a nuclear angular momentum density $\boldsymbol{I}(\boldsymbol{r}, t) = \sum_k \mathbf{i}_k(t)\delta(\boldsymbol{r} - \boldsymbol{r}_k)$.

Each variable in the hierarchy of equations of motion (as in Eq. A.1) can be expressed as an integral

$$\boldsymbol{\Phi}(t) = \int d^d r\, g(\boldsymbol{r})\, \varphi(g(\boldsymbol{r}))\, \boldsymbol{I}(\boldsymbol{r}, t), \tag{A.2}$$

where $\varphi(x)$ is a polynomial in x. That is, there is a one-to-one correspondence between polynomials $\varphi(x)$ and the variables in the EOM. For example, $\boldsymbol{L}$ corresponds to $\phi(x) = 1$.

We would like to think of a truncation procedure as any procedure that provides a reduced, self-consistent set of equations describing the evolution of $\boldsymbol{P}$, equivalently $\boldsymbol{L}$. We make a formal definition of a truncation procedure as a procedure producing a set of variables $\boldsymbol{\Phi}_k$, $k = 1, \ldots, M$, of the form above and an $M \times M$ matrix Q, such that $\boldsymbol{\Phi}_1 = \boldsymbol{L}$ and

$$\frac{d\boldsymbol{\Phi}_k}{dt} = \sum_\ell \boldsymbol{P} \times Q_{k\ell} \boldsymbol{\Phi}_\ell.$$

Since we always constrain $\boldsymbol{\Phi}_1 = \boldsymbol{L}$, we always have $\phi_1(x) = 1$.

To construct a convenient basis of nuclear spin variables we first define a norm $\langle \cdot \rangle_\varphi$ based on the statistical average of a nuclear spin variable in the infinite temperature ensemble, i.e.

$$\begin{aligned}\langle \Phi \cdot \Psi \rangle_{\varphi} &= \int d^d r \, d^d r' \, g^2(r) \varphi(g(r)) \psi(g(r')) \left\langle \boldsymbol{I}(\boldsymbol{r}) \cdot \boldsymbol{I}(\boldsymbol{r}') \right\rangle_e \\ &= \frac{I(I+1)}{a^d} \int d^d r \, g^2(r) \varphi(g(r)) \psi(g(r)) \end{aligned} \tag{A.3}$$

where a is the lattice spacing, $\langle \cdot \rangle_e$ is the ensemble average over the initial thermal state and we took $\langle \boldsymbol{I}(\boldsymbol{r}) \cdot \boldsymbol{I}(\boldsymbol{r}') \rangle = I(I+1)\delta(\boldsymbol{r}-\boldsymbol{r}')/a^d$. Now we can construct an orthogonal set of polynomials with respect to this norm by using the standard Gram-Schmidt procedure starting from the polynomial 1. This gives a set of orthogonal polynomials φ_k and associated nuclear spin variables $\boldsymbol{\Phi}_k = \int d^d r \, g(\boldsymbol{r}) \varphi_k(g(\boldsymbol{r})) \boldsymbol{I}(\boldsymbol{r}, t)$, which are statistically independent in the infinite temperature ensemble (*i.e.*, $\langle \boldsymbol{\Phi}_k \cdot \boldsymbol{\Phi}_l \rangle = 3\Omega_l^2 \delta_{kl}$)and satisfy $\boldsymbol{\Phi}_1 = \boldsymbol{L}$.

The equations of motion (EOM) for these variables can be written as

$$\dot{\boldsymbol{\Phi}}_n = \boldsymbol{P} \times Q_{nm} \boldsymbol{\Phi}_m \tag{A.4}$$

where the matrix Q_{mn} is a tridiagonal matrix defined by the recurrence relations

$$x\varphi_n(x) = Q_{nn-1}\varphi_{n-1} + Q_{nn}\varphi_n + Q_{nn+1}\varphi_{n+1} \tag{A.5}$$

and we used the fact that $x\varphi_n(x)$ only has a non-zero overlap with φ_n and $\varphi_{n\pm1}$.

We now define an Mth order truncation procedure with respect to the variables $\boldsymbol{\Phi}_k$ by setting $Q_{MM+1} = 0$. The central result of this appendix is encapsulated by the following theorem for this truncation procedure.

Theorem: *For a given wavefunction $g(\boldsymbol{r})$ and $\varepsilon > 0$, the above truncation procedure at order M will produce an effective $\boldsymbol{L}^M(t)$such that $\left|\boldsymbol{L}(t) - \boldsymbol{L}^{\boldsymbol{M}}(t)\right| < \varepsilon$ for all $t < t_M$, where t_M is a time scale that increases linearly with M and $\boldsymbol{L}(t)$ is the exact result for the untruncated system.*

We begin our analysis by proving that any truncation procedure is equivalent to a discretization of the function $g(\boldsymbol{r})$ (i.e., an annular approximation), by which we mean a representation of $\boldsymbol{L}$ as

$$\boldsymbol{L} = \sum_{k=1}^{M} g(\boldsymbol{r}_k)\tilde{\boldsymbol{I}}_k, \tag{A.6}$$

where $\tilde{\boldsymbol{I}}_k$ is a rescaled nuclear spin variable associated with position $\boldsymbol{r}_k$.

The reverse implication is clear because if we start with such a discrete representation, then the variable associated with the polynomial

$$w(x) = \prod_{k=1}^{M} [x - g(\boldsymbol{r}_k)]$$

is identically zero. That is, if there are only M discrete spins in the system, then there are only M statistically independent variables $\boldsymbol{\Phi}_k$ in the system, and $\boldsymbol{\Phi}_{M+1}$ is naturally zero. This result naturally truncates Eq. A.4. Consequently, if we consider any basis of polynomials of degree less than M and its associated set of spin variables, then we can obtain a finite, self-consistent set of equations for the evolution of $\boldsymbol{L}$.

The forward implication follows along similar lines. If $M-1$ is the maximal degree of the set of polynomials $\{\varphi_k(x)\}$ associated with the truncation variables $\{\boldsymbol{\Phi}_k\}$ and Φ_M is the spin variable corresponding to this polynomial, then, when we compare to the continuum limit, we find that the statement that $d\Phi_M/dt$ does not couple to higher degree polynomial variables implies the existence of a degree-M polynomial $w(x)$ such that

$$\int d^d r\, g(\boldsymbol{r})\, w(g(\boldsymbol{r}))\, \boldsymbol{I}(\boldsymbol{r},t) = 0,$$

for any $\boldsymbol{I}(\boldsymbol{r},t)$. The existence of such a polynomial immediately implies that we can represent $\boldsymbol{L}$ in the discretized form of Eq. A.6.

We have now reduced the problem of finding an optimal truncation procedure to the problem of finding an optimal discretization procedure for integrals of the form

$$\int d^d r\, g(\boldsymbol{r}) \varphi(g(\boldsymbol{r}))\, \boldsymbol{I}(\boldsymbol{r},t),$$

where $\varphi(x)$ is a polynomial in x. Fortunately, this last problem is solved through the theory of Gaussian quadrature. (Kress, 1998) First, though, we assume that our function $g(\boldsymbol{r})$ is spherically symmetric so that we can write our integrals as effective one-dimensional integrals with respect to the rescaled angular momentum density

$$\boldsymbol{I}(r,t) = \int d\Omega\, a^{d-1}\, N(r)\, \boldsymbol{I}(r,\boldsymbol{\Omega},t)/S(d) \tag{A.7}$$

where $\boldsymbol{\Omega}$ parameterizes the surface of a d-dimensional sphere, a is the lattice spacing, $S(d)$ is the surface area of a unit sphere in d dimensions, and $N(r) \equiv S(d)\, r^{d-1}/a^{d-1}$ is the number of nuclear spins at radius r; for example, in two dimensions $N(r) = 2\pi r/a$. The ensemble average of $\boldsymbol{I}(r,t)$ is given by $\langle \boldsymbol{I}(r) \cdot \boldsymbol{I}(r') \rangle = I(I+1)N(r)\delta(r-r')/a$.

To begin constructing our Gaussian quadrature rules we rewrite

$$\begin{aligned}\mathbf{\Phi}(t) &= \int_0^\infty dr N(r) g^2(r) \varphi(g(r)) \frac{\boldsymbol{I}(r,t)}{N(r)g(r)} \\ &= \int_0^1 dx\, \omega(x) \varphi(x) \frac{\boldsymbol{I}\big(g^{-1}(x),t\big)}{N\big(g^{-1}(x)\big)x}\end{aligned} \tag{A.8}$$

where $x = g(r)$ and $\omega(x) = \frac{dg}{dr}|_{g^{-1}(x)} N\big(g^{-1}(x)\big)x^2$ is the weight function. Standard results in the theory of numerical integration imply the existence of a set of orthogonal polynomials, φ_n, with respect to the inner product

$$(f,h) = \int_0^1 dx\, \omega(x)\, f(x)\, h(x) \tag{A.9}$$

such that, for any function $f(x)$, the Mth order quadrature approximation is given by

$$\int_0^1 dx\, \omega(x)\, f(x) \approx \sum_{k=1}^{M} \omega_k\, f(x_k), \tag{A.10}$$

where x_k are the zeros of φ_M and the weights ω_k are determined by the condition that Eq. A.10 is exact for all polynomials of degree strictly less than $2M$. The error in this formula decreases exponentially in M, or better, provided that f is smooth. (Kress, 1998) In addition, these polynomials are exactly the ones we used to construct our truncation procedure. Consequently, our truncation procedure defined above is equivalent to approximating $\boldsymbol{L}$ in quadrature as in Eq. A.6 with $\tilde{\boldsymbol{I}}_k = w_k \boldsymbol{I}(r_k,t)/g_k^2 N(r_k)$.

To prove the theorem we first note that from the definition $|\boldsymbol{P}(\boldsymbol{L})| \leq 1$ for all $\boldsymbol{L}$. Now let $p > 0$ be such that $|\boldsymbol{P}(\boldsymbol{L}) - \boldsymbol{P}(\boldsymbol{L}^{'})| < p|\boldsymbol{L} - \boldsymbol{L}^{'}|$ for all $\boldsymbol{L}$ and $\boldsymbol{L}^{'}$. We define $\boldsymbol{L}_n(t) \equiv \int d^d r g^n(\boldsymbol{r}) \boldsymbol{I}(\boldsymbol{r},t)$ and $\boldsymbol{L}_n^M(t)$ is the solution for the equivalent variable in the truncated system of equations. To provide bounds on the error propagation we define $\delta_n^M(t) \equiv |\boldsymbol{L}_n(t) - \boldsymbol{L}_n^M(t)|$. We work in time units where $\max_r g(\boldsymbol{r}) = 1$ and let $b = \max_{n,t}|\boldsymbol{L}_n(t)| \leq \int d^d r g(\boldsymbol{r})(I+1)$. Now it is straightforward to show that

$$\dot{\delta}_n^M \leq pb\,\delta_1^M + (1 + p\delta_1^M)\delta_{n+1}^M \leq \zeta(\delta_1^M + \delta_{n+1}^M) \tag{A.11}$$

where $\zeta = \max(pb, 1 + p\varepsilon)$ and, by assumption, we are restricted to short enough times that $\delta_1^M < \varepsilon$. By construction, $\delta_n^M(0) = 0$ for $n < M$ while for $n > M$ δ_n^M is bounded by the quadrature error on the integral $\int d^d r g^n(\boldsymbol{r})\boldsymbol{I}(\boldsymbol{r}, 0)$, which is less than $c\,e^{-M}$ for a constant c independent of M. Using Eq. A.11 we can then bound the error on $\delta_1^M \leq ce^{-M}(e^{2\zeta t} - 1)$. This implies that the time to make an error of size ε scales as $(1/2\zeta)\log(\varepsilon e^M/c + 1) \sim (M - \log c/\varepsilon)/2\zeta$ for large M. This proves the theorem.

For the two dimensional Gaussian $g(r) \propto e^{-r^2/2\sigma^2}$ the weight function $w(x) = x$ and the associated orthogonal polynomials are the Jacobi polynomials. The matrix Q is then given by standard recurrence relations for Jacobi polynomials. Once the recurrence relations are known, one can work with the Φ-variables without converting between the original nuclear spin variables because the Φ variables were defined such that they are initially statistically independent. This is a convenient numerical approach for these types of central spin problems, and it was used in all of the numerics in this work.

Table A.2: Relative population of the nuclear species x_α, effective hyperfine field due to species α b_α, and the gyromagnetic ratio γ_α, for the three nuclear species in GaAs.

	^{75}As	^{69}Ga	^{71}Ga
x_α	1	0.6	0.4
b_α (T)	-1.84	-1.52	-1.95
$\gamma_\alpha \left(\frac{\text{kHz}}{\text{mT}}\right)$	45.96	64.39	81.81

A.3 Multiple Nuclear Species

In this appendix we include the effects of multiple nuclear species in our simulations and find that the main results for both asymmetric and identical results carry through much the same. First we show how to include multiple species in terms of the collective Φ-variables and then we present the simulation results.

When multiple species are taken into account we must include the Larmor precession of the nuclear spins. In this case the EOM take the form

$$\dot{\boldsymbol{I}}^{\alpha}_{kd} = \gamma_e b_\alpha\, v_0\, |\psi_{kd}|^2\, \boldsymbol{P}_d \times \boldsymbol{I}^{\alpha}_{kd} - \omega_\alpha\, \hat{z} \times \boldsymbol{I}^{\alpha}_{kd}, \tag{A.12}$$

where α is a species index, $\omega_\alpha = \gamma_\alpha\, B_{\text{ext}} T/\tau_a$ is the effective Larmor frequency, b_α is the bare hyperfine field of species α, γ_α is the gyromagnetic ratio of species α, B_{ext} is the external magnetic field, and we have explicitly included the factor T/τ_a, where T is the total time of the nuclear pump cycle and τ_a is the adiabatic sweep time.

We introduce the projector function π^{α}_{kd}, such that $\pi^{\alpha}_{kd} = 1$ if there is species α in

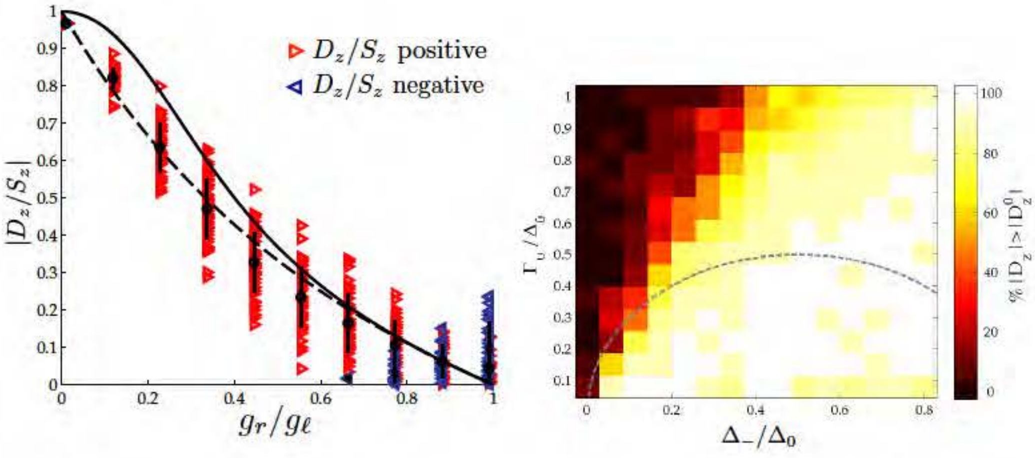

Figure A.1: a) As in Fig. 2.7, with parameters chosen as in Fig. 2 of Gullans et al. (2010), except with three species. Due to the computational cost of running three species of spins, simulations were run for only 10% as long, and the range of D_z/S_z is larger as a result. The trend that D_z/S_z is in good agreement with the single-species prediction is clearly visible. b) Phase diagram with multiple species and $m_0 = 0$.

unit cell k and 0 otherwise. This allows us to write

$$\begin{aligned} \boldsymbol{L} &= \sum_{k,\alpha} \gamma_e b_\alpha v_0 \left|\psi_{k\ell}\right|^2 \pi^\alpha_{k\ell} \boldsymbol{I}^\alpha_{k\ell} \\ &= \frac{\Omega_\ell}{\sqrt{\sum_\alpha b_\alpha^2 x_\alpha}} \sum_{k,\alpha} b_\alpha\, g_{k\ell}\, \pi^\alpha_{k\ell} \boldsymbol{I}^\alpha_{k\ell}. \end{aligned} \tag{A.13}$$

Here we have defined Ω_ℓ to be the standard deviation of L_μ in the infinite temperature state, explicitly

$$\langle \boldsymbol{I}^\alpha_{kd} \cdot \boldsymbol{I}^{\alpha'}_{k'd'} \rangle = I(I+1)\delta_{kk'}\delta_{dd'}\delta_{\alpha\alpha'}, \tag{A.14}$$

$$\Omega_\ell^2 \equiv \left\langle \boldsymbol{L}^2 \right\rangle /3 = \sum_{k,\alpha} \gamma_e^2 b_\alpha^2\, x_\alpha\, v_0^2 \left|\psi_{k\ell}\right|^4 \frac{I(I+1)}{3} \tag{A.15}$$

where $x_\alpha = \langle \pi^\alpha_{kd} \rangle$ is the relative proportion of species α on the sites it can occupy,

$g_{kd} \propto v_0 \left|\psi_{kd}\right|^2$ are chosen to satisfy $\sum_k g_k^2 \, I(I+1) = 3$, and I is the total spin of a single nuclear spin ($I = 3/2$ for all species in GaAs).

We define the variables

$$\boldsymbol{\Phi}_n^\alpha = \frac{1}{\sqrt{x_\alpha}} \sum_k g_{k\ell} \, \varphi_n^\ell(g_{k\ell}) \, \pi_{k\ell}^\alpha \, \boldsymbol{I}_{k\ell}^\alpha, \tag{A.16}$$

where $\varphi_n^\ell(x)$ are defined as in Appendix A.2 and are independent of the species, i.e. $\varphi_0^\ell(x) = 1$ and

$$\sum_k g_{kd}^2 \, \varphi_n^\ell(g_{kd}) \, \varphi_m^\ell(g_{kd}) \, I(I+1) = 3 \, \delta_{nm}. \tag{A.17}$$

These definitions have the implication that $\langle L_{n\,\mu}^\alpha \cdot L_{n'\mu'}^{\alpha'} \rangle = \delta_{nn'}\delta_{\mu\mu'}\delta_{\alpha\alpha'}$, and we can draw initial values for each of them from a normal distribution. Furthermore, we can express

$$\boldsymbol{L} = \frac{\Omega_\ell}{\sqrt{\sum_\alpha b_\alpha^2 \, x_\alpha}} \sum_\alpha b_\alpha \sqrt{x_\alpha} \, \boldsymbol{\Phi}_0^\alpha. \tag{A.18}$$

All these definitions are equivalent for the right dot.

In these variables the EOM take the form

$$\begin{gathered} \dot{\boldsymbol{\Phi}}_n^\alpha = \frac{\gamma_e b_\alpha}{N} \, \boldsymbol{P}_\ell \times \big(\varepsilon_n \boldsymbol{\Phi}_{n-1}^\alpha + \alpha_n \boldsymbol{\Phi}_n^\alpha \\ + \varepsilon_{n+1} \boldsymbol{\Phi}_{n+1}^\alpha \big) - \omega_\alpha \, \hat{z} \times \boldsymbol{\Phi}_n^\alpha, \end{gathered} \tag{A.19}$$

where we have used the definition $N^{-1} = \max_k v_0 \left|\psi_{kd}\right|^2$ to represent the number of nuclear spins with which the electron has significant overlap. For a two dimensional gaussian wave function we have $N = 2/3 \sum_\alpha x_\alpha \gamma_e^2 b_\alpha^2 I(I+1)/\Omega^2$

In Fig. A.1 we include the three nuclear species in the simulation and show that qualitatively the results from the single species case still hold. Fig. A.1a shows the asymptotic ratio of D_z/S_z as the relative dot sizes are varied, where we see good agreement with the simple prediction given in the introduction. In Fig. A.1b we extract the phase diagram in the simplified model with only $\Delta_{0,-}$ and Γ_0 non-zero, as in the model of Gullans et al. (2010). As in the single-spin case, we find a saturation regime at high values of Γ_0/Δ_0 and an instability regime at lower values. Unlike in the single-spin case, the saturation regime does not broaden at higher values of Δ_-/Δ_0. The dashed line is the same as that in Fig. 2.3, showing the simple prediction for the phase boundary with a single species, from (Gullans et al., 2010). The lower-left side of the phase diagram (the region most easily reached in experiments) is well-described by this prediction, even with multiple species.

Appendix B

Appendices to Chapter 3

B.1 Van der Waals Interaction with the Nanosphere

A ground state atom experiences an attractive van der Waals (vdw) force when placed near the sphere due to the virtual emission and reabsorption of photons reflected from the surface (Wylie and Sipe, 1984). This is a purely quantum mechanical effect and can be interpreted as a modification of the Lamb shift due to the presence of the material, which changes the photon density of states. In particular, if we write the atom-photon interaction Hamiltonian as

$$H_I = -\boldsymbol{\mu} \cdot \boldsymbol{E}(\boldsymbol{r}_0) \tag{B.1}$$

where $\boldsymbol{\mu}$ is the dipole operator and $\boldsymbol{E}$ is the electric field, then using second order perturbation theory one can write the energy shift of the ground state as

$$\delta E_a = -\frac{1}{\hbar}\sum_{k,e}\frac{\langle 0|\, E_\alpha\, |k\rangle\, \langle k|\, E_\beta\, |0\rangle\, \langle g|\, \mu_\alpha\, |e\rangle\, \langle e|\, \mu_\beta\, |g\rangle}{\omega_k+\omega_e} \tag{B.2}$$

where $|0\rangle$ refers to the vacuum, $|k\rangle$ to a one-photon state in the kth mode of the system, and $|g, e\rangle$ are the ground and excited states of the atom. Applying Kramers-Kronig relations one can rewrite this as (Wylie and Sipe, 1984)

$$\delta E_a = -\frac{\hbar}{2\pi}\mathrm{Im}\int_0^\infty d\omega\, G_{\alpha\beta}(\boldsymbol{r}_0,\boldsymbol{r}_0;\omega)\alpha_{\alpha\beta}(\omega) = -\frac{\hbar}{2\pi}\int_0^\infty d\xi\, G_{\alpha\beta}(\boldsymbol{r}_0,\boldsymbol{r}_0;i\xi)\alpha_{\alpha\beta}(i\xi) \tag{B.3}$$

We have defined the correlation functions for the electric field and atomic dipole moments

$$G_{\alpha\beta}(\boldsymbol{r},\boldsymbol{r}';t) = i\langle[E_\alpha(\boldsymbol{r},t),E_\beta(\boldsymbol{r}',0)]\rangle\Theta(t)/\hbar \tag{B.4}$$

$$\alpha_{\alpha\beta}(t) = i\,\langle g|\,[\mu_\alpha(t),\mu_\beta(0)]\,|g\rangle\,\Theta(t)/\hbar \tag{B.5}$$

with $\Theta(t)$ is the Heaviside step function. These can be identified with the field and atomic susceptibilities, respectively. The field susceptibility can be obtained from the classical solution for the electric field of an oscillating dipole near the sphere (Wylie and Sipe, 1984). The van der Waals interaction is obtained from the reflected contribution to $G_{\alpha\beta}$. We work in the quasistatic limit where the distance between the atom and sphere is much less than a wavelength. This results in the reflected field of

a dipole $\boldsymbol{p}$ above sphere: $\boldsymbol{E}_r(\boldsymbol{r},\boldsymbol{r}';\omega) = -\nabla(\boldsymbol{p}\cdot\nabla')\Phi_r(\boldsymbol{r},\boldsymbol{r}';\omega)$, where

$$\Phi_r(\boldsymbol{r},\boldsymbol{r}';\omega) = -\frac{1}{4\pi\epsilon_0}\sum_n \frac{\varepsilon(\omega)-1}{\varepsilon(\omega)+1+1/n}\,\frac{a^{2n+1}}{r'^{n+1}\,r^{n+1}}P_n\big(\cos(\theta-\theta')\big) \tag{B.6}$$

ε is the dielectric constant of the sphere, a is the radius, $\boldsymbol{r}'$ is the position of the dipole, and P_n is the nth order Legendre polynomial. The reflected greens function is defined by the relation

$$E_r^\alpha(\boldsymbol{r},\boldsymbol{r}';\omega) = G^r_{\alpha\beta}(\boldsymbol{r},\boldsymbol{r}';\omega)\cdot p_\beta \tag{B.7}$$

$$G_{\alpha\beta}(\boldsymbol{r},\boldsymbol{r}';\omega) = -\nabla_\alpha\nabla'_\beta\Phi_r(\boldsymbol{r},\boldsymbol{r}';\omega) \tag{B.8}$$

The van der Waals force for a ground state atom is dominated by the exchange of low-frequency, off-resonant photons. This is to be contrasted from situation for the excited states, where the atom can emit and reabsorb real photons at the resonance frequency leading to an additional correction to the van der Waals force (Chance et al., 1975). Because of this we are justified in taking $\varepsilon \to -\infty$ in Eq. B.6, which allows us to write

$$G^r_{zz}(\boldsymbol{r},\boldsymbol{r}) = \frac{1}{4\pi\epsilon_0}\frac{a^3}{r^6}\frac{4-3a^2/r^2+a^4/r^4}{(1-a^2/r^2)^3}, \tag{B.9}$$

$$G^r_{xx}(\boldsymbol{r},\boldsymbol{r}) = G^r_{yy}(\boldsymbol{r},\boldsymbol{r}) = \frac{1}{4\pi\epsilon_0}\frac{a^3}{r^6}\frac{1}{(1-a^2/r^2)^3}, \tag{B.10}$$

$$U_{\mathrm{vdW}} = -\frac{C_3}{r^6}\frac{2a^3\big(6-3(a/r)^2+(a/r)^4\big)}{\big(1-(a/r)^2\big)^3} = -\frac{\hbar\gamma}{16\,k_a^3a^3}\frac{2a^6\big(6-3(a/r)^2+(a/r)^4\big)}{r^6\big(1-(a/r)^2\big)^3}, \tag{B.11}$$

$$C_3 = \frac{\hbar}{16\pi^2\epsilon_0}\int_0^\infty d\xi\,\alpha(i\xi) = \frac{\langle\mu^2\rangle}{12}. \tag{B.12}$$

where γ is the spontaneous emission rate for the two-level atom in free space. In the limit $a \ll r$, $U_{\mathrm{vdW}} \sim 1/r^6$, as expected because the sphere responds like a dipole. In the opposite limit, when $(r-a) \ll a$ we reproduce the well known formula for the ground state shift of an atom above a perfectly conducting plane $U_{\mathrm{vdW}} = C_3/(r-a)^3$. For Rb^{87}, $\lambda \sim 780$ nm and $\gamma = 6$ MHz, if we take a sphere with a 20 nm radius this gives the typical scale for $U_{\mathrm{vdW}} \sim 100$ MHz, which is quite substantial.

B.2 Heating Rate from Inelastic Light Scattering

Here we calculate the heating rate due the inelastic light scattering from the trapping laser including the interaction with the nanosphere. Because of the tight trap confinement the change in motional state arises from events where a single phonon is added or subtracted to the system (Grimm et al., 2000). Expanding the fields around the trap center gives the heating rate

$$\Gamma_{\mathrm{jump}} = \Gamma_{\mathrm{tot}} \frac{E'_R}{\hbar \omega_{T,z}} \frac{\Omega^2}{\delta^2}, \tag{B.13}$$

where Ω is the Rabi frequency of the trapping light, δ is the trapping laser detuning from the atomic resonance, $\omega_{T,z}$ is the trap frequency, $E'_R = 9\hbar^2/2m\, z_T^2$ is an enhanced recoil energy due to the tight trap, m is the mass of the atom, and Γ_{tot} is the total spontaneous emission rate of the atom including both radiative emission and non-radiative emission into the surface plasmon modes of the sphere. The lifetime of the trap is approximately given by the time it takes for the atom to hop out of the trap due to such absorption processes

$$t_\ell \sim \frac{\hbar\Omega^2/\delta}{\Gamma_{\text{jump}}\,\hbar\omega_{T,z}} \tag{B.14}$$

We express $\Gamma_{\text{tot}} = \Gamma_{\text{rad}} + \Gamma_{\text{non-rad}}$ in terms of both radiative and non-radiative contributions. The radiative contribution can be found from the dipole moment induced in the sphere from the excited atom

$$\Gamma_{\text{rad}} = \gamma \left|\hat{\mu} + \frac{\alpha(\omega_a)}{4\pi\epsilon_0 z^3}(3(\hat{\mu}\cdot\hat{z})\,\hat{z} - \hat{\mu})\right|^2 \tag{B.15}$$

The non-radiative emission arises from near field coupling of the atom to plasmon modes of the sphere. It can be expressed as $\Gamma_{\text{non-rad}} \propto \text{Im}(\boldsymbol{p}\cdot\boldsymbol{E}_r(\boldsymbol{r}',\boldsymbol{r}'))$, where $\boldsymbol{E}_r$ is the field calculated in Eq. B.6. $\Gamma_{\text{non-rad}}$ contains both a resonant and non-resonant contributions from the dipole and multipole contributions, respectively

$$\frac{\Gamma_{\text{non-rad}}}{\Gamma_0} = \frac{6\,a^3}{k_a^3\,r^6}\frac{\text{Im}\big(\alpha(\omega_a)\big)}{4\pi\epsilon_0\,a^3} + \frac{3}{2}\frac{1}{k_a^3 a^3}\text{Im}\left(\frac{\varepsilon-1}{\varepsilon+1}\right)\frac{a^8\,(9-11(a/r)^2+4(a/r)^4)}{r^8\left(1-(a/r)^2\right)^3} \tag{B.16}$$

For moderate distances from the sphere we see that $\Gamma_{\text{non-rad}}$ is dominated by the emission into the resonant surface plasmon mode. In addition, this emission can be substantially greater than the radiative emission.

B.3 Tuning the Lattice Potential

In order to control the tunneling rate in the Hubbard model, one needs control over the trapping potential in the plane of the lattice. This can be achieved through

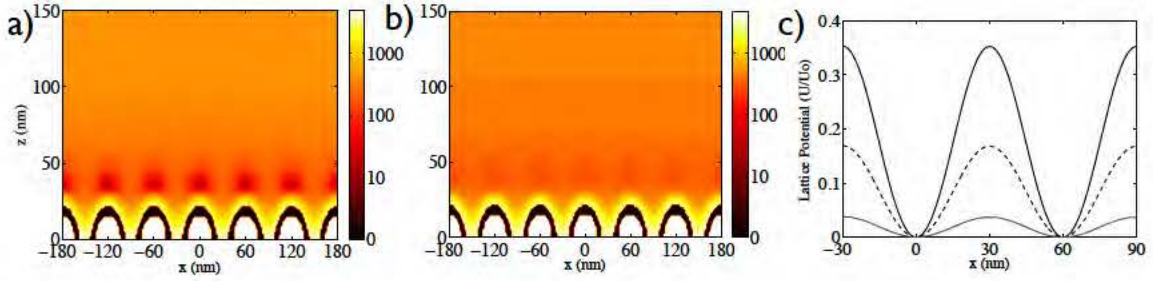

Figure B.1: a-b) Contours of atomic potential in MHz for a 1D chain of silver nanoshells including vdw with light blue-detuned to the plasmon resonance, linear polarized light is applied from the side and circularly polarized light is applied from above. The lattice potential can be tuned by changing the polarization between linear and circular: $U_z/U_0 = 1$ in (a), while $U_z/U_0 = 0.75$ in (b). c) Lattice potential along the chain for different amounts of circular polariztion: $U_z/U_0 = 1$ (solid), $U_z/U_0 = 0.75$ (dashed), and $U_z/U_0 = 0.5$ (grey).

polarization control similarly to the loading procedure. Figure B.4 demonstrates this tuning in a lattice formed by linearly polarized light. Here adding circularly polarized light lowers the potential in the plane of the lattice, while simultaneously maintaining the trap in the vertical direction.

B.4 Effective Scattering Length in Tight Traps

The scattering problem for two atoms in a three-dimensional isotropic trap interacting via a contact potential can be solved exactly. We follow the approach as described by Busch et al. (1998) and Bolda et al. (2002) and define an energy dependent effective scattering length as $a_{eff}(E) = -\tan\eta_0(k)/k$. We find the eigenvalues of the system by solving:

$$\frac{a_{eff}(E)}{l} = f(E) \tag{B.17}$$

where $l = \sqrt{\hbar/m\omega}$ is the harmonic oscillator groundstate length and the so called 'intercept' function $f(E)$ is defined as:

$$f(E) = \frac{1}{2}\tan\left(\frac{\pi E}{2\hbar\omega} + \frac{\pi}{4}\right)\frac{\Gamma(\frac{E}{2\hbar\omega} + \frac{1}{4})}{\Gamma(\frac{E}{2\hbar\omega} + \frac{3}{4})}$$

We calculate the effective scattering length by using the accumulated phase method as described by (Verhaar et al., 2009); we solve the radial Schrodinger equation between $r = a_{in} = 20\,\mathrm{a}_0$ and $r \to \infty$ where we apply the known scattering length as a boundary condition at $r \to \infty$, this gives us the phase of the wavefunction at $r = a_{in}$. Subsequently we calculate the effective scattering length as a function of energy E by using the phase at $r = a_{in}$ as the boundary condition. We assume the accumulated phase is energy independent over the energy range we consider. This results in an energy dependent scattering length. We verified the validity of the accumulated phase method by comparing to the results for ^{23}Na obtained by Bolda, et. al. and find good agreement (Bolda et al., 2002). The approach breaks down if the harmonic oscillator length becomes smaller than the van der Waals range ($l < r_{vdW}$) which is defined as $r_{vdW} = \frac{1}{2}\left(2\mu C_6/\hbar^2\right)^{1/4}$. For ^{87}Rb this implies the trapping frequency should be less than 12 MHz.

Figure B.4 shows the results of this calculation for ^{87}Rb with a 1 MHz trapping frequency. We took a triplet scattering length of $a_T = 98.99a_0$ and $C_6 = 4698a_0$ (van Kempen et al., 2002). For these parameters we find a resonance in the effective scattering length near $E \simeq h \times 9.5\,\mathrm{MHz} \simeq \mathrm{k_B}{\times}450\,\mu\mathrm{K}$, which is between the 4th and the 5th vibrational state. In the inset to Figure 3.2 we show the effective scattering length for the lowest vibrational level as a function of trap frequency where we see a

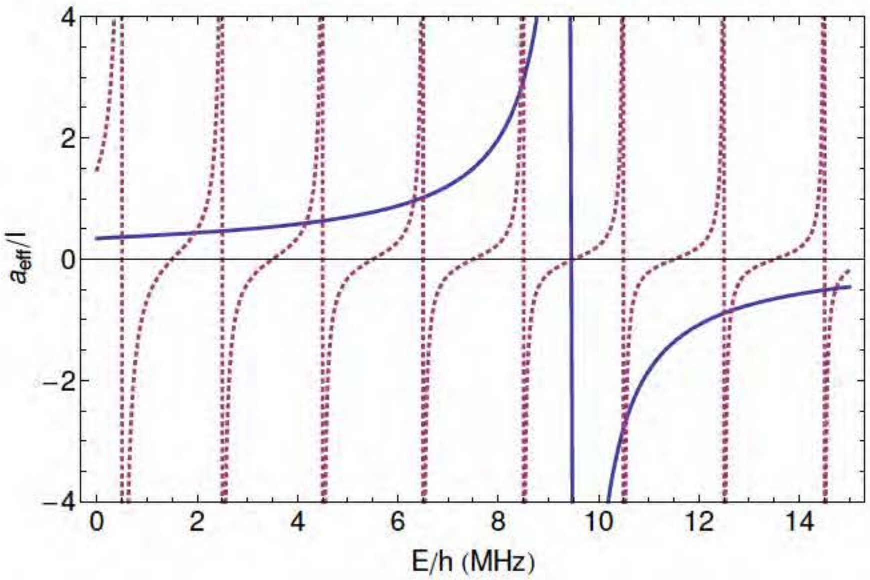

Figure B.2: The effective scattering length (blue solid curve) and the intercept function (red dashed curve) for a trap frequency of $\omega = 1\,\mathrm{MHz}$. The eigenvalues of this system correspond to the crossings of the two curves.

resonance at $\omega \simeq 3.8$ MHz.

This scattering problem will be also affected by the sphere because it modifies the vdw interaction between the atoms. However, the spheres contribution will be small compared the bare vdw, provided the typical distance between the atoms on a single site is much less than their distance to the sphere.

B.5 Two Atom Entanglement on the Lattice

For two atoms on sites 0 and n we take the density matrix evolution

$$H = \Delta(\sigma^1_{ee} + \sigma^2_{ee}) + \Omega(\sigma^1_{eg} - \sigma^2_{eg} + h.c.) + B_x(\sigma^1_{gs} + \sigma^2_{gs} + h.c.) \tag{B.18}$$

$$\dot{\rho} = -i\,[H, \rho] - \gamma_{0n}\mathcal{D}[\sigma^1_{ge} + \sigma^2_{ge}]\rho - \delta\gamma_n\big(\mathcal{D}[\sigma^1_{ge}] + \mathcal{D}[\sigma^2_{ge}] + \mathcal{D}[\sigma^1_{se}] + \mathcal{D}[\sigma^2_{se}]\big)\rho \tag{B.19}$$

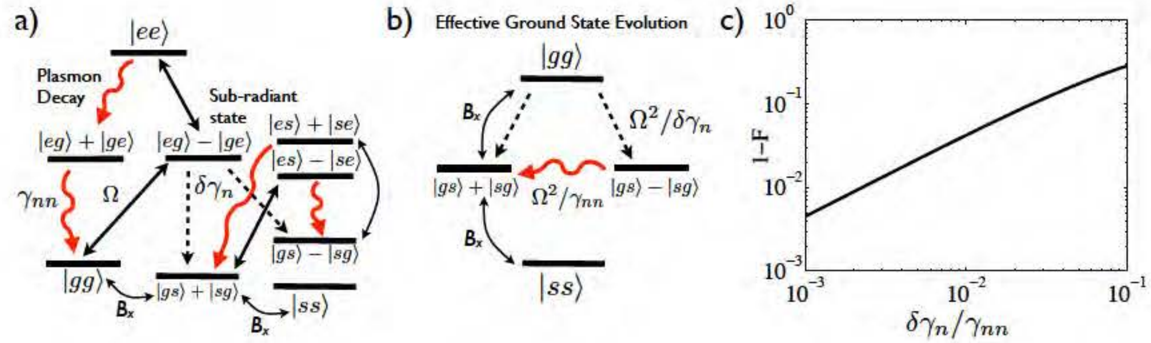
a)
$|ee\rangle$
Plasmon Decay
Sub-radiant state
$|eg\rangle + |ge\rangle$
$|eg\rangle - |ge\rangle$
$|es\rangle + |se\rangle$
$|es\rangle - |se\rangle$
γ_{nn}
Ω
$\delta\gamma_n$
$|gs\rangle - |sg\rangle$
$|gg\rangle$
$|gs\rangle + |sg\rangle$
$|ss\rangle$
B_x
B_x
b) Effective Ground State Evolution
$|gg\rangle$
B_x
$\Omega^2/\delta\gamma_n$
$|gs\rangle + |sg\rangle$
Ω^2/γ_{nn}
$|gs\rangle - |sg\rangle$
B_x
$|ss\rangle$
c)
1-F
10^0
10^{-1}
10^{-2}
10^{-3}
10^{-3}
10^{-2}
10^{-1}
$\delta\gamma_n/\gamma_{nn}$

Figure B.3: a) Level diagram for two atoms showing transitions driven by external fields and decay pathways. b) Level diagram showing effective transition rates in the ground state manifold. The pumping rate into the state $|sg\rangle - |gs\rangle$ is much larger than the rate out of it. c) Shows the infidelity for preparing the singlet state after optimizing B_x and Ω as the sub-radiant states linewidth becomes narrower.

where Δ is the detuning between the control fields and the excited state, Ω is an optical control field, B_x is a transverse ground state magnetic field, and $D[c]\rho = 1/2\{c^\dagger c, \rho\} - c\rho c^\dagger$. In addition to the decay from $|e\rangle$ to $|g\rangle$ through the plasmons we assume there is an additional decay from $|e\rangle$ to $|s\rangle$ that occurs at the rate $\delta\gamma_n$. This term is essential to remove entropy from the system to cool into the singlet state. The relevant process are shown schematically in Fig. B.5a.

The minimal error in preparing the singlet state decreases linearly with the ratio $\delta\gamma_n/\gamma_{nn}$ as shown in Fig. B.5c. This can be understood in the limit of weak driving $\Omega \ll \delta\gamma_n \ll \gamma_{nn}$. In this limit the excited states can be adiabatically eliminated to give the effective evolution depicted in Fig. B.5b. Because the optical pumping rate out of a state increases inversely with the linewidth, the pumping rate into the singlet state $R_{in} \approx \Omega^2/\delta\gamma_n$ can be much larger than the pumping rate out of it $R_{out} \approx \Omega^2/\gamma_{nn}$. If, in addition, $B_x \gg \Omega^2/\delta\gamma_n$ the triplet states are completely mixed and all triplet states can be optically pumped into the singlet state. The ratio $R_{out}/R_{in} \sim \delta\gamma_n/\gamma_{nn}$ then determines the relative population in the triplets to the singlet state, giving the fidelity $F \approx 1 - \delta\gamma_n/\gamma_{nn}$.

As a remark we note that Eqs. 16 and 17 can be mapped exactly to a cavity QED model by replacing γ_{0n} by g^2/κ and $\delta\gamma_n$ by γ, where g is the coupling of a single atom to a single cavity photon, κ is the cavity decay rate, and γ is the free space decay rate. In this case the fidelity scales as $1 - 1/P$ where $P = g^2/\kappa\gamma$ is the Purcell factor. This linear scaling of the singlet fidelity with the Purcell factor agrees with the limit obtained by Kastoryano et al. (2011) using a similar dissipative approach. The main difference between the two schemes is that for the scheme by Kastoryano et al. (2011), the cavity resonance is assumed to be far detuned from the atomic resonance, while in the present approach the two resonances are the same. Thus they operate in qualitatively different regimes of cavity QED. In the off resonance case the cavity interaction shifts the excited state energies for the states $|eg\rangle \pm |ge\rangle$, while in the resonant case the cavity interaction results in different linewidths for $|eg\rangle \pm |ge\rangle$. Clearly either phenomenon is sufficient for ground state entanglement generation.

Appendix C

Appendices to Chapter 4

C.1 Nonlinear Conductivity

The nonlinearity can be derived from the Boltzmann equation for the 2D electron distribution function $f(\boldsymbol{x}, \boldsymbol{k}, t)$ and Poisson's equation for the electric potential $\varphi(\boldsymbol{x}, z, t)$

$$\partial_t f + v_F \hat{k} \cdot \partial_{\boldsymbol{x}} f + e \partial_{\boldsymbol{x}} \varphi \cdot \partial_{\boldsymbol{k}} f = 0 \tag{C.1}$$

$$(\partial_{\boldsymbol{x}}^2 + \partial_z^2)\varphi = e\, n\, \delta(z)/\epsilon_0 \varepsilon \tag{C.2}$$

where $n = \int d\boldsymbol{k} f$ is the 2D electron density $\partial_{\boldsymbol{x}} = \partial_x \hat{x} + \partial_y \hat{y}$ and $\partial_{\boldsymbol{k}} = \partial_{k_x} \hat{x} + \partial_{k_y} \hat{y}$. Taking x to be the propagation direction the nonlinear equations for the moments n

and $n\,\bar{\boldsymbol{v}} = \int d\boldsymbol{k}\, v_F \hat{k}\, f$ can be derived as

$$\partial_t n + \partial_x n\,\bar{v} = 0 \tag{C.3}$$

$$\partial_t \bar{v} - \frac{e}{m^*}\partial_x\varphi + \bar{v}\,\partial_x\bar{v} + \frac{3e}{2m^* n_0}\partial_x\varphi\,\delta n = 0 \tag{C.4}$$

where the effective mass for the plasmon excitations is $m^* = \hbar k_F/v_F$, $\delta n = n - n_0$ and $n_0 \equiv k_F^2/\pi$ is the equilibrium electron density. Linearizing these equations around n_0 and $\bar{v} = 0$ gives the plasmon dispersion from Eq. 1 (Fetter, 1973). The nonlinearity is described by the last two terms into Eq. C.4, where the second term $\propto \partial\varphi\delta n$ arises from the linear band structure in graphene and is absent for electrons with a parabolic dispersion. To find the nonlinear conductivity we can expand $\bar{v}$ and n in spatial Fourier components and solve the resulting coupled equations combined with Poisson's equation (Denardo and Putterman, 1988). This allows us to express $\sigma^3(\omega)$ through the identity $en\bar{v} = \sigma(\omega)E + \sigma^3(\omega)E^3$.

To solve for the nonlinear shift in the cavity we use the boundary condition that $\bar{\boldsymbol{v}} \cdot \hat{n} = 0$. This allows us to represent $\bar{\boldsymbol{v}} = \hat{x}\sum_p v_p \sin px$ and $n = \sum_q n_q \cos qx$ where $q = mk_{sp}$ for some integer m. Inserting this solution into Eq. C.3-C.4 leads to coupled nonlinear equations for n_q and v_q

$$\begin{aligned}\sum_p \sin px\left(\dot{v}_p - \frac{\omega_p^2}{n_0 p}n_p\right) &= \frac{1}{2}\sum_{p,q}[pv_pv_q\sin(p-q)x \\ &- \left(pv_pv_q - \frac{3}{2}\frac{\omega_p^2}{p}\frac{n_pn_q}{n_0^2}\right)\sin(p+q)x] \qquad \text{(C.5)}\\ \sum_p \cos px(\dot{n}_p + n_0pv_p) &= \frac{1}{2}\sum_{p,q} n_pv_q\big[(p-q)\cos(p-q)x - \quad (p+q)\cos(p+q)x\big]\end{aligned}$$

where ω_p is given by Eq. 1. These equations can be solved in perturbation theory to find the nonlinear frequency shift of the plasmon resonance given in Eq. 4.

C.2 Quantizing the Plasmon Mode

To quantize the plasmon mode we use the Hamiltonian (Gervasoni and Arista, 2003)

$$
\begin{aligned}
H &= \frac{1}{2}\int d\boldsymbol{x}\, e\,\delta n\,\varphi + \frac{1}{2}\int d\boldsymbol{x} n_0 m^* \bar{v}^2 \\
&= \frac{A\,m^*}{4\,n_0}\sum_q \frac{1}{q^2}(\omega_q^2\,\delta n_q^2 + \delta\dot{n}_q^2)
\end{aligned}
\tag{C.6}
$$

where $A = \pi^2/k_{sp}^2$ is the area of the sheet and we used the relation $\bar{v}_q = -\delta\dot{n}_q/q\,n_0$ from the continuity equation. This Hamiltonian can be quantized in the usual way by defining $\delta n_q = \frac{\gamma_q}{2\omega_q}(a_q + a_q^\dagger)$ for bosonic operators a_q such that $\dot{a}_q = -i\omega_q a_q$ and $\gamma_q = 2q\sqrt{\omega_q\omega_F/\pi A}$. This leads directly to Eq. 4.

C.3 Coupling between Nanoribbon and Cavity

To calculate the coupling between the cavity and the proximal nanoribbion we use the electric potential of the nanoribbon plasmons acting on the graphene cavity

$$
\begin{aligned}
\varphi_r(x) &= \frac{1}{4\pi\epsilon_0\varepsilon}\sum_k \int d\boldsymbol{x}' \frac{e\,n_k^r\,\cos kx'}{|x+d-x'|} \\
&\approx \frac{W_r}{4\pi\epsilon_0\varepsilon}\sum_k \frac{e\,n_k^r}{k^2(x+d)^2}
\end{aligned}
\tag{C.7}
$$

where we assumed $d \gg W, \lambda_{sp}$. Inserting this into . Eq. C.4 gives the coupling between each plasmon mode k in the nanoribbon with the plasmon mode q of the cavity as

$$\kappa_{kq} = \frac{8}{\pi}\sqrt{\frac{k_F^r\, W_r}{k_F^c L}}\frac{{\omega_q^c}^2}{\omega_k^r + \omega_q^c}\frac{1}{q^2 k\, d^3} \tag{C.8}$$

where L is the length of the nanoribbon, $k_F^{r,c}$ is the Fermi wavevector and $\omega_k^{r,c}$ is the dispersion of the ribbon(r) and cavity(c). Applying Fermi's Golden rule gives the decay rate of the cavity mode into the nanoribbon plasmons given in Eq. 8.

Appendix D

Appendices to Chapter 6

D.1 Numerical Code for Two-Photon Time Dependent Dynamics

Here we show the numerical MATLAB code we wrote for time dependent dynamics of 2 photons.

```
%%% Evolves two photon-atom wavefunction in time including Rydberg
%%% interactions
%%% Variables:
%%% PhotIn_x - Input photon wavefunction is a function of space x and integer time
%%% WF1a - WF in region with 1 photon in the medium and one behind
%%% pWF1ab - photon WF at boundary of region with 1 phot out and 1 phot at
%%%          start of the medium
%%% WF2 - WF inside medium composed of 3 level Rydberg atoms
%%% RydV - Flag which says whether or not there are interactions
%%% RydInd - Pairs of coord separ. by Ryd blockade for square potential
%%% u2RightB - Boundary WF for region with 1 phot out and 1 phot in
%%% u2upperB - Boundary WF for region with 1 phot out and 1 phot at start
%%%            of medium
%%% Uevolx1 - Evolution operator e^{-i HatomPhot delt}
%%% Uevolx2 - Tensor product of Uevolx1 with itself
```

```
for m=1:Nt
    % Update WF in region with 1 phot in medium and 1 behind
    WF1a(1,:)=circshift(WF1a(1,:),[0,nshift]);
    WF1a(1,1:nshift)=PhotIn_x(0,m);
    WF1a=Uevolx1*WF1a;
    %%%%%%%%
    % Record output at boundary of region with 1 phot out and 1 phot at
    % start of the medium
    pWF1aB=circshift(pWF1aB,-1);
    pWF1aB(end)=WF1a(1,end);
    %%%%%%%%%
    % Include second photon to get two photon WF
    WF1aB=PhotIn_x(0,m).*WF1a;
    %%%%%%%%%
    % Update two photon WF with both photons in medium
    WF2(1,:,:)=circshift(WF2(1,:,:),[0 nshift nshift]);
    WF2(2,:,:)=circshift(WF2(2,:,:),[0 nshift 0]);
    WF2(3,:,:)=circshift(WF2(3,:,:),[0 nshift 0]);
    WF2(1:3,1,:)=WF1aB;
    WF2(4,:,:)=squeeze(WF2(2,:,:)).';
    WF2(7,:,:)=squeeze(WF2(3,:,:)).';
    WF2(1,:,1)=WF2(1,1,:);
    % etprod is an external function for multidimensional tensor products
    % Can be found online
    WF2=etprod('a12',Uevolx2,'ab',WF2,'b12');
    % Include Rydberg interaction
    if RydV~=0
        WF2(9,RydInd)=0;
    end
    %%%%%%%%%
    % Extract boundary conditions for exiting the medium
    u2rightB=WF2([1 4 7],:,end);
    %%%%%%%%
    % Update WF in region with 1 phot out and 1 phot in medium
    WF2b(1,:,:)=circshift(WF2b(1,:,:),[0 1 1]);
    WF2b(2,:,:)=circshift(WF2b(2,:,:),[0 0 1]);
    WF2b(3,:,:)=circshift(WF2b(3,:,:),[0 0 1]);

    u2upperB=zeros(1,Nb);
    u2upperB(1:min(m,Nb))=fliplr(pWF1aB(1:min(m,Nb))).*PhotIn_x(0,m);
    WF2b(2,1,:)=PhotIn_x(0,m).*WF1a(2,end);
    WF2b(3,1,:)=PhotIn_x(0,m).*WF1a(3,end);
    WF2b(1,1,:)=u2upperB;
    WF2b(:,:,1)=u2rightB;

    WF2b=etprod('a12',Uevolx1,'ab',WF2b,'b12');
    %%%%%%%%%%%%
    % Save ouptut by recording values for WF2b(1,end,:)
 end
```

D.2 Numerical Code for Three-Photon Steady State Solution

Here we show the numerical MATLAB code we wrote for steady state solutions of up to three photons.

```
%%% Finds wavefunction (WF) in steady state for three photons incident on
%%% the medium
%%% Variables:
%%% WF2-5 - WF in regions 2-5, 4B, and 5B defined below
%%% eitR - Ratio of amplitude between S and E state for dark state
%%%        polariton
%%% alpha - Initial amplitude of coherent state input
%%% Natoms - Number of atoms
%%% Nmeas - Number of grid points taken past the medium where photons are
%%%         measured
%%% RydInd - Pairs of coord separ. by Ryd blockade for square potential


%%% 2 photons in 1 behind
%%% [EEE;EES;ESE;ESS];
WF2=zeros(4,Natoms,Natoms);

%%% 3 photons in
%%% [EEE;EES;ESE;ESS;SEE;SES;SSE;SSS];
WF3=(zeros(8,Natoms,Natoms,Natoms));
```

```
%%% 2 photons in 1 out
%%% [EEE;EES;ESE;ESS;SEE;SES;SSE;SSS];
WF4=(zeros(8,Natoms,Natoms,Nmeas));

%%% 1 photon in 2 out
%%% [EEE;SEE];
WF5=(zeros(2,Natoms,Nmeas,Nmeas));

%%% 1 photons in 1 out 1 behind
%%% [EEE;EES;ESE;ESS];
WF4B=zeros(4,Natoms,Nmeas);

%%% 2 photons out 1 behind
%%% EEE
WF5B=zeros(4,Nmeas,Nmeas);

%%% Parameters governing solution in region 1 with 1 photon in and 2 behind
eitR=-gc/Omega;
alpha=1;

%%%%%%% Region 2 %%%%%%%%%

%%% Initial conditions
WF2(1,1,:)=alpha^3;
WF2(1,:,1)=alpha^3;
WF2(2,1,:)=eitR*alpha^3;
WF2(3,:,1)=eitR*alpha^3;
WF2(4,1,1)=eitR/2.*(WF2(2,1,1)+WF2(3,1,1));
WF2(4,RydInd)=0;

%%% Update WF in region 2
for L=1:Natoms
    if L>1
        %%% EEE has 3 spatial derivatives so we use value from all three
        %%% one behind, similarly EES and ESE have 2 spatial derivatives
        %%% and ESS has one.
        WF2(1,L,2:end)=WF2(1,L-1,1:end-1)+delt.* ...
            etprod('a12',HamEffx2(1,:),'ab',WF2(:,L-1,1:end-1),'b12');
        WF2(2,L,2:end)=WF2(2,L-1,2:end)+delt.* ...
            etprod('a12',HamEffx2(2,:),'ab',WF2(:,L-1,2:end),'b12');
        WF2(2,L,1)=WF2(3,1,L);
    end
    for k=1:Natoms
        if k>1
            WF2(3,L,k)=WF2(3,L,k-1)+delt.* ...
                etprod(’a12’,HamEffx2(3,:),’ab’,WF2(:,L,k-1),’b12’);
        end
        if  RydInd(L,k)==0
            WF2(4,L,k)=eitR.*(WF2(2,L,k)+WF2(3,L,k))/2;
        end
    end
end

%%%%%%% Region 4B %%%%%%%%%%
%%% Use WF2 to get boundary condition for region 4 with 2 in 1 out.
%%% Initial conditions
WF4B(:,:,1)=WF2(:,:,end);
WF4B(1,1,:)=alpha^3;
WF4B(2,1,:)=WF4B(2,1,1);
for L=1:Natoms
    if L>1
        WF4B(3,1,L)=WF4B(3,1,L-1) + delt.* ...
            HamEffx2(2,:)*squeeze(WF4B(:,1,L-1));
    end
    WF4B(4,1,L)=eitR.*(WF4B(2,1,L)+WF4B(3,1,L))/2;
end
%%% Full WF
for L=2:Nmeas


    WF4B(1,2:end,L)=WF4B(1,1:end-1,L-1) ...
        + delt.*HamEffx2(1,:)*squeeze(WF4B(:,1:end-1,L-1));
    WF4B(3,:,L)=WF4B(3,:,L-1) ...
        + delt.*HamEffx2(3,:)*squeeze(WF4B(:,:,L-1));
    for k=1:Natoms
        if k>1
            WF4B(2,k,L)=WF4B(2,k-1,L) + delt.* ...
                HamEffx2(2,:)*squeeze(WF4B(:,k-1,L));
        end
        WF4B(4,k,L)=eitR.*(WF4B(2,k,L)+WF4B(3,k,L))/2;
    end

end
```

```
%%%%%%% Region 5B %%%%%%%%%%

%%% Find BC for region 5 with 2 out and 1 in from region 4B
%%% Initial conditions
WF5B(:,1,:)=WF4B(:,end,:);
WF5B(1,:,1)=WF5B(1,1,:);
WF5B(2,:,1)=WF5B(3,1,:);
WF5B(3,:,1)=WF5B(2,1,:);
WF5B(4,:,:)=eitR*(WF5B(2,:,:)+WF5B(3,:,:))/2;

for L=2:Nmeas
    WF5B(1,L,L:end)=WF5B(1,L-1,L-1:end-1);
    WF5B(1,L:end,L)=WF5B(1,L,L:end);
end

%%%%%%% Region 3 %%%%%%%%%%

%%% Initial conditions
WF3(1:4,1,:,:)=WF2;
WF3(2,:,1,:)=WF2(2,:,:);
WF3(3,:,:,1)=WF2(2,:,:);
WF3(1,:,1,:)=WF2(1,:,:);
WF3(1,:,:,1)=WF2(1,:,:);
WF3(5,:,1,:)=squeeze(WF3(3,1,:,:));
WF3(5,:,:,1)=squeeze(WF3(3,1,:,:));
WF3(6,:,1,:)=squeeze(WF3(4,1,:,:));
WF3(7,:,:,1)=squeeze(WF3(4,1,:,:));
%%% SSS has no spatial derivatives so steady state solution can be derived
WF3(8,1,1,1)=eitR/3.*sum(squeeze(WF3([4 6 7],1,1,1)));
WF3(8,RydInd123)=0;
WF3(4,RydInd23)=0;
WF3(7,RydInd12)=0;
WF3(6,RydInd13)=0;

%%% Initial conditions
for k=1:Natoms
    for m=1:Natoms
        if  m>1 && RydInd12(1,k,m)==0
            WF3(7,1,k,m)=WF3(7,1,k,m-1)...
                +delt.*HamEffx3(7,:)*squeeze(WF3(:,1,k,m-1));
        end
        if k>1
            if RydInd13(1,k,m)==0
                WF3(6,1,k,m)=WF3(6,1,k-1,m)...
                    +delt.*HamEffx3(6,:)*squeeze(WF3(:,1,k-1,m));
            end
            if m>1
                WF3(5,1,k,m)=WF3(5,1,k-1,m-1)...
                    +delt.*HamEffx3(5,:)*squeeze(WF3(:,1,k-1,m-1));
            end
        end

        if RydInd123(1,k,m) == 0
            WF3(8,1,k,m)=eitR/3.*sum(squeeze(WF3([4 6 7],1,k,m)));
        end
    end
end
%%% Initial conditions
WF3(2,:,:,1)=squeeze(WF3(5,1,:,:));
WF3(3,:,1,:)=squeeze(WF3(5,1,:,:));
WF3(4,:,:,1)=squeeze(WF3(6,1,:,:));
WF3(4,:,1,:)=squeeze(WF3(4,:,:,1));
WF3(6,:,:,1)=squeeze(WF3(7,1,:,:));
WF3(7,:,1,:)=squeeze(WF3(7,1,:,:));
WF3(8,:,:,1)=squeeze(WF3(8,1,:,:));
WF3(8,:,1,:)=squeeze(WF3(8,1,:,:));

%%% Find full WF taking into account when 2 phot are within a blockade
%%% Could be made much faster with more efficient matrix representation
%%% or by writing in c and using mex

for L=2:Natoms
    for k=2:Natoms
        for m=2:Natoms
            WF3(2,L,k,m)=WF3(2,L-1,k-1,m) ...
                +delt.*HamEffx3(2,:)*squeeze(WF3(:,L-1,k-1,m));
            if RydInd13(L,k,m)==0
                WF3(6,L,k,m)=WF3(6,L,k-1,m)...
                    +delt.*HamEffx3(6,:)*squeeze(WF3(:,L,k-1,m));
            end
            WF3(1,L,k,m)=WF3(1,L-1,k-1,m-1)...
                +delt.*HamEffx3(1,:)*squeeze(WF3(:,L-1,k-1,m-1));
            WF3(5,L,k,m)=WF3(5,L,k-1,m-1)...
```

```
                +delt.*HamEffx3(5,:)*squeeze(WF3(:,L,k-1,m-1));
            if RydInd23(L,k,m)==0
                WF3(4,L,k,m)=WF3(4,L-1,k,m)...
                    +delt.*HamEffx3(4,:)*squeeze(WF3(:,L-1,k,m));
            end
            WF3(3,L,k,m)=WF3(3,L-1,k,m-1) ...
                +delt.*HamEffx3(3,:)*squeeze(WF3(:,L-1,k,m-1));
            if RydInd12(L,k,m)==0
                WF3(7,L,k,m)=WF3(7,L,k,m-1)...
                    +delt.*HamEffx3(7,:)*squeeze(WF3(:,L,k,m-1));

            end
            if RydInd123(L,k,m) == 0
                WF3(8,L,k,m)=eitR/3.*sum(squeeze(WF3([4 6 7],L,k,m)));
            end
        end
    end
end

%%%%%%% Region 4 %%%%%%%%%

%%% Initial conditions
WF4(:,:,:,1)=WF3(:,:,:,end);
WF4(1,1,:,:)=WF4B(1,:,:);
WF4(1,:,1,:)=WF4B(1,:,:);
WF4(2,1,:,:)=WF4B(2,:,:);
WF4(2,:,1,:)=WF4B(2,:,:);
WF4(3,1,:,:)=WF4B(3,:,:);
WF4(4,1,:,:)=WF4B(4,:,:);
WF4(5,:,1,:)=WF4B(3,:,:);
WF4(6,:,1,:)=WF4(4,1,:,:);
%%% Initial conditions
for L=1:Natoms
    for m=2:Nmeas
        if L>1
            WF4(3,L,1,m)=WF4(3,L-1,1,m-1) ...
                +delt.*HamEffx3(3,:)*squeeze(WF4(:,L-1,1,m-1));
            WF4(4,L,1,m)=WF4(4,L-1,1,m)...
                +delt.*HamEffx3(4,:)*squeeze(WF4(:,L-1,1,m));


        end
        if RydInd(L,1)==0
            WF4(7,L,1,m)=WF4(7,L,1,m-1) + delt.* ...
                HamEffx3(7,:)*squeeze(WF4(:,L,1,m-1));
            WF4(8,L,1,m)=eitR/3.*sum(squeeze(WF4([4 6 7],L,1,m)));
        end
    end
end
%%% Initial conditions
WF4(7,1,:,:)=WF4(7,:,1,:);
%%% Initial conditions
for k=2:Natoms
    for m=2:Nmeas

        WF4(6,1,k,m)=WF4(6,1,k-1,m)...
            +delt.*HamEffx3(6,:)*squeeze(WF4(:,1,k-1,m));
        WF4(5,1,k,m)=WF4(5,1,k-1,m-1)...
            +delt.*HamEffx3(5,:)*squeeze(WF4(:,1,k-1,m-1));


        if RydInd(1,k)==0
            WF4(7,1,k,m)=WF4(7,1,k,m-1)...
                +delt.*HamEffx3(7,:)*squeeze(WF4(:,1,k,m-1));

        end
        if RydInd(1,k) == 0
            WF4(8,1,k,m)=eitR/3.*sum(squeeze(WF4([4 6 7],1,k,m)));
        end
    end
end
%%% Full WF
for L=2:Natoms

    for k = 2:Natoms
        for m=2:Nmeas
            WF4(2,L,k,m)=WF4(2,L-1,k-1,m) ...
                +delt.*HamEffx3(2,:)*squeeze(WF4(:,L-1,k-1,m));

            WF4(6,L,k,m)=WF4(6,L,k-1,m)...
                +delt.*HamEffx3(6,:)*squeeze(WF4(:,L,k-1,m));


            WF4(1,L,k,m)=WF4(1,L-1,k-1,m-1)...
```

```
                +delt.*HamEffx3(1,:)*squeeze(WF4(:,L-1,k-1,m-1));
            WF4(5,L,k,m)=WF4(5,L,k-1,m-1)...
                +delt.*HamEffx3(5,:)*squeeze(WF4(:,L,k-1,m-1));

            WF4(4,L,k,m)=WF4(4,L-1,k,m)...
                +delt.*HamEffx3(4,:)*squeeze(WF4(:,L-1,k,m));

            WF4(3,L,k,m)=WF4(3,L-1,k,m-1) ...
                +delt.*HamEffx3(3,:)*squeeze(WF4(:,L-1,k,m-1));
            if RydInd(L,k)==0
                WF4(7,L,k,m)=WF4(7,L,k,m-1)...
                    +delt.*HamEffx3(7,:)*squeeze(WF4(:,L,k,m-1));

            end
            if RydInd(L,k) == 0
                WF4(8,L,k,m)=eitR/3.*sum(squeeze(WF4([4 6 7],L,k,m)));
            end

        end
    end
end
%%%%%% Region 5 %%%%%%%%%

%%% Initial conditions
WF5(1,:,1,:)=WF4(1,:,end,:);
WF5(2,:,1,:)=WF4(5,:,end,:);
WF5(1,:,:,1)=WF5(1,:,1,:);
WF5(2,:,:,1)=WF5(2,:,1,:);
WF5(1,1,:,:)=WF5B(1,:,:);
for k=2:Nmeas
    for m=2:Nmeas
        WF5(2,1,k,m)=WF5(2,1,k-1,m-1)+delt.*...
            HamEff(2,:)*squeeze(WF5(:,1,k-1,m-1));
    end
end
tmp=squeeze(WF5(:,:,1,:));
for k=0:Nmeas-2
    WF5diagk=zeros(2,Natoms,(Nmeas-k));
    tmp=squeeze(WF5(:,:,1,k+1));
    for m=2:(Nmeas-k)
        for mm=1:round(c/vg)
            tmptmp=tmp;
            tmp(1,2:end)=tmptmp(1,1:end-1)+delt.*...
                HamEff(1,:)*tmptmp(:,1:end-1);
            tmp(2,2:end)=tmptmp(2,2:end)+delt.*...
                HamEff(2,:)*tmptmp(:,2:end);
        end
        WF5diagk(:,:,m)=tmp;
    end
    for L=2:Natoms
        WF5(1,L,:,:)=squeeze(WF5(1,L,:,:))+diag(squeeze(WF5diagk(1,L,:)),k);
        WF5(2,L,:,:)=squeeze(WF5(2,L,:,:))+diag(squeeze(WF5diagk(2,L,:)),k);
    end
end
for L=2:Natoms
    WF5(1,L,:,:)=squeeze(WF5(1,L,:,:))+squeeze(WF5(1,L,:,:)).’-diag(diag(squeeze(W
end
for k=2:Nmeas
    tmptmp=tmp;
    for L=2:Natoms
        tmp(1,L,k:end)=squeeze(tmptmp(1,L-1,(k-1):(end-1)))+...
            (delt.*HamEff(1,:)*squeeze(tmptmp(:,L-1,(k-1):end-1))).’;
        tmp(2,L,k:end)=squeeze(tmptmp(2,L,(k-1):end-1))+ ...
            (delt*HamEff(2,:)*squeeze(tmptmp(:,L,(k-1):end-1))).’;

    end
    WF5(1,2:end,k,k:end)=tmp(1,2:end,k:end);
    WF5(2,2:end,k,k:end)=tmp(2,2:end,k:end);
    tmp=WF5(:,:,k,:);
end

%%% 3 Photon WF or equivalently g3
EEEmeas=squeeze(WF5(1,end,:,:));
```

Bibliography

A. Abragam and M. Goldman. *Rep. Prog. Phys.*, 41:395, 1978.

K. A. Al-Hassanieh, V. V. Dobrovitski, E. Dagotto, and B. N. Harmon. *Phys. Rev. Lett.*, 97:037204, 2006.

M. Bajcsy, S. Hofferberth, V. Balic, T. Peyronel, M. Hafezi, A. S. Zibrov, V. Vuletic, and M. D. Lukin. *Phys. Rev. Lett.*, 102:203902, 2009.

W. L. Barnes, A. Dereux, and T. W. Ebbesen. *Nature*, 424:824, 2008.

C. Barthel, J. Medford, H. Bluhm, A. Yacoby, C. M. Marcus, M. P. Hanson, and A. C. Gossard. *Phys. Rev. B*, 85:035306, 2012.

D. Basko, I. Aleiner, and B. Altshuler. *Ann. Phys. N.Y.*, 321:1126, 2006.

D. Belitz and T. R. Kirkpatrick. *Rev. Mod. Phys.*, 66:261, 1994.

Y. Ben-Aryeh. *J. Opt. B: Quant. and Semiclass. Opt.*, 1:234, 1999.

K. M. Birnbaum, A. Boca, R. Miller, A. D. Boozer, T. E. Northup, and H. J. Kimble. *Nature*, 436:87, 2005.

I. Bloch, J. Dalibard, and S. Nascimbene. *Nat. Phys.*, 8:267, 2012.

H. Bluhm, S. Foletti, D. Mahalu, V. Umansky, and A. Yacoby. *Phys. Rev. Lett.*, 105: 216803, 2010.

H. Bluhm, S. Foletti, I. Neder, M. Rudner, D. Mahalu, V. Umansky, and A. Yacoby. *Nat. Phys.*, page 109, 2011.

C. F. Bohren and D. R. Huffman. *Absorption and Scattering of Light by Small Particles.* John Wiley & Sons, New York, NY, 1983.

E. L. Bolda, E. Tiesinga, and P. S. Julienne. *Phys. Rev. A*, 66:013403, 2002.

R. Bose, D. Sridharan, H. Kim, G. S. Solomon, and E. Waks. *Phys. Rev. Lett.*, 108: 227402, 2012.

R. W. Boyd. *Nonlinear optics.* Academic Press, San Diego, 2003.

A. S. Bracker, E. A. Stinaff, D. Gammon, M. E. Ware, J. G. Tischler, A. Shabaev, Al. L. Efros, D. Park, D. Gershoni, V. L. Korenev, and I. A. Merkulov. *Phys. Rev. Lett.*, 94:047402, 2005.

A. Brataas and E. I. Rashba. *Phys. Rev. B*, 84:045301, 2011.

A. Brataas and E. I. Rashba. *Phys. Rev. Lett.*, 109:236803, 2012.

F. Brennecke, T. Donner, S. Ritter, T. Bourdel, M. Khl, and T. Esslinger. *Nature*, 450:268, 2007.

D. Brooks, T. Botter, S. Schreppler, T. Purdy, N. Brahms, and D. Stamper-Kurn. *Nature*, 488:476, 2012.

I. Buluta and F. Nori. *Science*, 326:108, 2009.

T. Busch, B.G. Englert, K. Rzazewski, and M. Wilkens. *Foundations of Physics*, 28: 549, 1998.

K. Byczuk, W. Hofstetter, and D. Vollhardt. *Phys. Rev. Lett.*, 94:056404, 2005.

H. J. Carmichael, R. J. Brecha, , and P. R. Rice. *Optics Comm.*, 82:73, 1991.

I. Carusotto and C. Ciuti. *Rev. Mod. Phys.*, 85:299, 2013.

A. H. Castro Neto, F. Guinea, N. M. R. Peres, K. S. Novoselov, and A. K. Geim. *Rev. Mod. Phys.*, 81:109, 2009.

R. R. Chance, A. Prock, and R. Silbey. *Phys. Rev. A*, 12:1448, 1975.

D. E. Chang, A. S. Sørensen, E. A. Demler, and M. D. Lukin. *Nat. Phys.*, 3:807, 2007.

D. E. Chang, J. D. Thompson, H. Park, V. Vuletić, A. S. Zibrov, P. Zoller, and M. D. Lukin. *Phys. Rev. Lett.*, 103:123004, 2009.

G. Chen, D. L. Bergman, and L. Balents. *Phys. Rev. B*, 76:045312, 2007.

J. Chen, M. Badioli, P. Alonso-Gonzalez, S. Thongrattanasiri, F. Huth, J. Osmond, M. Spasenovi, A. Centeno, A. Pesquera, P. Godignon, A. Z. Elorza, N. Camara, F. J. Garca de Abajo, R. Hillenbrand, and F. H. L. Koppens. *Nature*, 487:77, 2012.

L. Childress, M. V. Gurudev Dutt, J. M. Taylor, A. S. Zibrov, F. Jelezko, J. Wrachtrup, P. R. Hemmer, and M. D. Lukin. *Science*, 314:281–285, 2006.

H. Christ, J. I. Cirac, and G. Giedke. *Phys. Rev. B*, 75:155324, 2007.

J. I. Cirac, P. Zoller, H. J. Kimble, and H. Mabuchi. *Phys. Rev. Lett.*, 78:3221, 1997.

W. A. Coish and D. Loss. *Phys. Rev. B*, 70:195340, 2004.

Y. Colombe, T. Steinmetz, G. Dubois, F. Linke, D. Hunger, and J. Reichel. *Nature*, 450:272, 2007.

B. Dayan, A. S. Parkins, T. Aok, E.P. Ostby, K.J. Vahala, and H.J. Kimble. *Science*, 319:1062–1065, 2008.

N. P. de Leon, M. D. Lukin, and H. Park. *IEEE J. Sel. Topics Quantum Electronics*, 18:1781, 2012.

P. de Vries, D. V. van Coevorden, and A. Lagendijk. *Rev. Mod. Phys.*, 70:447, 1998.

B. Denardo and S. Putterman. *Phys. Rev. B*, 37:3720, 1988.

D. C. Dixon, K. R. Wald, P. L. McEuen, and M. R. Melloch. *Phys. Rev. B*, 56:4743, 1997.

L.-M. Duan and C. Monroe. *Adv. in Atom., Mol., and Opt. Phys.*, 55:419, 2008.

Y. O. Dudin and A. Kuzmich. *Science*, 336(6083):887, 2012.

L. A. Falkovsky. *J. Phys.: Conf. Ser.*, 129:012004, 2008.

L. Fallani, J. E. Lye, V. Guarrera, C. Fort, and M. Inguscio. *Phys. Rev. Lett.*, 98: 130404, 2007.

J. A. Fan, C. Wu, K. Bao, J. Bao, R. Bardhan, N. J. Halas, V N. Manoharan, P. Nordlander, G. Shvets, and F. Capasso. *Science*, 328:1135, 2010.

Z. Fei, A. S. Rodin, G. O. andreev, W. Bao, A. S. McLeod, M. Wagner, L. M. Zhang, Z. Zhao, M. Thiemens, G. Dominguez, M. M. Fogler, A. H. Castro Neto, C. N. Lau, F. Keilmann, and D. N. Basov. *Nature*, 487:82, 2012.

S. Ferretti and D. Gerace. *Phys. Rev. B*, 85:033303, 2012.

A. L. Fetter. *Ann. Phys. N.Y.*, 81:367, 1973.

M. Fleischhauer, A. Imamoglu, and J.P. Marangos. *Rev. Mod. Phys.*, 77:633, 2005.

S. Foletti, J. Martin, M. Dolev, D. Mahalu, V. Umansky, and A. Yacoby. *arXiv*, 0801.3613, (2008).

S. Foletti, H. Bluhm, D. Mahalu, V. Umansky, and A. Yacoby. *Nat. Phys.*, 5:903, 2009.

S. M. Frolov, J. Danon, S. Nadj-Perge, K. Zuo, J.W. W. van Tilburg, V. S. Pribiag, J. W. G. van den Berg, E. P. A. M. Bakkers, and L. P. Kouwenhoven. *arXiv*, 1209.1510, 2012.

I. Fushman, D. Englund, A. Faraon, N. Stoltz, P. Petroff, and J. Vuckovic. *Science*, 320:769, 2008.

J. S. Gardner, M. J. P. Gingras, and J. E. Greedan. *Rev. Mod. Phys.*, 82:53, 2010.

A. K. Geim and K. S. Novoselov. *Nat. Mater.*, 6:183, 2007.

D. A. Genov, R. F. Oulton, G. Bartal, and X. Zhang. *Phys. Rev. B*, 83:245312, 2011.

J. Gervasoni and N. Arista. *Phys. Rev. B*, 68:235302, 2003.

S. Gopalakrishnan, B. L. Lev, and P. M. Goldbart. *Nat. Phys.*, 5:845, 2009.

A. V. Gorshkov, J. Otterbach, M. Fleischhauer, T. Pohl, and Mikhail D. Lukin. *Phys. Rev. Lett.*, 107:133602, 2011.

P. Grangier, D. F. Walls, and K. M. Gheri. *Phys. Rev. Lett.*, 81:2833, 1998.

R. Grimm, M. Weidemller, and Y. B. Ovchinnikov. *Adv. Atom., Mol. and Opt. Phys.*, 42:95, 2000.

M. Gross and S. Haroche. *Phys. Rep.*, 93:301, 1982.

M. Grzelczak, J. Vermant, E. M. Furst, and L. M. Liz-Marzan. *ACS Nano*, 4:3591, 2010.

M. Gullans, J. J. Krich, J. M. Taylor, H. Bluhm, B. I. Halperin, C. M. Marcus, M. Stopa, A. Yacoby, and M. D. Lukin. *Phys. Rev. Lett.*, 104:226807, 2010.

R. Hanson, L. P. Kouwenhoven, J. R. Petta, S. Tarucha, and L. M. K. Vandersypen. *Rev. Mod. Phys.*, 79:1217, 2007.

S. Haroche. *Rev. Mod. Phys.*, 85:1083, 2013.

S. E. Harris and Y. Yamamoto. *Phys. Rev. Lett.*, 81:3611, 1998.

G. V. Hartland. *Chem. Rev.*, 111:3858, 2011.

E. Hecht. *Optics.* Addison-Wesley, 3rd edition, 1998.

C. Henkel, S. Potting, and M. Wilkens. *Appl. Phys. B*, 69:379, 1999.

K. Hennessy, A. Badolato, M. Winger, D. Gerace, M. Atatüre, S. Gulde, S. Fält, E. L. Hu, and A. Imamoğlu. *Nature*, 445:896, 2007.

A. Högele, M. Kroner, C. Latta, M. Claassen, I. Carusotto, C. Bulutay, and A. Imamoglu. *Phys. Rev. Lett.*, 108:197403, 2012.

B. Huang, M. Bates, and X. Zhuang. *Annual Rev. of Biochem.*, 78:993, 2009.

J. Hwang, M. Pototschnig, R. Lettow, G. Zumofen, A. Renn, S. Gotzinger, and V. Sandoghdar. *Nature*, 460:76, 2009.

A. Imamoglu, H. Schmidt, G. Woods, and M. Deutsch. *Phys. Rev. Lett.*, 79:1467, 1997.

M. Jablan, H. Buljan, and M. Soljacic. *Phys. Rev. B*, 80:245435, 2009.

J. D. Jackson. *Classical Electrodynamics.* John Wiley & Sons, New York, NY, 3rd edition, 1999.

D. Jaksch, C. Bruder, J. I. Cirac, C. W. Gardiner, and P. Zoller. *Phys. Rev. Lett.*, 81:3108, 1998.

F. Jelezko and J. Wrachtrup. *Phys. Stat. Sol. a*, 203(13):3207, 2006.

J. D. Joannopoulos, S. G. Johnson, J. N. Winn, and R. D. Meade. *Photonic Crystals: Molding the Flow of Light.* Princeton Univ. Press, 2nd edition, 2008.

P. B. Johnson and R. W. Christy. *Phys. Rev. B*, 6:4370, 1972.

M. J. Kastoryano, F. Reiter, and A. S. Sørensen. *Phys. Rev. Lett.*, 106:090502, 2011.

H. J. Kimble. *Nature*, 453:1023, 2008.

D. Klauser, W. A. Coish, and Daniel Loss. *Phys. Rev. B*, 78:205301, 2008.

F. H. L. Koppens, K. C. Nowack, and L. M. K. Vandersypen. *Phys. Rev. Lett.*, 100: 236802, 2008.

F. H. L. Koppens, D. E. Chang, and F. J. Garcia de Abajo. *Nano Lett.*, 11:3370, 2011.

J. R. Krenn, A. Dereux, J. C. Weeber, E. Bourillot, Y. Lacroute, J. P. Goudonnet, G. Schider, W. Gotschy, A. Leitner, F. R. Aussenegg, and C. Girard. *Phys. Rev. Lett.*, 82:2590, 1999.

R. Kress. *Numerical Analysis.* Springer-Verlag, 1998.

A. Kubanek, A. Ourjoumtsev, I. Schuster, M. Koch, P. W. H. Pinkse, K. Murr, and G. Rempe. *Phys. Rev. Lett.*, 101:203602, 2008.

A. Lagendijk, B. A. Van Tiggelen, and D. Wiersma. *Phys. Today*, 62:24, 2009.

C. W. Lai, P. Maletinsky, A. Badolato, and A. Imamoglu. *Phys. Rev. Lett.*, 96:167403, 2006.

V. Y. F. Leung, A. Tauschinsky, N. J. van Druten, and R. J. C. Spreeuw. *arXiv*, 1104.3067, 2012.

M. Lewenstein, A. Sanpera, and V. Ahufinger. *Ultracold Atoms in Optical Lattices: Simulating Quantum Many- Body Systems.* Oxford University Press, 2012.

J. Q. Liao and C. K. Law. *Phys. Rev. A*, 82:053836, 2010.

N. C. Lindquist, P. Nagpal, K. M. McPeak, D. J. Norris, and S.-H. Oh. *Rep. Prog. Phys.*, 75:036501, 2012.

H.-Y. Lo, Y.-C. Chen, P.-C. Su, H.-C. Chen, J.-X. Chen, Y.-C. Chen, I. A. Yu, and Y.-F. Chen. *Phys. Rev. A*, 83:041804, 2011.

M. D. Lukin, M. Fleischhauer, R. Coté, L. M. Duan, D. Jaksch, J. I. Cirac, and P. Zoller. *Phys. Rev. Lett.*, 87:037901, 2001.

H. Mabuchi. *arXiv:1110.5583*, 2011.

S. A. Maier. *Plasmonics: Fundamentals and Applications.* Springer, New York, 2007.

F. Marquardt and S. Girvin. *Physics*, 2:40, 2009.

N. Matsuda, R. Shimizu, Y. Mitsumori, H. Kosaka, and K. Edamatsu. *Nature Photonics*, 3:95, 2009.

B. M. Maune, M. G. Borselli, B. Huang, T. D. Ladd, P. W. Deelman, K. S. Holabird, A. A. Kiselev, I. Alvarado-Rodriguez, R. S. Ross, A. E. Schmitz, M. Sokolich, C. A. Watson, M. F. Gyure, and A. T. Hunter. *Nature*, 481:344, 2012.

P. Michler, A. Kiraz, C. Becher, W. V. Schoenfeld, P. M. Petroff, Lidong Zhang, E. Hu, and A. Imamoglu. *Science*, 290:2282, 2000.

S. A. Mikhailov. *Phys. Rev. B*, 84:045432, 2011.

S. A. Mikhailov and K. Ziegler. *J. Phys.: Condens. Matter*, 20:384204, 2008.

S. A. Mikhailov and K. Ziegler. *Phys. Rev. Lett.*, 99:016803, 2007.

B. Murphy and L. V. Hau. *Phys. Rev. Lett.*, 102:033003, 2009.

P. Nagpal, N. C. Lindquist, S.-H. Oh, and D. J. Norris. *Science*, 325:594, 2009.

R. R. Nair, P. Blake, A. N. Grigorenko, K. S. Novoselov, T. J. Booth, T. Stauber, N. M. R. Peres, and A. K. Geim. *Science*, 320:1308, 2008.

J. L. O'Brien, A. Furusawa, and J. Vuckovic. *Nature Photonics*, 3:687, 2009.

K. Ono and S. Tarucha. *Phys. Rev. Lett.*, 92:256803, 2004.

S. Y. Park and D. Stroud. *Phys. Rev. B*, 69:125418, 2004.

J. R. Petta, A. C. Johnson, J. M. Taylor, E. A. Laird, A. Yacoby, M. D. Lukin, C. M. Marcus, M. P. Hanson, and A. C. Gossard. *Science*, 309:2180, 2005.

J. R. Petta, J. M. Taylor, A. C. Johnson, A. Yacoby, M. D. Lukin, C. M. Marcus, M. P. Hanson, and A. C. Gossard. *Phys. Rev. Lett.*, 100:067601, 2008.

T. Peyronel, O. Firstenberg, Q. Y. Liang, S. Hofferberth, A. V. Gorshkov, T. Pohl, M. D Lukin, and V. Vuletić. *Nature*, 488:57, 2012.

T. Peyronel, O. Firstenberg, Q. Y. Liang, A. V. Gorshkov, , M. D Lukin, and V. Vuletić. *Nature, in press*, 2013.

H. Pichler, J. Schachenmayer, J. Simon, P. Zoller, and A. J. Daley. *arXiv*, 1205.6189, 2012.

D. Press, S. Götzinger, S. Reitzenstein, C. Hofmann, A. Löffler, M. Kamp, A. Forchel, and Y. Yamamoto. *Phys. Rev. Lett.*, 98:117402, 2007.

A. Principi, G/ Vignale, M. Carrega, and M. Polini. *arXiv*, 1305.4666, 2013.

J. D. Pritchard, D. Maxwell, A. Gauguet, K. J. Weatherill, M. P. A. Jones, and C. S. Adams. *Phys. Rev. Lett.*, 105:193603, 2010.

M. Quinten, A. Leitner, J.R. Krenn, and F.R. Ausenegg. *Opt. Lett.*, 23:1331, 1998.

G. Ramon and Xuedong Hu. *Phys. Rev. B*, 75:161301(R), 2007.

M. T. H. Reid, A. W. Rodriguez, J. White, and S. G. Johnson. *Phys. Rev. Lett.*, 103: 040401, 2009.

D. J. Reilly, J. M. Taylor, E. A. Laird, J. R. Petta, C. M. Marcus, M. P. Hanson, and A. C. Gossard. *Phys. Rev. Lett.*, 101:236803, 2008a.

D. J. Reilly, J. M. Taylor, J. R. Petta, C. M. Marcus, M. P. Hanson, and A. C. Gossard. *Science*, 321:817, 2008b.

H. Ribeiro and G. Burkard. *Phys. Rev. Lett.*, 102:216802, 2009.

M. S. Rudner and L. S. Levitov. *Phys. Rev. B*, 82:155418, 2010.

M. S. Rudner and L. S. Levitov. *arXiv*, 1209.2997, 2012.

M. Rycenga, C. M. Cobley, J. Zeng, W. Li, C. H. Moran, Q. Zhang, D. Qin, and Y. Xia. *Chem. Rev.*, 111:3669, 2011.

G. Salis, D. T. Fuchs, J. M. Kikkawa, D. D. Awschalom, Y. Ohno, and H. Ohno. *Phys. Rev. Lett.*, 86:2677, Mar 2001.

H. Schmidt and A. Imamoğlu. *Opt. Lett.*, 21:1936, 1996.

V. M. Shalaev. *Nature Photonics*, 1:41, 2007.

M. D. Shulman, O. E. Dial, S. P. Harvey, H. Bluhm, V. Umansky, and A. Yacoby. *Science*, 336(6078):202–205, 2012.

J. Simon, W. S. Bakr, R. Ma, M. E. Tai, P. M. Preiss, and M. Greiner. *Nature*, 472 (7343):307, 2011.

A. W. Snyder and J. Love. *Optical Waveguide Theory.* Springer, 1st edition, 1983.

C. Stehle, H. Bender, C. Zimmermann, D. Kern, M. Fleischer, and S. Slama. *Nat. Phot.*, 5:494, 2011.

D. Stepanenko, M. Rudner, B. I. Halperin, and D. Loss. *Phys. Rev. B*, 85:075416, 2012.

M. Stopa, J. J. Krich, and A. Yacoby. *Phys. Rev. B*, 81:041304(R), 2010.

P. Strack and S. Sachdev. *Phys. Rev. Lett.*, 107:277202, 2011.

B. Sun, C. M. E. Chow, D. G. Steel, A. S. Bracker, D. Gammon, and L. J. Sham. *Phys. Rev. Lett.*, 108:187401, 2012.

R. Takahashi, K. Kono, S. Tarucha, and K. Ono. *Phys. Rev. Lett.*, 107:026602, 2011.

H. Tanji-Suzuki, W. Chen, R. Landig, J. Simon, and V. Vuletić. *Science*, 333:1266, 2011.

J. M. Taylor, J. R. Petta, A. C. Johnson, A. Yacoby, C. M. Marcus, and M. D. Lukin. *Phys. Rev. B*, 76:035315, 2007.

R. J. Thompson, G. Rempe, and H. J. Kimble. *Phys. Rev. Lett.*, 68:1132, 1992.

O. Tsyplyatyev and D. Loss. *Phys. Rev. Lett.*, 106:106803, 2011.

Q. A. Turchette, C. J. Hood, W. Lange, H. Mabuchi, and H. J. Kimble. *Phys. Rev. Lett.*, 75:4710, 1995.

B. Urbaszek, X. Marie, T. Amand, O. Krebs, P. Voisin, P. Maletinsky, A. Högele, and A. Imamoglu. *Rev. Mod. Phys.*, 85:79, 2013.

E. G. M. van Kempen, S. J. J. M. F. Kokkelmans, D. J. Heinzen, and B. J. Verhaar. *Phys. Rev. Lett.*, 88:093201, 2002.

B. J. Verhaar, E. G. M. van Kempen, and S. J. J. M. F. Kokkelmans. *Phys. Rev. A*, 79:032711, 2009.

F. Verstraete, M. M. Wolf, and J. I. Cirac. *Nat. Phys.*, 5:633, 2009.

N. V. Vitanov and B. M. Garraway. *Phys. Rev. A*, 53:4288, Jun 1996.

T. Volz, A. Reinhard, M. Winger, A. Badolato, K. J. Hennessy, E. L. Hu, and A. Imamoğlu. *Nat. Photon.*, 6:605, 2012.

Y. Wang, R.-B. Liu, and L. J. Sham. *Phys. Rev. B*, 74:195301, 2006.

W. M. Witzel and S. Das Sarma. *Phys. Rev. B*, 77:165319, 2008.

Q. Wu, G. D. Feke, R. D. Grober, and L. P. Ghislain. *Appl. Phys. Lett.*, 75:4064, 1999.

B. Wunsch, T. Stauber, F. Sols, and F. Guinea. *New J. Phys.*, 8:318, 2006.

J. M. Wylie and J. E. Sipe. *Phys. Rev. A*, 30:1185, 1984.

H. Yan, T. Low, W. Zhu, Y. Wu, M. Freitag, X. Li, F. Guinea, P. Avouris, and F. Xia. *Nat. Phot.*, 7:394, 2013.

W. Yao and Y. Luo. *Europhys. Lett.*, 92:17008, 2010.

W. Yi, A. J. Daley, G. Pupillo, and P. Zoller. *New Journal of Physics*, 10:073015, 2008.

G. Yusa, K. Muraki, K. Takashina, K. Hashimoto, and Y. Hirayama. *Nature*, 434: 1001, 2005.

F. A. Zwanenburg, A. S. Dzurak, A. Morello, M. Y. Simmons, Lloyd C. L. Hollenberg, G. Klimeck, S. Rogge, S. N. Coppersmith, and M. A. Eriksson. *Rev. Mod. Phys.*, 85:961, 2013.